Imperial College London
Department of Materials

Controlling Dopant Distributions and Structures in Advanced Semiconductors

Hassan A. Tahini

Jan 2014

Submitted in part fulfilment of the requirements for the degree of
Doctor of Philosophy in Materials of Imperial College London
and the Diploma of Imperial College London

Declaration

I herewith certify that all material in this dissertation which is not my own work has been properly acknowledged.

Hassan A. Tahini

Abstract

The suitability of silicon for micro and sub-micro electronic devices is being challenged by the aggressive and continuous downscaling of device feature size. New materials with superior qualities are continually sought-after. In this thesis, defects are examined in two sets of silicon alternate materials; germanium (Ge) and III-V semiconductors. Point defects are of crucial importance in understanding and controlling the properties of these electronic materials. Point defects usually introduce energy levels into the band gap, which influence the electronic performance of the material. They are also key in assisting mass transport.

Here, atomistic scale computational methods are employed to investigate the formation and migration of defects in Ge and III-V semiconductors. The behaviour of n-type dopants coupled to a vacancy in Ge (known as E-centres) is reported from thermodynamic and kinetic points of view, revealing that these species are highly mobile, consequently, a strategy is proposed to retard one of the n-dopants. Further, the electronic structure of Ge is examined and the changes induced in it due to the application of different types of strain along different planes and directions. The results obtained agree with established experimental values regarding the bands transition from indirect to direct under biaxial strain. This is used to support further predictions, which indicate that a moderate strain parallel to the [111] direction can efficiently transform Ge into a direct band gap material, with a band gap energy useful for technological applications.

Vacancies and antisites in III-V semiconductors have been studied under various growth and doping conditions. Results presented in this thesis help predict and explain the stability of some defects over a range of growth conditions. This, together with knowledge of the kinetics of migration of Ga and As/Sb vacancies is used to explain the disparities in self-diffusion between GaAs and GaSb.

بِسْمِ ٱللَّهِ ٱلرَّحْمَٰنِ ٱلرَّحِيمِ
وَ قُلْ رَبِّي زِدْنِي عِلْمَا

Lord, increase my knowledge.

To the family that made me and to the family that I am to make...

$\mathscr{H}_2\mathscr{O}$

Acknowledgement

I want to start by thanking my supervisors: Prof. Grimes for his excellent supervision, Prof. Schwingenschlögl for his usual efficiency and Dr Chroneos for his unparalleled creativity... Their guidance and support throughout the stages of this research is the dream of any student.

The members of the Atomistic Simulations Group are highly thanked for their usual assistance and help, in particular Dr Rushton who is an encyclopaedia when it comes to computational materials science and programming, Dr Murphy for the daily discussions and advices and Miss Warriss who without her management skills, the office would have been in a state of high entropy.

This research would have been less entertaining without the daily chess games with Sam, Charlie and Patrick. The problem below is for you guys... White to play and mate in three!

Finally, I want to thank my parents and my wife Ola for being constantly by my side.

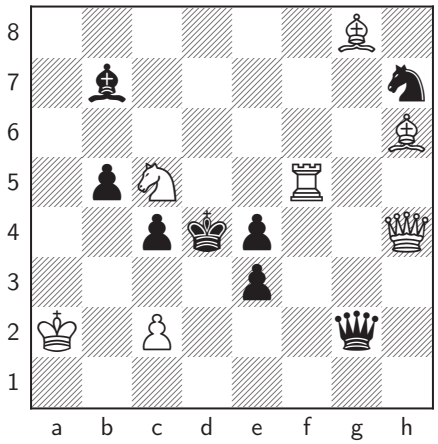

Copyright Declaration

List of Publications

1. **H. A. Tahini**, A. Chroneos, H. Bracht, S. T. Murphy, R. W. Grimes and U. Schwingenschlögl, "*Antisites and anisotropic diffusion in GaAs and GaSb*" Appl. Phys. Lett. **103**, 142107 (2013).

2. **H. A. Tahini**, A. Chroneos, S. T. Murphy, R. W. Grimes and U. Schwingenschlögl, "*Vacancies and defect levels in III-V semiconductors*" J. App. Phys. **114**, 063517 (2013).

3. **H. A. Tahini**, A. Chroneos, U. Schwingenschlögl and R. W. Grimes, "*Co-doping with antimony to control phosphorous diffusion in germanium*" J. App. Phys. **113**, 073704 (2013).

4. **H. A. Tahini**, A. Chroneos, R. W. Grimes and U. Schwingenschlögl, "*Point defect engineering strategies to retard phosphorous diffusion in germanium*", Phys. Chem. Chem. Phys. (2013).

5. **H. A. Tahini**, A. Chroneos, R. W. Grimes, U. Schwingenschlögl and A Dimoulas, "*Strain induced changes of the electronic structure of germanium*", J. Phys.: Condens. Matter **24**, 195802 (2012).

6. **H. A. Tahini**, A. Chroneos, R. W. Grimes, U. Schwingenschlögl, "*Diffusion of tin in germanium: a GGA+U approach*", Appl. Phys. Lett. **99**, 162103 (2011).

7. **H. A. Tahini**, A. Chroneos, R. W. Grimes, U. Schwingenschlögl, and H. Bracht, "*Diffusion of E-Centres in germanium predicted using the GGA+U approach*", Appl. Phys. Lett. **99**, 072112 (2011).

Contents

List of Tables

List of Figures

1. Background

> "*If all scientific knowledge were to be destroyed, and only one sentence passed on to the next generation of creatures, what statement would contain the most information in the fewest words? I believe it is the atomic hypothesis- that* ***all things are made of atoms****. In that one sentence you will see an enormous amount of information about the world, if just a little imagination and thinking are applied.*"
>
> — Richard Feynman, physicist

1.1. The Quest for High Electron Mobility Semiconductors

Electronic devices form the pillars of our modern life. The operation of these devices relies on the physical properties of semiconducting materials. Silicon dominates the world of semiconductor devices, even though, the first transistor was made out of germanium. The abundance of silicon in nature and the existence of a stable silicon oxide which acts as a dielectric, made silicon an obvious choice for electronic applications.

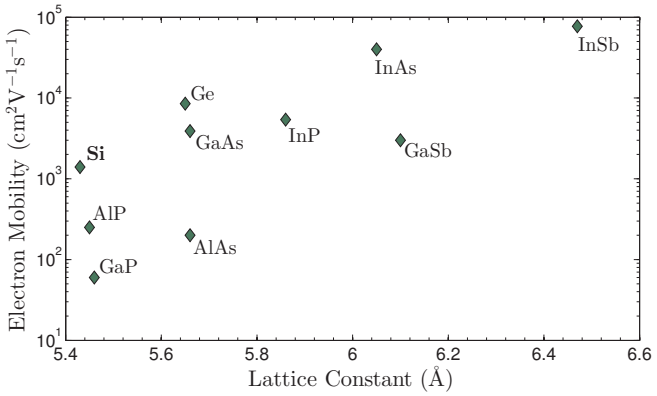

Figure 1.1.: Electron mobilities of Ge, Si and III-V semiconductors.

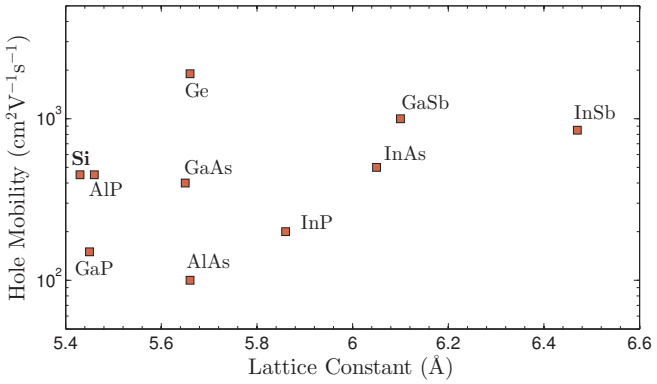

Figure 1.2.: Hole mobilities of Ge, Si and III-V semiconductors.

However, the ongoing progress in fabricating devices on smaller length scales has given rise to many challenges to the suitability of silicon as an efficient and reliable semiconductor. Quantum mechanical effects such as electron tunnelling become important and may lead to a degradation of performance [10–12]. This regenerated interest in high-κ dielectric materials, such as hafnium (IV) oxide [13]. However, using silicon with a non-native oxide leads to a decrease in channel carrier mobility [14]. Germanium on the other hand, has a higher low field mobility than silicon and the availability of compatible non-native oxides could substitute for the lack of stable germanium oxide. Another advantage for the electronics industry is that germanium is compatible with some silicon

manufacturing processes. Figs. 1.1 and 1.2 are the electron and hole mobilities of Si, Ge and III-V semiconductors. Ge and indium antimonide (InSb) possess the highest hole and electron mobilities respectively among the semiconductors considered here, making them desirable options for many applications.

The physical properties of germanium as well as III-V semiconductors are less well understood than silicon, as much of the early work concentrated on silicon due to its dominance of the electronics technology. Theoretical modelling also encountered several problems. The underestimation of the band gap in density functional theory studies posed a serious problem in studying the properties of electronically active impurities in germanium and other semiconductors.

1.2. Defects in Solids

Any deviation from an ideal crystal structure is considered a defect [15]. Several types can occur in a crystal (See Fig. 1.3). A missing atom from a normally occupied position leaves behind a vacancy. A foreign atom introduced (intentionally as dopant or unintentionally as impurities) into the crystal lattice will also be accommodated as a defect. If the additional atom sits on an unoccupied interstice, then it is also known as an interstitial. Interstitial atoms of the same nature as the elements making up the crystal are referred to as self-interstitials. If the foreign atom occupies the site of a host crystal atom then it forms a substitutional defect. These defects are referred to collectively as point defects. Formation of point defects is enhanced during crystal growth when subjected to elevated temperatures, or if the crystal is exposed to radiation or treated with high energy particles. A process known as annealing, which involves heating the crystal at moderate temperatures for extended periods of time is used to change the composition of some of the point defects in the crystal. However, any form of treatment will not completely eliminate the defects present, and a population of

point defects will always remain.

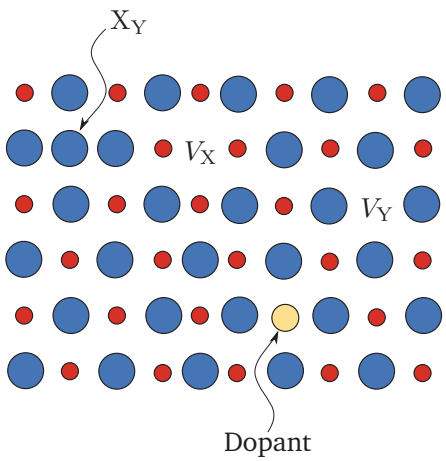

Figure 1.3.: Simple point defects in a crystal structure comprised of X (larger blue circles) and Y (smaller red circles) atoms. Here, a missing X atom V_X, a missing Y atom V_Y, X atom on a Y atom site X_Y (known as an antisite defect) and a substitutional dopant atom are shown.

Impurities will break the order in which the atoms and electrons are shared in the intrinsic semiconductor. Elements from group Ⅴ have one extra electron in their outer shell and are among those used to dope Si or Ge. Phosphorous (P), Arsenic (As) and Antimony (Sb) can form substitutional defects by occupying the sites of a Si or Ge atoms. Theses substitutional atoms use four of their electrons to form the normal sp^3 bonds. Depending on the binding energy, the fifth electron can be liberated from the atom and be made accessible to assist in conduction by *roaming* through the crystal under the influence of an external electric fields. Such atoms are called donors since they donate an extra electron to the conduction band of the crystal. For instance P, As and Sb donor levels in Ge are 12 meV, 13 meV and 10 meV below the conduction band [1]. This is comparable to the thermal energy of ∼25 meV at room temperature. Similarly, it is possible to use elements with fewer electrons in their outer shell relative to silicon or germanium, for example the group Ⅲ elements boron (B), aluminium (Al) and gallium (Ga) which only have 3 electrons to share with the four neighbouring crystal atoms. This deficiency of electrons can be interpreted as a hole

which possesses a positive charge relative to its surrounding. These holes introduced by the impurity atoms could be thermally activated and allowed to move freely through the crystal. The doped crystal then conducts using these positive holes and is called a p-type semiconductor [16].

At equilibrium, a very good approximation is that the law of electroneutrality must be fulfilled:

$$[D^{\bullet}] + [h^{\bullet}] = [A'] + [e'] \tag{1.1}$$

where $[D^{\bullet}]$, $[A']$, $[h^{\bullet}]$ and $[e']$ are the concentration of donors, acceptors, holes and electrons respectively (the Kröger-Vink notation [17] is used here, in which a "$\bullet$" or a "$'$" denotes a positive or a negative effective charge respectively).

In a crystalline ionic compound, a vacancy defect of one type breaks the charge neutrality of the crystal. The balance is restored by forming subsequent vacancies of the other types of the constituent atoms or other defects in order to maintain charge neutrality. This equal number of defects guarantees an overall charge neutrality of the crystal [18, 19]. There are two major types of defects involving vacancies: Frenkel or Schottky disorder. In a Frenkel disorder [20], an atom is dislodged from its normal lattice site creating a self-interstitial and leaving behind a vacancy. Thus, for an anion Frenkel defect we can generally write:

$$X_X^{\times} \rightarrow X'_{\mathrm{int}} + V_X^{\bullet} \tag{1.2}$$

Although in some ionic oxides, it is not necessarily the case that the oxygen interstitial and vacancy have opposite charges — although the oxygen vacancy is typically a double donor, the oxygen interstitial is also potentially a donor [21].

The formation enthalpy H_{FP} for a Frenkel pair can be written as the sum of the

interstitial and the vacancy formed:

$$H_{\mathrm{FP}} = H_{X'_{\mathrm{int}}} + H_{V_X^{\bullet}} \tag{1.3}$$

In a Schottky disorder equal amounts of vacancies of the various components found in a crystal exist simultaneously at equilibrium:

$$M_M^{\times} + X_X^{\times} \rightarrow V'_M + V_X^{\bullet} + \mathrm{MX} \tag{1.4}$$

Assuming that these vacancies forming the Schottky pair are non-interacting we can write the enthalpy of formation as:

$$H_{\mathrm{SP}} = H_{V'_M} + H_{V_X^{\bullet}} \tag{1.5}$$

The stoichiometry of a crystal is maintained when Frenkel or Schottky disorders are created. Highly ionic systems favour Frenkel or Schottky disorder which is a result of the favourable electrostatic interactions between these fully charged defects [15, 19].

1.3. The Role of Defects

The quality of semiconducting materials in a device such as a transistor or a photovoltaic device is governed by three parameters [22]. First, the doping level of the base material should be low which demands high purity. Second, carriers should possess high mobilities which requires perfect single crystals to reduce scattering effects [23, 24], and finally these carriers must have long lifetimes which is achieved by the two previous conditions.

Defects in a material determine many of its properties such as colour (due

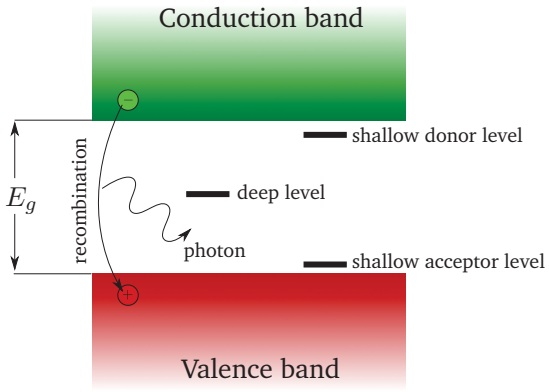

Figure 1.4.: Possible transition levels within the band gap. An excited electron in the conduction band drops to the valence band by releasing a photon with an energy equal to the band gap of the material in direct band gap materials (as shown here) or by releasing phonons in the form of heat in indirect band gap materials.

to optical transitions), conductivity (doping or scattering centres), mechanical strength (dislocations), etc.

In general, a system seeks to attain a minimum of free energy system given as the Gibbs free energy G as:

$$G = H - TS \tag{1.6}$$

where H is the enthalpy comprising the internal energy U and a pressure-volume term (PV). T is the temperature of the system. S is the entropy and is due to two contributions, vibrational S_v and configurational S_c entropy. The change in the Gibbs free energy associated with the formation of a defect can be written as [25]:

$$G^f_{D,q} = \Delta E + F^{\text{vib}} + P\Delta V \pm \mu_D \tag{1.7}$$

where ΔE, F^{vib} and ΔV are changes in the total energy, vibrational free energy and volume between the defected and perfect crystals and μ_D is the defect chemical potential (see Sec. 5.2). For solids $P\Delta V$ is negligibly small and is estimated to be $\sim 1 \times 10^{-5}$ eV [26] which is much smaller than ΔE and therefore it

is reasonable to ignore. In the work presented here, the vibrational free energy (which also includes the zero point energy) is also neglected. It is noted however, that this term is significantly enhanced by temperature and is nonnegligible at elevated temperatures [25, 27]. The remaining terms, ΔE and μ_D, are obtained from total energy calculations employing density functional calculations at 0 K.

In semiconductors, defects can exist as neutral or electrically charged species depending on the Fermi level which in turn is dependent on the level of doping, which leads to the creation of defect levels in the band gap. This is shown schematically in Fig. 1.4. A level represents a transition from one charge state to another. Throughout the thesis, these concepts will be used to calculate the formation energies of defects as a function of the Fermi level which are then used obtain the defect transition levels from one charge to the other.

2. Methodology

"Shall I refuse my dinner because I do not fully understand the process of digestion?"

— Oliver Heaviside, physicist

2.1. The Schrödinger Equation and the Hartree-Fock Approach

The ultimate properties of an electronic system might be obtained by solving an innocuous looking equation of the form:

$$\hat{H}\Psi = E\Psi \tag{2.1}$$

where E is the energy of the system, Ψ is the wavefunction which is a complex mathematical construct dependent on position and generally dependent on

time. Finally $\hat{H}$, known as the Hamiltonian operator, which is the sum of kinetic operators $\hat{K}$ due to the *motion* of electrons and nuclei and potential energy operators $\hat{V}$ arising from contributions due to electron-electron, nuclei-nuclei and electron-nuclei interactions and is given as a sum below:

$$\begin{aligned}\hat{H} = \hat{K}_{\text{electrons}} + \hat{K}_{\text{nuclei}} + \hat{V}_{\text{electron}-\text{electron}} \\ + \hat{V}_{\text{nuclei}-\text{nuclei}} + \hat{V}_{\text{electron}-\text{nuclei}}\end{aligned} \tag{2.2}$$

In full terms, assuming the Born-Oppenheimer approximation which neglects the nuclear kinetic energy, this can be written as:

$$\begin{aligned}\hat{H} = -\frac{\hbar^2}{2m_e}\sum \nabla^2_{\mathbf{r}_i} + \frac{1}{2}\sum \frac{Z_I e^2}{|\mathbf{r}_i - \mathbf{R}_I|} + \frac{1}{2}\sum \frac{e^2}{|\mathbf{r}_i - \mathbf{r}_j|} \\ + \frac{1}{2}\sum \frac{Z_I Z_J e^2}{|\mathbf{R}_I - \mathbf{R}_J|}\end{aligned} \tag{2.3}$$

where the first term denotes the electron kinetic energy contribution, the second and third terms represent the electron-nucleus and electron-electron interactions. The problem is impossible to solve analytically for any system consisting of more than few electrons. Hence, many early attempts were made to solve the problem numerically with few assumptions to simplify the task.

The Hartree-Fock approach relies on the linear addition of atomic orbitals $\phi_\mu(r)$ to generate molecular orbitals, $\psi_i(\mathbf{r}_i)$:

$$\psi_i(\mathbf{r}_i) = \sum_\mu c_{\mu i}\phi_\mu(\mathbf{r}_i) \tag{2.4}$$

where $c_{\mu i}$ are expansion coefficients. An ansatz for the N electron wavefunction is a product of the individual molecular orbitals:

$$\Psi(\{\mathbf{r}_i\}) = \prod_i \psi_i(\mathbf{r}_i) \tag{2.5}$$

Electrons are fermions obeying the Pauli exclusion principle, their wavefunctions

must be antisymmetric upon exchange of two electrons. This is guaranteed by using a Slater determinant for N electrons system of the form [28]:

$$\Psi_{\mathrm{HF}}(\mathbf{r}_1, \mathbf{r}_2, \ldots, \mathbf{r}_N) = \frac{1}{\sqrt{N!}} \begin{vmatrix} \psi_1(\mathbf{r}_1) & \psi_2(\mathbf{r}_1) & \cdots & \psi_N(\mathbf{r}_1) \\ \psi_1(\mathbf{r}_2) & \psi_2(\mathbf{r}_2) & \cdots & \psi_N(\mathbf{r}_2) \\ \vdots & \vdots & \ddots & \vdots \\ \psi_1(\mathbf{r}_N) & \psi_2(\mathbf{r}_N) & \cdots & \psi_N(\mathbf{r}_N) \end{vmatrix} \tag{2.6}$$

The classical description of a force acting on a system, in this case a nucleus I, is expressed as:

$$F_I = -\frac{\partial E}{\partial \mathbf{R}_I} \tag{2.7}$$

The energy is obtained from the expectation value of the Hamiltonian as:

$$E = \langle \Psi | \hat{H} | \Psi \rangle \tag{2.8}$$

which can then be used to calculate the forces on a quantum mechanical system according to the Hellman-Feynmann theorem [29, 30]:

$$F_I = -\left\langle \Psi \left| \frac{\partial \hat{H}}{\partial R_I} \right| \Psi \right\rangle - \left\langle \frac{\partial \Psi}{\partial \mathbf{R}_I} \left| \hat{H} \right| \Psi \right\rangle - \left\langle \Psi \left| \hat{H} \right| \frac{\partial \Psi}{\partial \mathbf{R}_I} \right\rangle \tag{2.9}$$

where the last two terms in Eq. 2.9 disappear due to the stationarity of the total energy with respect to variations of the wavefunctions [31].

2.2. Density Functional Theory

The major problem in solving the many-electron problem lies in the description of electron-electron interactions. A practical solution to the problem is to replace this explicit term with an effective potential term, V_{eff}.

The aim of density functional theory (DFT) is to transform the problem of finding

the wavefunction of a system consisting of N interacting electrons into a problem of determining the electronic density with an appropriate one-electron potential which includes the exchange-correlation (xc) energy (while the exchange term is adequately defined in the HF approach, correlation effects are absent) as well as the electron-electron and electron-nucleus Coulomb interactions. Knowledge of this one-electron potential can allow the determination of both the energy of the system and the crystal structure which corresponds to the configuration that minimizes the energy of the system.

DFT is based on two theorems that were formulated in 1964 by Hohenberg and Kohn [32] which can be summarized as follows:

(a) There is a mapping between the external potential $V_{\text{ext}}(\mathbf{r})$ and the ground state particle density $n_0(\mathbf{r})$. This implies that the electron density, which is a function of the spatial coordinates, is sufficient to describe any physical quantity of an interacting electron gas, in particular the total energy of the system $E[n]$.

(b) There exists a density functional such that $E[n]$ reaches its minimum at the true density $n(\mathbf{r})$.

The total energy functional is expressed as [28]:

$$E_{\text{HK}}[n] = T[n] + E_{\text{int}}[n] + \int V_{\text{ext}}(\mathbf{r}) n(\mathbf{r}) \mathrm{d}^3\mathbf{r} + E_{II} \tag{2.10}$$

where $T[n]$ is the internal kinetic energy and E_{II} represents the nuclei interaction energy.

While the theorems above prove the existence of a functional sufficient to describe the ground state properties of a system, an analytical form was (and still is) unknown.

Kohn and Sham proposed replacing the original many-body problem by an auxiliary independent particle problem [33] with the assumption that the ground state density of the interacting system is the same as the non-interacting system. The assumption is guaranteed when this system of non-interacting particles experiences an effective potential V_{eff}.

2.2.1. Exchange and Correlation

The electron-electron interactions are accounted for by the exchange-correlation functional $E_{\text{xc}}[n(\mathbf{r})]$. No analytical form of this functional exists and computations rely on approximations, most commonly the local density and generalized gradient density approximations (LDA and GGA respectively).

The LDA expresses the potential at a given site of an electron as a function of the electron density at that site, and is defined as [34]:

$$E_{\text{xc}}^{\text{LDA}}[n(\mathbf{r})] = \int n(\mathbf{r})\epsilon_{\text{xc}}^{\text{LDA}}(n(\mathbf{r}))d\mathbf{r} \tag{2.11}$$

where $\epsilon_{\text{xc}}^{\text{LDA}}(n(\mathbf{r}))$ is the exchange-correlation energy per electron in a uniform electron gas of density n.

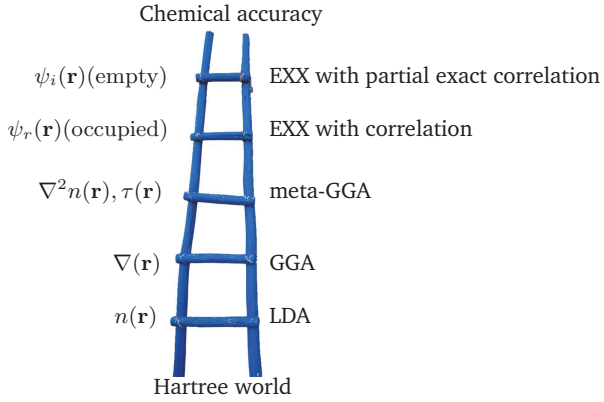

Figure 2.1.: Jacob's ladder depicting the hierarchy in xc treatment in various functionals [3].

The above simple treatment assumes that the electron density is homogeneous,

which in real materials, is not the case. An improvement would be to account for the local gradients of the electron density which is the essence of the generalized gradient approximation. Here the xc energy density is a function of the local density and its gradient:

$$E_{\mathrm{xc}}^{\mathrm{GGA}} = \int n(\mathbf{r})\epsilon_{\mathrm{xc}}^{\mathrm{GGA}}(n(\mathbf{r}), \nabla n(\mathbf{r}))d\mathbf{r} \tag{2.12}$$

GGA exists in different flavours. Each is constructed based on certain approximations that are based on both theoretical methods that consider sum rules, long-range decay, etc., and by empirical fitting of parameters in such a way to produce experimental results. Some common flavours include Perdew-Becke (PB), Perdew-Wang 1986 [35] and 1991 [36] (PW86 and PW91 respectively), Perdew-Beck-Ernzerhof (PBE) [37], etc.

It is well known that the lack of an exact exchange leads to an inaccurate description of the electronic structure of the materials under investigation. Many schemes were put forward to correct for this. These are reflected in the rungs of Fig. 2.1 known as *Jacob's ladder* [3].

2.2.2. Bloch's Theorem and the Basis Set

In order to solve the Schrödinger equations computationally it is customary to transform the equations into a linear eigenvalue problem by expanding the Kohn-Sham wavefunctions using a basis set. Due to the periodicity of the crystalline structures one can make use of the periodic boundary conditions and use plane waves as the basis set. According to Bloch's theorem, a molecular orbital with Bloch wavevector $\mathbf{k}$ in the first Brillouin zone can then be written in the form:

$$\psi_{n,\mathbf{k}}(\mathbf{r}) = \sum_{\mathbf{G}} c_{n,\mathbf{k}+\mathbf{G}} e^{i(\mathbf{k}+\mathbf{G}).\mathbf{r}} \tag{2.13}$$

where the summation is over all reciprocal lattice vectors $\mathbf{G}$. However, the above summation is truncated by choosing a cut off energy, E_{cut} and for each $\mathbf{k}$ only include lattice vectors such that $\left|\frac{(\mathbf{k}+\mathbf{G})^2}{2}\right| < E_{\text{cut}}$.

However, for rapidly varying functions, plane-wave expansions converge very slowly. This is the case close to the nucleus where the electronic wavefunctions oscillate rapidly. These electrons are not normally involved in chemical reactions, therefore the potential at the nucleus is replaced by a pseudopotential, which includes the combined potential of the nucleus and the core electrons (Sec. 2.2.4).

Integrations in the Brillouin zone are performed using the Monkhorst-Pack scheme [38] in which an $n \times n \times n$ mesh is used to sample the reciprocal unit cell. The symmetry then reduces the number of $\mathbf{k}$-points into a set of points in the irreducible wedge of the Brillouin zone. To determine a suitable cutoff energy and a Brillouin zone sampling grid, convergence tests were performed. Fig. 2.2 shows that for Ge in a 64 atom supercell a cutoff energy (which is independent of the cell size) of ~ 380 eV is sufficient to converge the total energy to within 2 meV. Similarly a $3 \times 3 \times 3$ $\mathbf{k}$-point grid was adequate to achieve the same order of convergence.

2.2.3. DFT+U and Hybrid Functionals

One major shortcoming of DFT calculations is the well known band gap problem. The calculated band gaps are much smaller than those calculated from experiments. This is due to electron self interactions and the lack of derivative of the exchange-correlation potential with respect to the occupation number. This leads to an obvious problem, which is determining the accurate defect transition levels within the band gap. Another problem might be the effect of band gap underestimation on the calculated defect formation energies. Some of these

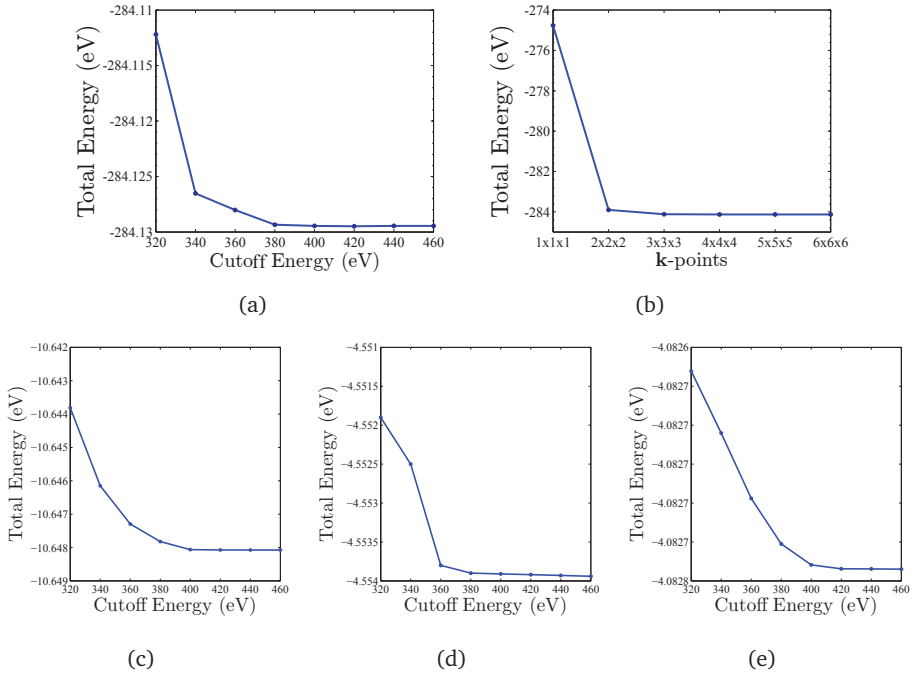

Figure 2.2.: (a) Total energy convergence with respect to cutoff energy for a supercell containing 64 Ge atoms. (b) Total energy convergence with respect to **k**-points. (c)-(e) Total energy convergence of typical Ge dopants, P, As and Sb respectively.

problems might be partially eliminated when using total energy differences to calculate the defect ionization levels, however false electronic occupations near the conduction band edge will still remain a problem. The band gap problem remains fairly insensitive to the choice of LDA or GGA functionals. For example, Ge is predicted to have no band gap, whereas the experimental band gap is 0.74 eV, similarly Si is predicted to have a gap of 0.61 eV whereas the experimental band gap is 1.16 eV [39].

The LDA/GGA+U approach was introduced to treat systems with partially occupied bands originating from localized d or f states [40]. The main step in this approach is to divide the electrons into two subsystems: localized d or f electrons with strong Coulomb interactions which are taken into account using a model Hamiltonian (through an on-site Hubbard like U) and delocalised s and

p electrons which could be described using an orbital independent one electron potential [41]. For example, zinc oxide's (ZnO) band gap could be improved by using the LDA+U approach, where the U term lowers the energy of the Zn semi-core states and reduces the repulsion with the O p states. This causes the valence band maximum (VBM) to become lower in energy. The on-site U can also shift the conduction band minimum (CBM) to higher energies. This widening of the band edges automatically leads to a larger band gap. One should be aware that this artificial method of correcting for the band gap does not provide a solution for the physical problem that lies behind the band gap underestimation i.e. the absence of the derivative discontinuity. The method could not be expected to completely adjust the band gap to fit the measured experimental values, as in many cases fitting the band gap would lead to unphysically large values of U.

The other approach introduces what is known as hybrid functionals. In these functionals, a portion of the Hartree-Fock non-local exchange E_{x} is mixed with the exchange term taken from standard PBE ($E_{\mathrm{x}}^{\mathrm{PBE}}$). This is used to generate the unscreened PBE0 functional:

$$E_{\mathrm{xc}}^{\mathrm{PBE0}} = \alpha E_{\mathrm{x}} + (1-\alpha)E_{\mathrm{x}}^{\mathrm{PBE}} + E_{\mathrm{c}}^{\mathrm{PBE}} \tag{2.14}$$

Usually, α varies between 0 and 1 but previous work by Perdew *et al.* [42] has suggested a value of $\alpha = 0.25$ as derived from perturbation theory. Due to the non-local nature of the functional above, the convergence as a function of cutoff energy can be very slow when using a plane-wave basis set. To alleviate this problem, Heyd-Scuseria-Ernzerhof [43, 44] suggested separating the exchange term into short and long range terms and truncating the slow decaying long range term leading to a screened functional:

$$E_{\mathrm{xc}}^{\mathrm{HSE06}} = \alpha E_{\mathrm{x}}^{\mathrm{sr}}(\mu) + (1-\alpha)E_{\mathrm{x}}^{\mathrm{PBE,sr}}(\mu) + E_{\mathrm{x}}^{\mathrm{PBE,lr}}(\mu) + E_{\mathrm{c}}^{\mathrm{PBE}} \tag{2.15}$$

μ is the screening parameter, it is used to partition the short and long range using complementary error and error functions (erfc and erf respectively) according to [45]:

$$\frac{1}{r} = \mathrm{sr}(r) + \mathrm{lr}(r) = \frac{\mathrm{erfc}(\mu r)}{r} + \frac{\mathrm{erf}(\mu r)}{r} \tag{2.16}$$

An optimum value for μ was found empirically to be 0.207 Å^{-1} [43, 44, 46]. Setting $\mu = 0$ restores the PBE0 functional while for $\mu \to \infty$, HSE06 is reduced to PBE.

2.2.4. Pseudopotentials

Core electrons that are tightly bound to the nucleus play a less important role in chemical reactions and bonding [47, 48]. The speed of a numerical DFT calculation is to a large extent dependent on the number of electrons in a system and scales as O(N^3). It is therefore, highly desirable to reduce the number of electrons treated explicitly.

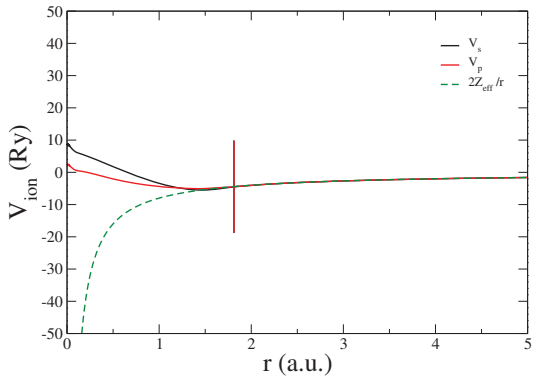

Figure 2.3.: The all electron potential and the pseudopotential.

Another complication is that due to orthogonality restrictions between the core states, the wavefunction oscillates rapidly closer to the nucleus requiring a finer numerical mesh or, in this case, a larger basis set to capture these oscillations accurately, implying more plane waves which is manifested in an increased computational cost.

This prompted the idea of using a pseuodopotential to replace the potential of these core electrons by a smooth and piecewise continuous function that extends from the nucleus up to a certain cut-off radius, beyond which the valence electrons are taken into account explicitly. Three types of pseudopotenital exist:

(a) Norm-conserving

(b) Ultrasoft

(c) Projector augmented-wave method

2.2.4.1. Norm-Conserving Pseudopotential

Norm-conserving pseudopotentials ensure that the integrals over the core region of the pseudo and all-electron charge densities are the same [49–51]. This is summarized by equation 2.17 below:

$$\int_0^{r_c} |\psi_{\mathrm{PP}}(\mathbf{r})|^2 d^3r = \int_0^{r_c} |\psi_{\mathrm{AE}}(\mathbf{r})|^2 d^3r \tag{2.17}$$

Norm-conserving pseudopotentials boosted the reliability, accuracy and transferability of pseudopotentials. The major drawback comes from the hardness of these pseudopotentials as they require a short core radius which then requires a larger number of plane waves, putting a demand on the computational efficiency.

2.2.4.2. Ultrasoft Pseudopotentials

Ultrasoft pseudopotentials relax the norm-conserving criteria hence softening the pseudopotential [52]. This soft and smooth wavefunction can be expanded using fewer plane-waves, i.e. smaller cutoff energy. One drawback is that the

construction of the pseudopotential requires many parameters and several cut-off radii and hence requires careful testing in order to guarantee transferability between systems of interest [53].

2.2.4.3. Projector Augmented-Wave Method

The projector augmented-wave (PAW) method was first proposed by Blöchl [54] and implemented by Kresse and Joubert [55]. The method relies on the transformation of all-electron wavefunctions onto auxiliary wavefunctions which are then easily expanded in terms of plane waves. Here a smooth wavefunction $\widetilde{\psi}$ is created. A transformation relation $\mathcal{T}$ relates $\widetilde{\psi}$ to ψ_{AE} via:

$$|\psi_{\mathrm{AE}}\rangle = \mathcal{T}\,|\widetilde{\psi}\rangle \tag{2.18}$$

By means of a linear transformation [54] one can express ψ_{AE} as:

$$|\psi_{\mathrm{AE}}\rangle = |\widetilde{\psi}\rangle + \sum_i (|\phi\rangle - |\widetilde{\phi}\rangle)\,\langle\widetilde{p}|\widetilde{\psi}\rangle \tag{2.19}$$

where ϕ are the AE partial waves obtained from a reference atom, $\widetilde{\psi}$ are the corresponding pseudopotential waves which are equivalent to ϕ beyond the core radius and are continuous at $r = r_c$. $\widetilde{p}$ are the projector functions and are given by:

$$\langle\widetilde{p}|\widetilde{\phi}\rangle = \delta_{ij} \tag{2.20}$$

This generally puts the PAW potential at the same level of accuracy as the AE potentials. PAW generates charge densities of valence orbitals that are not otherwise obtainable using norm-conserving or ultrasoft pseudopotentials. As such PAW have been used successfully with a usage spreading widely in the field of computational materials science.

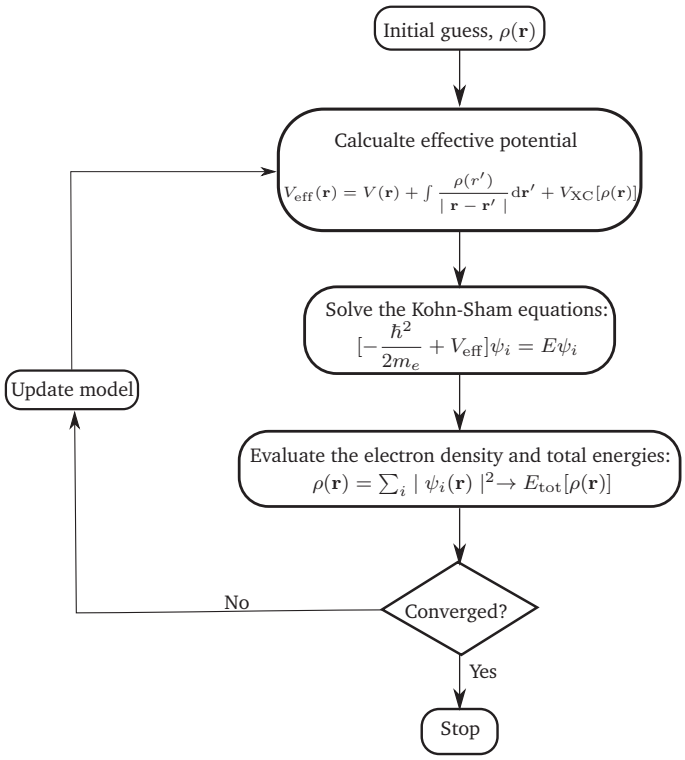

Figure 2.4.: A flow chart for a basic self-consistent iteration process.

2.2.5. Practical DFT Method

A typical DFT code will follow a simplistic path as shown in Fig. 2.4. An initial charge density is guessed based upon an initial structure that is fed into the code. That generates an effective potential which is used to solve the one particle Kohn-Sham equations whose wavefunctions are used in turn to generate a new charge density. The process is repeated iteratively until the new density gives an energy that is consistent with the old density. Once this self-consistency is achieved forces on the atoms can be calculated by invoking the the Hellman-Feynmann equations (Eq. 2.9). The geometry is optimised until these forces are minimum. In most simulations performed here (unless otherwise stated) the tolerances on the electronic self consistency iterations were set to 1×10^{-5} eV and 1×10^{-2} eV/Å or lower for forces acting on atoms.

2.3. Supercells and Boundary Conditions

The two most common approaches to study defects are the cluster approach and the supercell approach. The former attempts to model a defect surrounded by the host atoms. Convergence tests should be carried out to guarantee that the cluster's size is representative of the real physical system under investigation [56]. Once this is found it is necessary to terminate or passivate the surface of the cluster to eliminate any dangling bonds. This is usually achieved by attaching hydrogen atoms to the surface.

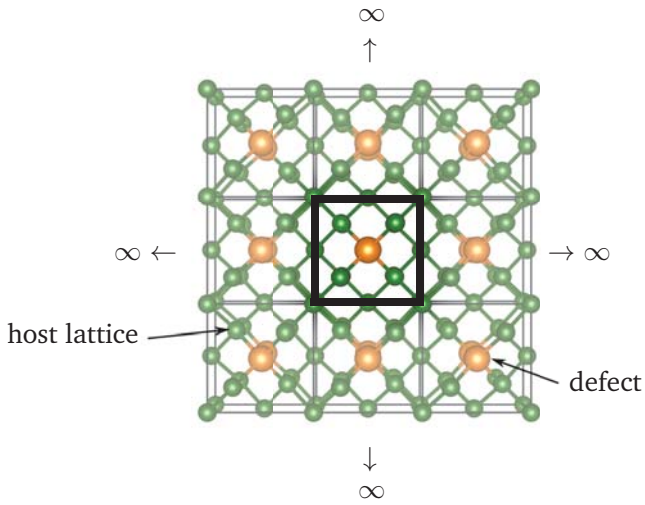

Figure 2.5.: Periodic boundary conditions, showing interactions between defects and their neighbouring images.

The supercell approach on the other hand consists of a repetition of unit cells into one larger supercell. The supercell (and the defect it might contain) is then repeated infinitely in space (see Fig. 2.5) taking full advantage of the Bloch's theorem (2.2.2). For a defective supercell, convergence tests should also be carried out to use a supercell large enough that is relatively immune to the defect-defect interactions as well as to remain computationally tractable.

In this thesis, the supercell approach is adopted as this provides a good description of the electronic structure of the host and defective systems. In addition the cluster approach suffers from considerable quantum confinement effects which are strongly dependent on the size of the cluster [57], exerting great restraints on the ability to compare directly to bulk materials.

2.4. Charged Defects Interactions

2.4.1. Finite Size Corrections

The effects of using supercells and their image repetitions in 3D are fairly well understood in terms of the consequent spurious interactions [58]. Nevertheless, the case is complicated by the introduction of charged defects since this results in both elastic and electrostatic interactions between the periodic defective cells. To account for the latter, different schemes were introduced to eliminate these unrealistic interactions as will be discussed in the following sections.

2.4.2. Compensating Background Jellium

When dealing with charged defects a compensating background (jellium) charge is assumed [59]. This due to the fact that the energy of an array of like-charge images is divergent.

2.4.3. The Makov-Payne Correction

One of the first successful attempts to effectively correct for charged defect-defect interactions was the Makov-Payne correction scheme [60] which builds on an earlier approach by Leslie and Gillian [59] which takes into account the

screening introduced by the lattice characterised by the Madelung constant (α_M) and the dielectric constant (ϵ) on a localized charge q. Makov and Payne extended this approach by including a third order term accounting for the interaction of the delocalized part of the defect-induced charge with the screened point-charge potential of the images [61] providing a more complete description given by:

$$E(L) = E(L_\infty) - \frac{\alpha_M q^2}{2\epsilon L} - \frac{2\pi q Q}{3\epsilon L^3} \tag{2.21}$$

where L is the defect-defect separation and Q is the quadrupole moment of the defect charge, $\int_V \rho_e(\mathbf{r}) r^2 \mathrm{d}^3 r$.

2.4.4. Potential Alignment

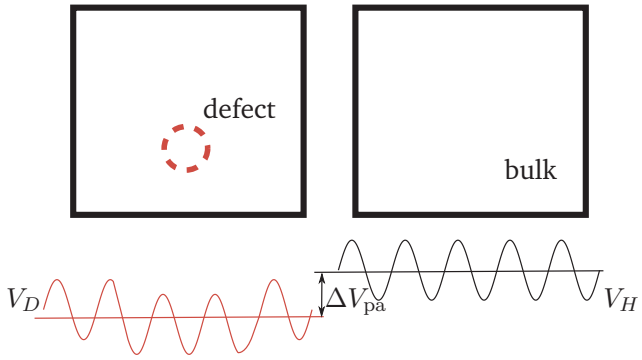

Figure 2.6.: The defect distorts the potential relative to a perfect bulk crystal. The potential alignment ΔV_{pa} restores the defective potential relative to that of a pristine crystal.

Also, the introduction of a defect distorts the electrostatic potential relative to the perfect host (Fig. 2.6) which shifts the valence band maximum which is used as a reference energy for the electron reservoir. This calls for a potential alignment, ΔV_{pa}, between the electrostatic potentials of the defective and perfect (reference) cells. The potential alignment is obtained from the average electrostatic

potentials of the host and the defective cell as [61]:

$$\Delta V = \overline{(V_D^{\alpha} - V_H^{\alpha})} \tag{2.22}$$

In which case, the average electrostatic potential at a position in the defect containing supercell far away from the defect site is chosen. This is done in order to exclude the immediate neighbours of the defect as their atomic potentials is normally affected by chemical interactions with the defect.

2.4.5. The Freysoldt *et al.* Scheme

Recently, Freysoldt *et al*. [8, 9] described a more rigorous and practical approach to this problem. It involves calculating the interaction energies between the periodic repetitions and also the interaction energy of the compensating background with the defect potential, to give a screened lattice energy, E_q^{latt}. The defect potential can be deconvoluted into a long-range and a short-range potential, for which the latter decays to zero far away from the defect (see Ref. [8]), leading to a correction term:

$$E_{\text{corr}} = E_q^{latt} - q\Delta V_{q/0} \tag{2.23}$$

where $\Delta V_{q/0}$ is the alignment term between the perfect reference cell and the defective cell. The connection between this scheme and the Makov-Payne method [60] was established by Komsa *et al* [58]. This scheme is robust and practical as it only involves knowing the electrostatic potentials for the perfect and defective cells, which are obtained in a fully *ab initio* manner without reliance on external parameters and without the need for carrying out several supercell calculations as is necessary with other methods [62].

2.5. Nudged Elastic Band

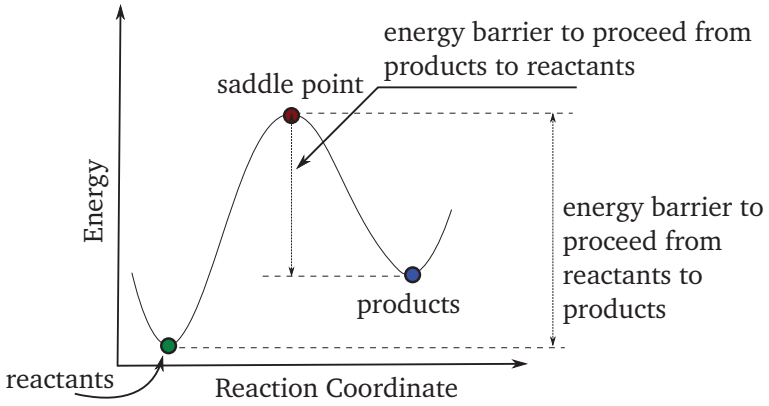

Figure 2.7.: The energy barrier to proceed from reactants to products and vice versa.

An important problem in understanding the evolution of defects in solid systems from one state or configuration to the other is the identification of minimum energy paths (MEP) on the potential energy surface (PES). The rate of chemical reactions and diffusion events are all, in part, determined by the energy barrier between the reactants and the products.

The maximum along the MEP corresponds to a saddle point which reflects the migration energy of the process under investigation. Locating saddle points can be complicated due to the complexity of PES.

Several methods have been proposed and implemented to calculate the MEP such as the drag method [63], the dimer method [63] or the chain-of-states method [64]. The most successful of these approaches is the Nudged Elastic Band (NEB) method.

In a NEB calculation, one starts from a string of replicas (images) denoted as $[\mathbf{R}_0, \mathbf{R}_1, \mathbf{R}_2, ..., \mathbf{R}_N]$ that are a linear interpolation of the reactants and products. Each image is then relaxed towards the MEP. To prevent the images from

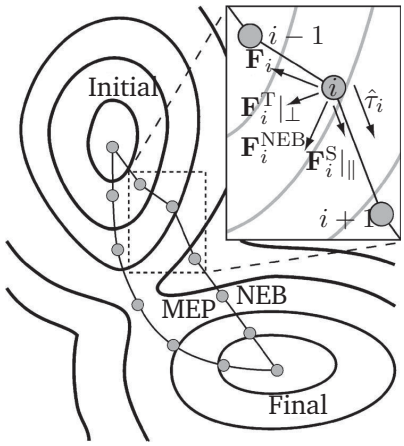

Figure 2.8.: The nudged elastic band method, showing forces parallel and perpendicular along the migration path [4].

returning to the end points, they are connected by fictitious springs with spring constant κ. The force acting on each image (see Fig. 2.8) is the sum of the component of the spring force tangent to the elastic band and the component of the true force perpendicular to the elastic band. The perpendicular component of the spring force and the parallel component of the true force are not used:

$$\mathbf{F}_i^{\mathrm{NEB}} = \mathbf{F}_i^{\mathrm{S}}|_\parallel + \mathbf{F}_i^{\mathrm{T}}|_\perp \tag{2.24}$$

Henkelman and Jónsson [63, 65] proposed a simple scheme to estimate the tangent given by:

$$\boldsymbol{\tau}_i = \begin{cases} \boldsymbol{\tau}_i^+ & \text{if } E_{i+1} > E_i > E_{i-1} \\ \boldsymbol{\tau}_i^- & \text{if } E_{i+1} < E_i < E_{i-1} \end{cases} \tag{2.25}$$

where $\boldsymbol{\tau}_i^+ = \mathbf{R}_{i+1} - \mathbf{R}_i$ and $\boldsymbol{\tau}_i^- = \mathbf{R}_i - \mathbf{R}_{i-1}$. When an image is at an extremum $\boldsymbol{\tau}_i$ is then expressed as:

$$\boldsymbol{\tau}_i = \begin{cases} \boldsymbol{\tau}_i^+ \Delta E_i^{\max} + \boldsymbol{\tau}_i^- \Delta E_i^{\min} & \text{if } E_{i+1} > E_{i-1} \\ \boldsymbol{\tau}_i^+ \Delta E_i^{\min} + \boldsymbol{\tau}_i^- \Delta E_i^{\max} & \text{if } E_{i+1} < E_{i-1} \end{cases} \tag{2.26}$$

where:

$$\Delta E_i^{\max} = \max(|E_{i+1} - E_i|, |E_{i-1} - E_i|) \tag{2.27}$$

and:

$$\Delta E_i^{\min} = \min(|E_{i+1} - E_i|, |E_{i-1} - E_i|) \tag{2.28}$$

The tangents must be normalized by $\hat{\boldsymbol{\tau}}_i = \boldsymbol{\tau}_i / |\boldsymbol{\tau}_i|$.

The parallel component of the spring force, $\mathbf{F}_i^{\mathrm{S}}|_{\parallel}$, in Eq. 2.24 can be expressed as:

$$\mathbf{F}_i^{\mathrm{S}}|_{\parallel} = \kappa(|\mathbf{R}_{i+1} - \mathbf{R}_i| - |\mathbf{R}_i - \mathbf{R}_{i-1}|)\hat{\boldsymbol{\tau}}_i \tag{2.29}$$

and the perpendicular component of the true force, $\mathbf{F}_i^{\mathrm{T}}|_{\perp}$, is given by:

$$\mathbf{F}_i^{\mathrm{T}}|_{\perp} = -\nabla E(\mathbf{R}_i) + \nabla E(\mathbf{R}_i).\hat{\boldsymbol{\tau}}_i\hat{\boldsymbol{\tau}}_i \tag{2.30}$$

To achieve the real saddle point along the MEP, the image with the highest energy is made to move uphill by lifting the spring force and allowing the image to experience an inverted parallel component of the true force ($\mathbf{F}_i^{\mathrm{T}}|_{\parallel}$):

$$\mathbf{F}_{\mathrm{imax}}^{\mathrm{climb}} = \mathbf{F}_i^{\mathrm{T}}|_{\perp} - \mathbf{F}_i^{\mathrm{T}}|_{\parallel} \tag{2.31}$$

This modification is know as the climbing image-NEB (CI-NEB) [4, 65].

Part I.

Perfect Lattice Properties of Germanium and III-V Semiconductors

3. Germanium and III-V: Perfect Lattice Properties

3.1. Introduction

In this chapter, the perfect crystal properties of the semiconductors covered in this thesis i.e. Ge and III-V semiconductors will be studied.

Ge and III-V semiconductors exhibits the diamond or the zinc blende structure respectively with space groups Fd$\bar{3}$m or F$\bar{4}$3m. The two structures are very similar, both are made up of two interpenetrating face centred cubic lattices (FCC). In the case of Ge, a primitive cell consists of 2 Ge atoms located at $(0,0,0)$ and $a_0(\frac{1}{4},\frac{1}{4},\frac{1}{4})$ (see Fig. 3.1). The lattice vectors are given by:

$$\mathbf{a}_1 = \frac{a_0}{2}\begin{pmatrix}0\\1\\1\end{pmatrix}, \quad \mathbf{a}_2 = \frac{a_0}{2}\begin{pmatrix}1\\0\\1\end{pmatrix}, \quad \text{and} \quad \mathbf{a}_3 = \frac{a_0}{2}\begin{pmatrix}1\\1\\0\end{pmatrix} \tag{3.1}$$

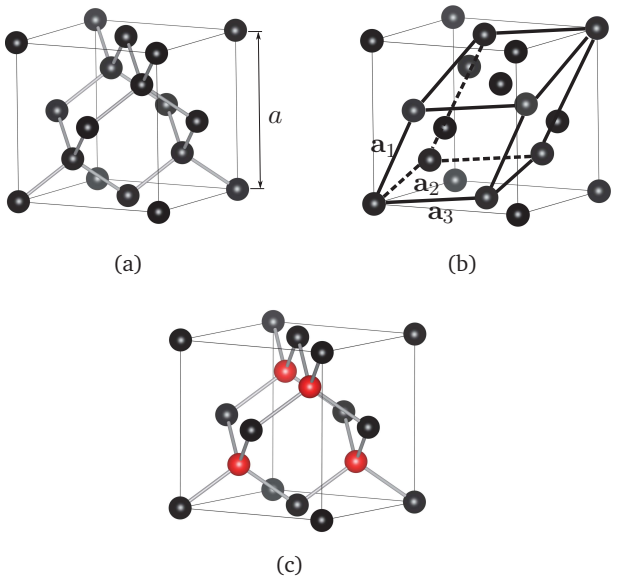

Figure 3.1.: Diamond crystal structure, showing (a) the unit cell and (b) the primitive cell. The zinc blende structure is shown in (c).

Binary III-V semiconductors have the same structure and lattice vectors however, the basis is made up from two different atoms, one group III and one group V atom in each case.

The reciprocal lattice vectors are related to their real space counterparts via:

$$\mathbf{b}_1 = \frac{2\pi \mathbf{a}_2 \times \mathbf{a}_3}{\mathbf{a}_1.(\mathbf{a}_2 \times \mathbf{a}_3)},\ \mathbf{b}_2 = \frac{2\pi \mathbf{a}_3 \times \mathbf{a}_1}{\mathbf{a}_1.(\mathbf{a}_2 \times \mathbf{a}_3)},\ \mathbf{b}_3 = \frac{2\pi \mathbf{a}_1 \times \mathbf{a}_2}{\mathbf{a}_1.(\mathbf{a}_2 \times \mathbf{a}_3)} \tag{3.2}$$

The primitive reciprocal space cell (i.e. the first Brillouin zone) of a FCC structure with the most important high symmetry points is shown in Fig. 3.2. The coordinates of these points are listed in Table 3.1.

3.2. Ge: Perfect Lattice Properties

Ge proved to be difficult to model in the standard framework of DFT as the band gap is closed and thus it is predicted to be a metal. This difficulty arises, as has

Table 3.1.: High symmetry points and their coordinates in reciprocal and Cartesian coordinates.

Point	Reciprocal coordinates (units of $\mathbf{b}_1$,$\mathbf{b}_2$,$\mathbf{b}_3$)	Cartesian coordinates (units of $\frac{2\pi}{a}$)
Γ	0 0 0	0 0 0
X	$\frac{1}{2}$ 0 $\frac{1}{2}$	0 1 0
W	$\frac{1}{2}$ $\frac{1}{4}$ $\frac{3}{4}$	$\frac{1}{2}$ 1 0
L	$\frac{1}{2}$ $\frac{1}{2}$ $\frac{1}{2}$	$\frac{1}{2}$ $\frac{1}{2}$ $\frac{1}{2}$

been discussed in Chapter 2, from the inadequate description of the exchange functional in LDA or GGA.

The band structure obtained from such calculations is shown in Fig. 3.3(a). The top of the valence band is composed of *p*-orbitals which are incorrectly raised in energy when described by LDA or GGA alone causing the already small band gap to dramatically shrink or be closed altogether. To correct this, schemes have been devised in which an energy term U has been added into the description of the electronic structure to account for this deficiency.

A correct band structure is important in order to describe defect levels and charge transitions across the band gap. To correct the band gap a range of values for U and J were tested and applied to the *p*-orbitals. Here, U and J specify the effective on-site Coulomb and exchange interaction parameters as described by Dudarev *et al*. [66] and implemented in VASP. It was found that a setting of $U = 0$ and $J = 3.33$ eV gives an indirect band gap of 0.74 eV which is in exact agreement with experimental data. This is shown in Fig. 3.3(b).

Recently, a family of hybrid functionals due to Heyd, Scuseria and Ernzerhof (HSE06) [43, 44] have been demonstrated and shown to accurately reproduce the electronic structure and the lattice properties for a range of semiconduc-

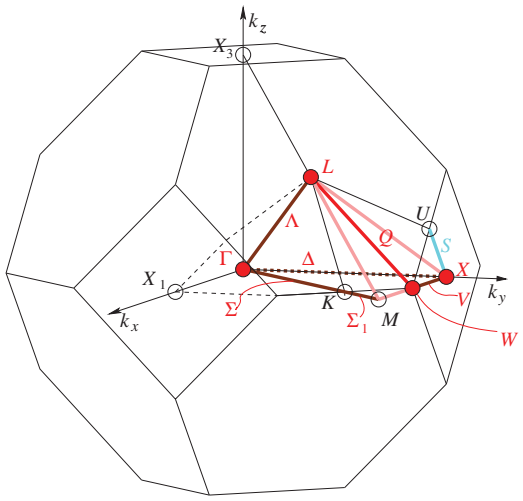

Figure 3.2.: The Brillouin zone of a FCC structure showing the high symmetry points and the paths connecting them. Courtesy of [5]

Table 3.2.: The band gap and lattice parameter of Ge calculated using the GGA, GGA+U and HSE06 functionals compared to experimental data.

	GGA	GGA+U	HSE06	Exp
Band gap (eV)	0	0.74	0.75	0.74 [70]
Lattice parameter (Å)	5.78	5.60	5.71	5.66 [71]

tors [67–69]. The effect this has on the electronic structure of Ge is shown in Fig. 3.3(c). Here, the indirect band gap is reproduced with a gap of 0.75 eV which is in excellent agreement with the experimental band gap at 0 K.

With the GGA functional, the lattice parameter is calculated to be 5.78 Å which is 2.22% higher than the experimental value calculated by Singh which is 5.66 Å when extrapolated to 0 K [71]. This overestimation in lattice parameters is typical of GGA functionals. The GGA+U approach gives a lattice parameter of 5.60 Å which is 1.03 % smaller than the experimental value. This reduction in the lattice parameter can be attributed to a higher degree of binding in Ge introduced by the U correction. HSE06 reproduces a lattice parameter of 5.71 Å which is 0.97 % higher than the experimental value. The band gaps and lattice parameters for the different functionals are summarised in Table 3.2. In Chapter

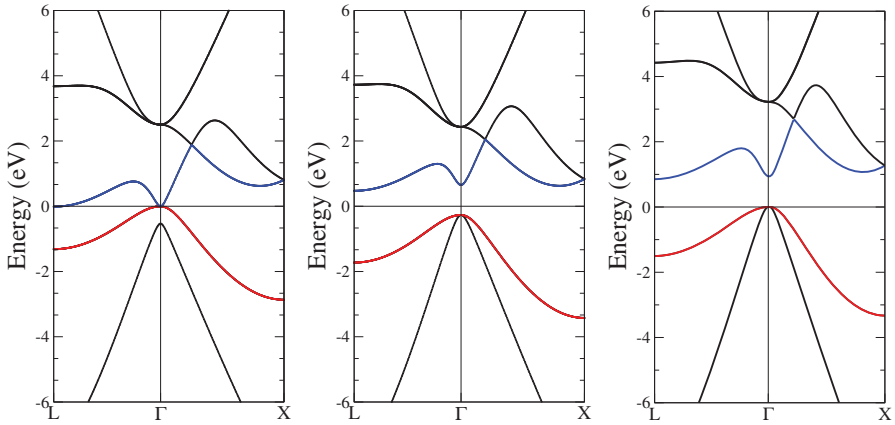

(a) GGA (b) GGA+U (c) HSE06

Figure 3.3.: Ge band structure calculated using different functionals. The GGA severely underestimates the band gap as is shown in (a) in which Ge is predicted to be a *metal*. On the other hand, (b) GGA+U and (c) HSE06 can accurately reproduce the band structure. Bands coloured in red represent the highest occupied valence band while the blue coloured ones represent the empty conduction band minima.

6 we compare GGA, GGA+U and HSE06 and show that GGA+U and HSE06 exhibit an agreement in terms of the densities of states and binding energies of the studied defects in Ge.

3.3. III-V: Perfect Lattice Properties

The III-V family of semiconductors is made from the six elements shown in Figs. 3.4(a)-3.4(f). These binary compound semiconductors are usually fabricated using techniques such as metal organic chemical vapour deposition (MOCVD) [72–74], molecular beam epitaxy (MBE) [75, 76] or atomic layer deposition (ALD) [77]. These techniques can be extended to fabricate ternary and quaternary III-V compounds.

The electronic structure description of these semiconductors suffers when studied using local or semi-local functionals. This did not stop years of research to

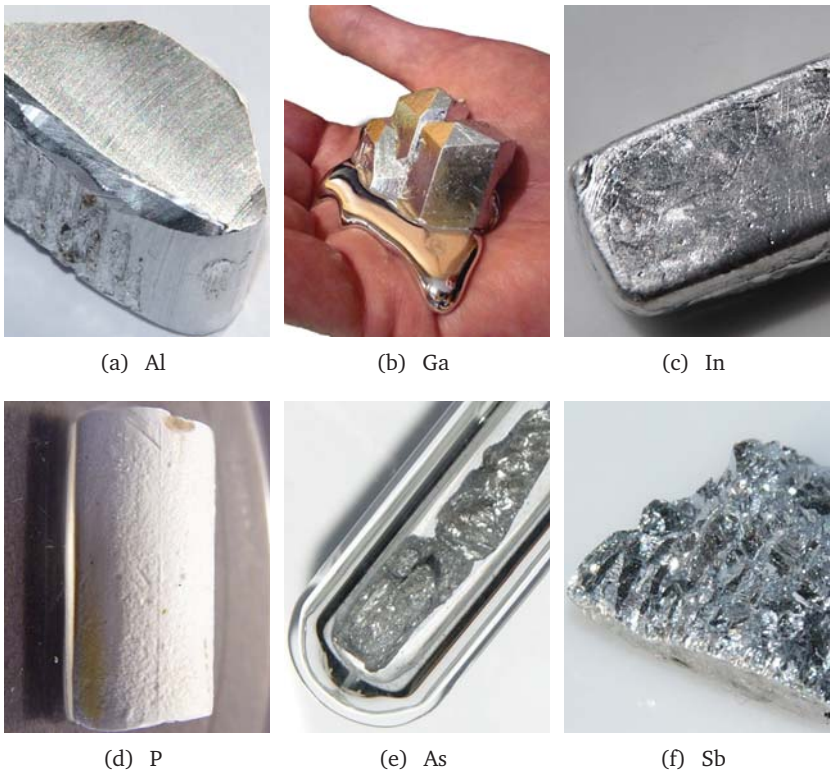

(a) Al (b) Ga (c) In

(d) P (e) As (f) Sb

Figure 3.4.: Constituents of III-V semiconductors in their elemental state. Images courtesy of [6].

be carried out on these materials using standard DFT producing many important and ground breaking results [78]. In the coming sections results regarding electronic, lattice, elastic and thermodynamic properties of these semiconductors using GGA and HSE06 will be presented and compared to experimental findings.

3.3.1. Electronic Properties

The calculated band gaps using GGA and HSE06 are shown in Fig. 3.5 and 3.6 respectively. The first four compounds are correctly reproduced to be indirect band gap materials as has been proven experimentally. AlP and AlAs have their conduction band minimum valley at the high symmetry point X in the Brillouin

zone, whereas, in AlSb and GaP this occurs at L. All other materials are predicted to have direct band gaps. Severe underestimation is observed for GaAs, InAs and InSb with GGA. On the other hand, HSE06 with the default 25% Hartree-Fock exchange mixing overestimates the band gaps in several cases such as AlP and AlAs. It is therefore customary to adjust the mixing parameter to fit the desired band gap. These values along with the experimental ones are given in Table 3.3.

Table 3.3.: The band gaps of III-V semiconductors calculated using PBE and HSE06 compared to experimental values [1]. Values in bold indicate an indirect band gap.

	Band gap (eV)		
System	PBE	HSE06	Exp
AlP	**1.63**	**3.80**	**2.51**
AlAs	**1.50**	**2.64**	**2.30**
AlSb	**1.23**	**1.73**	**1.70**
GaP	**1.51**	**2.41**	**2.40**
GaAs	0.05	1.35	1.53
GaSb	0.20	0.75	0.78
InP	0.41	1.47	1.41
InAs	···	0.41	0.43
InSb	···	0.31	0.23

The dielectric constants were calculated using density functional perturbation theory (DFPT) [79, 80] as implemented in VASP. In general there is a good agreement between the GGA and the HSE06 results on one side and the experimental data on the other.

To follow any trends in the properties of III-V semiconductors, the compounds are divided them into three families:

(a) Aluminium-V compounds

(b) Gallium-V compounds

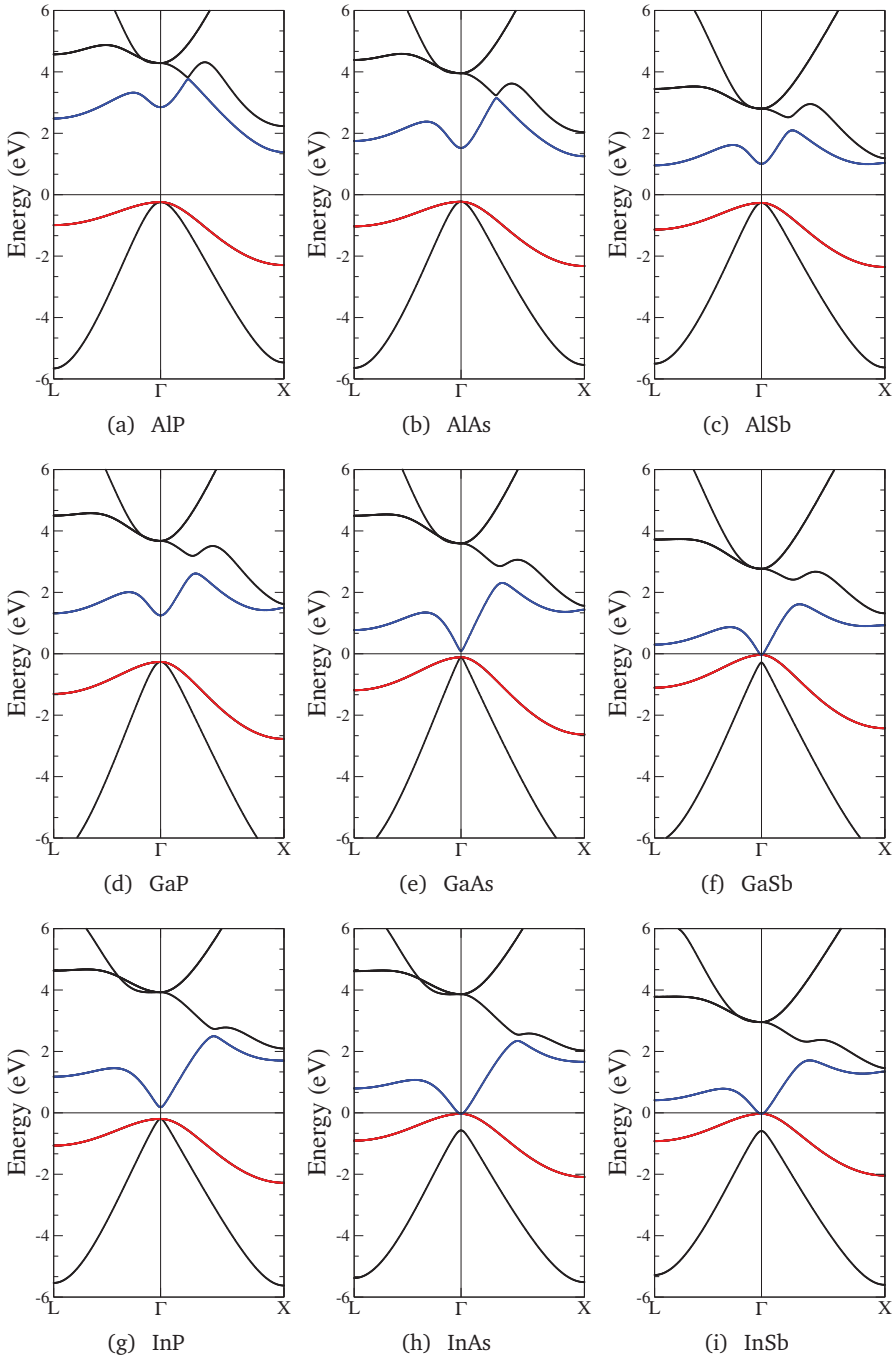

Figure 3.5.: Calculated band structures of III-V semiconductors using GGA.

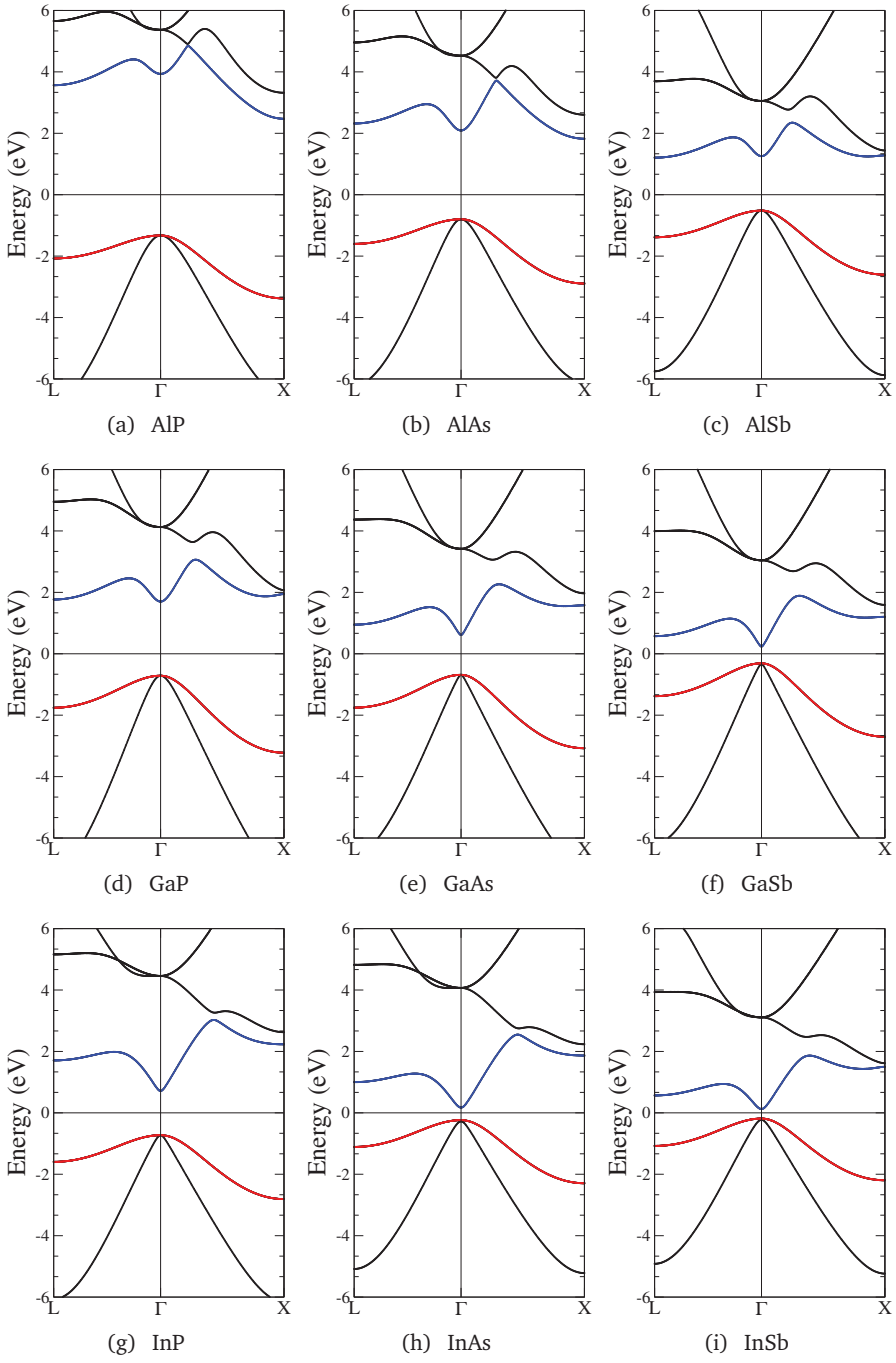

Figure 3.6.: Calculated band structures of III-V semiconductors using HSE06.

(c) Indium-Ⅴ compounds

This way of categorising these compounds will be used extensively when studying the formation of vacancies and antisites in them in Chapters 9 and 10.

Table 3.4.: The static dielectric constants of Ⅲ-Ⅴ semiconductors calculated using PBE and HSE06 compared to experimental values [1].

	Dielectric constant		
System	PBE	HSE06	Exp
AlP	7.69	8.84	9.80
AlAs	9.08	9.01	...
AlSb	12.68	12.75	11.21
GaP	9.70	10.32	10.75
GaAs	14.02	13.22	12.90
GaSb	16.95	16.81	15.70
InP	10.82	10.94	12.61
InAs	15.75	15.61	15.15
InSb	18.74	18.91	17.88

The trend observed in the dielectric constants, both from a computational and experimental points of view, is that the dielectrics increase across any given family. An interesting point to note is that GGA and HSE06 tend to overestimate the dielectric constants except for the phosphides (AlP, GaP and InP) whose values are always underestimated.

3.3.2. Lattice Properties

The lattice parameters are shown in Table 3.5. As was mentioned earlier, it is typical for PBE functionals to overestimate lattice parameters. Overall, HSE06 performs better than PBE in reproducing lattice parameters that are in better agreement with experimental values.

Table 3.5.: The lattice parameters of III-V semiconductors calculated using PBE and HSE06 compared to experimental values [1].

Lattice parameters (Å)			
System	PBE	HSE06	Exp
AlP	5.51	5.49	5.46
AlAs	5.73	5.71	5.66
AlSb	6.23	6.20	6.14
GaP	5.53	5.49	5.45
GaAs	5.76	5.71	5.65
GaSb	6.22	6.18	6.10
InP	6.00	5.91	5.86
InAs	6.21	6.12	6.05
InSb	6.65	6.56	6.47

3.3.3. Elastic Properties

The zinc blende structure exhibited by III-V semiconductors has three independent elastic constants c_{11}, c_{12} and c_{44} which are listed in Table 3.6. The elastic constants are computed via a stress-strain approach as implemented in VASP [81]. This is done by distorting the lattice and deriving the elastic constants from the stress tensor. For a cubic system, the relevant equations [82, 83] are:

$$B = \frac{1}{3}(c_{11} + 2c_{12}) = \frac{\partial \sigma_{11}}{\partial \epsilon_{11}} \tag{3.3}$$

$$\frac{1}{2}(c_{11} - c_{12}) = -\frac{1}{2}\frac{\partial \sigma_{33}}{\partial \epsilon_{33}} \tag{3.4}$$

$$c_{44} = \frac{1}{2}\frac{\partial \sigma_{12}}{\partial \epsilon_{12}} \tag{3.5}$$

As seen in Table 3.6, there is no superiority for one functional over the other when describing elastic parameters.

Table 3.6.: The elastic constants (c_{11}, c_{12} and c_{44}) of III-V semiconductors calculated using PBE and HSE06 compared to experimental values [1].

	c_{11} (GPa)			c_{12} (GPa)			c_{44} (GPa)		
	PBE	HSE06	Exp	PBE	HSE06	Exp	PBE	HSE06	Exp
AlP	132.35	140.13	132.00	67.88	68.78	63.00	61.75	67.03	61.50
AlAs	112.75	120.03	125.00	58.71	59.04	53.40	52.60	57.73	54.20
AlSb	84.91	90.72	89.39	45.03	45.46	44.27	37.66	40.97	41.55
GaP	139.61	148.23	141.20	69.42	69.67	62.53	66.07	71.74	70.47
GaAs	115.33	123.29	118.77	57.91	57.41	53.72	54.76	60.40	59.44
GaSb	86.12	92.72	88.39	43.15	42.90	40.33	39.93	44.30	43.16
InP	103.14	109.64	102.2	67.29	68.21	57.60	40.03	44.75	46.00
InAs	86.92	93.05	83.29	56.44	56.53	45.26	34.20	38.84	39.59
InSb	67.27	72.23	67.20	42.02	42.10	36.70	26.86	30.20	30.20

For AlP, PBE gives the best description of c_{11}, c_{12} and c_{44}, whereas for AlAs it can correctly describe c_{12} and c_{44}. HSE06 agrees well with experimental data in describing the parameters for AlSb. For the rest of the semiconductors, some parameters are described better with one functional than other. The most obvious example is InSb. Here, PBE agrees remarkably well in reproducing c_{11} but fails in reproducing c_{44} in which case HSE06 gives the same value as experiment. For the c_{12} parameter both functionals give the same value of about 42 GPa which differs from the 36.70 GPa obtained experimentally.

The bulk moduli are computed from elastic constants using Eq. 3.3. These are shown in Table 3.7 for which the calculated values obtained using GGA and HSE06 along with experimental values are given. With the exception of AlSb, GGA is closer to experiment than HSE06.

3.3.4. Thermodynamic Properties

The Gibbs free energy of formation of one formula unit of a compound is calculated using the total energy of the compound and its constituent elemental solids

Table 3.7.: The bulk moduli of III-V semiconductors calculated using PBE and HSE06 compared to experimental values [1].

	Bulk moduli (GPa)		
	PBE	HSE06	Exp
AlP	89.37	92.56	86.00
AlAs	76.72	79.37	77.27
AlSb	58.32	60.55	59.31
GaP	92.82	95.86	88.75
GaAs	77.05	79.37	75.40
GaSb	57.47	59.51	56.35
InP	79.24	82.02	72.47
InAs	66.60	68.70	57.94
InSb	50.44	52.14	46.87

as:

$$\Delta G_{\text{compound}} = \mu^{\text{bulk}}_{\text{compound}} - \sum_{\text{elements}} \mu^{\text{bulk}} \tag{3.6}$$

where $\mu^{\text{bulk}}_{\text{compound}}$ and μ^{bulk} are the chemical potential of one formula unit of the compound and the chemical potential of an atom in its stable solid state, respectively.

Table 3.8.: Calculated Gibbs free energy of formation of III-V semiconductors in comparison with experimental values [1].

	ΔG (eV/formula unit)		
System	PBE	HSE06	Exp
AlP	−1.32	−1.57	−1.73
AlAs	−0.98	−1.27	−1.25
AlSb	−0.33	−0.52	−0.52
GaP	−0.86	−1.10	−0.91
GaAs	−0.70	−0.95	−0.74
GaSb	−0.32	−0.46	−0.43
InP	−0.48	−0.65	−0.92
InAs	−0.49	−0.69	−0.61
InSb	−0.26	−0.38	−0.32

Overall, HSE06 is more adequate in describing the III-V Gibbs free energy of formation than the PBE. The two exceptions are GaP and GaAs for which PBE agrees within 0.05 eV and 0.04 eV with the experimental values respectively. For InSb on the other hand, both functionals show an error of 0.06 eV from the experimental values in which PBE underestimates whereas HSE06 tends to overestimate ΔH_{InSb}. In general, values obtained with GGA are all within the level of accuracy expected using this level of accuracy such as the work of Delly *et al.* [84] or Jain *et al.* [85].

3.4. Conclusions

In this chapter, the perfect lattice properties of Ge and III-V semiconductors were investigated. The performances of GGA, GGA+U and HSE06 were compared for Ge. The incorrect description of the electronic structure is amended by employing GGA+U and HSE06. These two approaches give the correct band gap and are able to reproduce lattice parameters in very good agreement with experiments.

III-V semiconductors suffer from the band gap problem when using the GGA. This is not entirely resolved by using HSE06 with the default Hartree-Fock exchange portion ($\alpha = 0.25$), as some of the band gaps are overestimated. No clear superiority of one functional over the other is exhibited when describing the dielectric and elastic properties (although HSE06 is slightly better for Gibbs free energy of formation), making the choice of the less computationally demanding GGA functional somewhat justifiable in later chapters.

Parts of this chapter have been published in Tahini *et al.* J. Phys.: Condens. Matter **24**, 195802 (2012) [86].

4. Strain-Induced Changes to the Electronic Structure of Germanium

4.1. Introduction

Ge is an indirect band gap material so an electron transits from an energy level in the conduction band to a level in the valence band mainly via phonon assisted non-radiative recombination. Direct optical recombination is slow and inefficient.

To enhance optical recombination rates, it would be desirable to find a way to force Ge to have a direct gap. Some results have been achieved by growing Sn_xGe_{1-x} alloys on Si where a direct band gap of 0.41 eV was obtained with a Sn content of 14% [87]. The correlation between the structure and the electronic properties of semiconductors means that these properties can also be en-

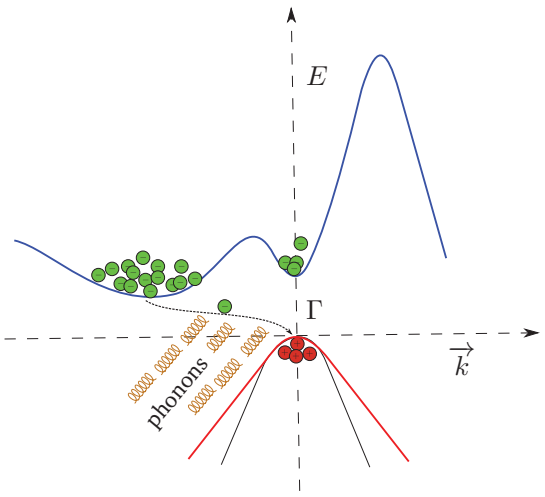

Figure 4.1.: A schematic of the band structure of Ge, showing the valence band and the conduction band valleys. A non-radiative electron-hole recombination due to the indirectness of the band gap results in lattice vibrations manifested as phonons.

gineered by applying deformations to the material. Uniaxial and biaxial strains have been studied and applied extensively in Si to increase the carrier mobilities for integrated circuit applications [88]. Typically biaxial strain in Si enhances the carrier mobility; however, the gains diminish at high vertical electric fields [89]. The enhancement of mobility is maintained for uniaxially strained Si [90]. The deformation potential theory has been widely and successfully used to study the electronic properties of semiconductors [91–93]. Niquet *et al.* [94] used a model for the onsite matrix elements of the $sp^3d^5s^*$ tight binding Hamiltonian, to study the effect of strain on Si, Ge and their alloys. They complemented their results with post-DFT (LDA) GW corrected calculations. This model was used to calculate the band energies for the (001), (110), and (111) biaxial strain as well as the deformation potentials for Si and Ge. For the latter, their model showed an agreement between the LDA and experimental results in the case of Si but deviated to a larger extent in the case of Ge. Lim *et al.* [95] studied the emission characteristics of Ge micromechanical structures under tensile biaxial stain. According to their simulations they found out that while at 1.5 % strain Ge was still an indirect band gap material a net optical gain could be achieved with an

electron-hole injection of 9×10^8 cm^{-3}. Recent similar experimental findings by Camacho-Aguilera *et al.* showed direct band gap narrowing in highly doped n-type Ge [96] and similar work by Carroll *et al.* [97] and by Schmid *et al.* [98]. Kurdi *et al*. [99], employing the $\mathbf{k}.\mathbf{p}$ formalism, concluded that for biaxial (001) tensile strained Ge the crossover from indirect to direct occurs at 1.9%.

Recently, Murphy-Armando and Fahy [100] used electronic structure calculations to show that electron mobilities can be enhanced several hundred times for thin Ge films (strained biaxially parallel to (001)) and $5 - 20$ times (strained uniaxially along [111]) in Ge nanowires. In this chapter, we use DFT to investigate the effects of biaxial and uniaxial strain on the indirect to direct band gap transition in bulk Ge.

4.2. Methodology

The band structure calculations were performed using DFT as implemented in the Vienna ab-initio Simulation Package (VASP) code [55, 101]. Electron exchange and correlation were described using the PBE functional [37]. The electrons occupying the $4s^2 4p^2$ states were treated as valence, whereas the [Ar]3d^{10} were approximated by a pseudopotential generated according to the PAW method [54]. A primitive cell is used with 2 Ge atoms as basis located at (0,0,0) and $(\frac{1}{4}, \frac{1}{4}, \frac{1}{4})$. For such a cell a $10 \times 10 \times 10$ k-point grid is used which is generated according to the Monkhorst-Pack scheme to sample the Brillouin zone [38]. To obtain the bandstructure, the high symmetry paths linking $\mathrm{L} \rightarrow \Gamma \rightarrow \mathrm{X}$ were sampled using 200 $\mathbf{k}$-points for each segment which was enough for the resolution of such calculations. The kinetic energy cutoff was set to 400 eV, yielding a converged total energy (Sec. 2.2.2) with SCF tolerance set to 1×10^{-5} eV. To simulate the strain in the cells the deformed lattice parameters were held fix and only the atoms' positions were allowed to relax such that the forces on them

were below 0.001 eV/Å. To correct the underestimation of the band gap (typical for GGA), a GGA+U approach is employed by setting the on-site Coulomb parameter, U, to 0 eV and the on-site exchange parameter, J, to 3.33 eV (see Sec.3.2). This results in a band gap of 0.74 eV for the unstrained Ge structures, which is in agreement with the experimental band gap. This method employed to correct for the band gap has been tested before and yielded accurate results in agreement with available experimental data. Its computational efficiency in comparison with hybrid functionals or post-DFT calculations (HSE06 or GW) and its ability to reproduce similar electronic structures in relaxed unstrained Ge make it a desirable choice.

Table 4.1.: Calculated lattice, elastic and electronic properties of Ge compared to experimental results.

	This work	Experimental
Lattice parameter (Å)	5.60	5.66 (extrapolated to 0 K) [71]
c_{11} (GPa)	128.1	128.35 (298 K) [102]
c_{12} (GPa)	46.1	48.23 (298 K) [102]
c_{44} (GPa)	69.7	66.66 (298 K) [102]
Indirect band gap, $\Gamma_c \rightarrow L_v$ (eV)	0.74	0.74 (4 K) [70]
Indirect band gap, $\Gamma_c \rightarrow X_v$ (eV)	0.89	...
Direct band gap, $\Gamma_c \rightarrow \Gamma_v$ (eV)	0.92	0.89 (10 K) [103]

For the unstrained Ge it is calculated that the difference in energy between the indirect and direct band gaps is 0.18 eV (close to the experimental value of 0.14 eV) [104]. The band gaps are measured from the top of the valence band at the Γ point to the lowest of the conduction band minima encountered along the paths between the high-symmetry points L, Γ and X in the reciprocal lattice. The minimum gaps closest to these three points are denoted E_g^L, E_g^Γ, and E_g^X, respectively. Notably, $E_g{}^X$ does not occur exactly at the X point but somewhere along the Δ path connecting the Γ and the X high symmetry points in the Brillouin zone. This description of the electronic structure leads to accurate lattice

and elastic properties of the material as shown in Table 4.1 where the DFT results are compared to previous experimental evidence [70, 71, 103, 105]. In general, by using the elasticity theory, strain is applied by first calculating the Poisson's ratio [106]:

$$D = -\frac{\epsilon_{\perp}}{\epsilon_{\parallel}} \tag{4.1}$$

where $\epsilon_{\perp}$ and $\epsilon_{\parallel}$ are the strain components perpendicular and parallel to the plane. D is dependent on the elastic constants and the nature of strain (biaxial or uniaxial) [106]. $\epsilon_{\perp}$ and $\epsilon_{\parallel}$ can be expressed as a function of strain tensor components when the perpendicular and parallel vectors to the plane of interest are known ($\upsilon_{\perp}$ and $\upsilon_{\parallel}$ respectively) [107]:

$$\epsilon_{\perp} = \vec{\upsilon}_{\perp}^{T}.\bar{e}.\vec{\upsilon}_{\perp}, \qquad \epsilon_{\parallel} = \vec{\upsilon}_{\parallel}^{T}.\bar{e}.\vec{\upsilon}_{\parallel} \tag{4.2}$$

where $\bar{e}$ is the strain tensor given by:

$$\bar{e} = \begin{bmatrix} e_{xx} & e_{xy} & e_{xz} \\ e_{yx} & e_{yy} & e_{yz} \\ e_{zx} & e_{zy} & e_{zz} \end{bmatrix} \tag{4.3}$$

For instance, [010] or [100] are two vectors parallel to the (001) plane while the perpendicular vector is [001]. By using Eq. 4.2 and Eq. 4.3 and assuming a uniform biaxial strain we get:

$$\begin{aligned} \epsilon_{\parallel} &= e_{xx} = e_{yy} \\ \epsilon_{\perp} &= e_{zz} = -D\epsilon_{\parallel} \end{aligned} \tag{4.4}$$

where for biaxial strain parallel to the (001) plane [106]:

$$D_{(001)}^{\text{biaxial}} = \frac{2c_{12}}{c_{11}} \tag{4.5}$$

This is used to adjust one or more of the lattice parameters to reproduce the desired strain, for which the new lattice vectors become [107, 108]:

$$\mathbf{a}_1 = a_0(1+\epsilon_{\parallel})\hat{\mathbf{x}}, \quad \mathbf{a}_2 = a_0(1+\epsilon_{\parallel})\hat{\mathbf{y}}, \quad \mathbf{a}_3 = a_0(1+\epsilon_{\perp})\hat{\mathbf{z}} \tag{4.6}$$

The above describes uniform biaxial strain parallel to the (001) plane which is the simplest of the strain cases considered here. A similar approach can be followed for the more complicated (110) and (111) planes. For example, the vector perpendicular to the (110) plane is:

$$\vec{v}_{\perp}^{T} = \left[\frac{1}{\sqrt{2}}\frac{1}{\sqrt{2}}0\right]^{T} \tag{4.7}$$

while the two parallel vectors are:

$$\vec{v}_{\parallel}^{T} = \left[\frac{1}{\sqrt{2}}\frac{-1}{\sqrt{2}}0\right]^{T} \text{ and } \vec{v}_{\parallel}^{T} = [001] \tag{4.8}$$

Using Eq. 4.2 one can show that for uniform biaxial strain parallel to the (110) plane:

$$\begin{aligned} \epsilon_{\perp} &= e_{xx} + e_{xy} \\ \epsilon_{\parallel} &= e_{xx} - e_{xy} = e_{zz} \end{aligned} \tag{4.9}$$

For which the strained lattice vectors become [107, 109]:

$$\begin{aligned} \mathbf{a}_1 &= \frac{a_0}{2}\left[-\left(\frac{\epsilon_{\parallel}-\epsilon_{\perp}}{2}\right)\hat{x} + \left(1+\frac{\epsilon_{\parallel}+\epsilon_{\perp}}{2}\right)\hat{y} + (1+\epsilon_{\parallel})\hat{z}\right] \\ \mathbf{a}_2 &= \frac{a_0}{2}\left[\left(1+\frac{\epsilon_{\parallel}+\epsilon_{\perp}}{2}\right)\hat{x} - \left(\frac{\epsilon_{\parallel}-\epsilon_{\perp}}{2}\right)\hat{y} + (1+\epsilon_{\parallel})\hat{z}\right] \\ \mathbf{a}_3 &= \frac{a_0}{2}(1+\epsilon_{\perp})(\hat{x}+\hat{y}) \end{aligned} \tag{4.10}$$

4.3. Results and Discussions

In the following subsections, the effect strain has on the band structure is discussed in terms of altering the energies of the two indirect band gaps ${E_g}^L$ and ${E_g}^X$ and the direct band gap ${E_g}^\Gamma$.

4.3.1. Biaxial Strain (001)

As the strain is applied biaxially parallel to the (001) plane all three band gaps drop for positive (tensile) strain and the ${E_g}^\Gamma$ and ${E_g}^X$ also drop for negative (compressive) strain. For the compressive strain ${E_g}^\Gamma$, and to a lesser extent ${E_g}^X$, exhibits a quadratic dependence on strain. ${E_g}^\Gamma$ increases initially with compression before starting to fall beyond -1% strain. The three band gaps fall but no cross-over between ${E_g}^\Gamma$ and ${E_g}^L$ occurs within the limits considered. At around -3% ${E_g}^X$ attains the minimum among the band gaps but Ge maintains an indirect band gap. Between 0 and 3.5% strain, the band gaps depend linearly on strain. Beyond this, however, the band edges show a remarkable deviation from the nearly linear dependence on strain, which is a behaviour not normally accounted for using deformation potential theories and results from the shear strain component [94]. The rate at which ${E_g}^\Gamma$ decreases is greater than the other two band gaps, and it becomes the lowest energy band gap at 1.7% at which point Ge changes from an indirect to a direct band gap material. This is in very good agreement with experiments carried out by Huo [110]. At this strain the direct band gap is about 0.47 eV which is 36% lower than the unstrained indirect band gap.

As strain is applied, the degeneracy in valence bands comprising light and heavy holes and split-off bands is lifted as can be seen in Fig. 4.3.

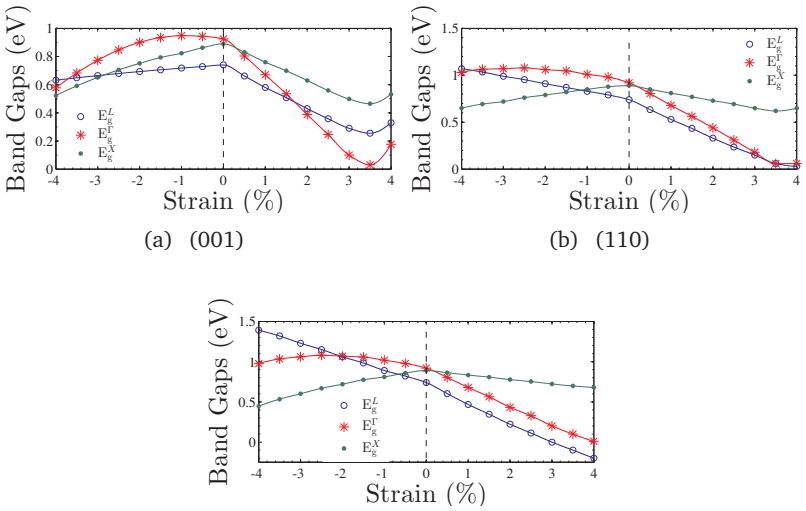

(a) (001) (b) (110)

(c) (111)

Figure 4.2.: The change in band gaps, $E_g{}^L$, $E_g{}^\Gamma$ and $E_g{}^X$ with biaxial strain parallel to the (001), (110) and (111) planes.

4.3.2. Biaxial Strain (110)

For compression parallel to the (110) plane E_g^L increases with strain rather than decreasing as in the (001) case. $E_g{}^\Gamma$ depends quadratically on strain increasing before it gradually starts falling again. Only $E_g{}^X$ drops linearly with compression until a minimum band gap at about -1.14%. Overall there is no transition to a direct band gap. For tensile strain, $E_g{}^\Gamma$ and $E_g{}^L$ decrease linearly, however, the decrease is not enough to make the gap direct. Only at 3.5 % do the two band gaps become nearly equal, beyond which they diverge once more and $E_g{}^L$ remains the minimum energy valley. Even if Ge were converted into a direct band gap material, the band gap would be about 0.1 eV, which is too small for solar or telecommunications applications.

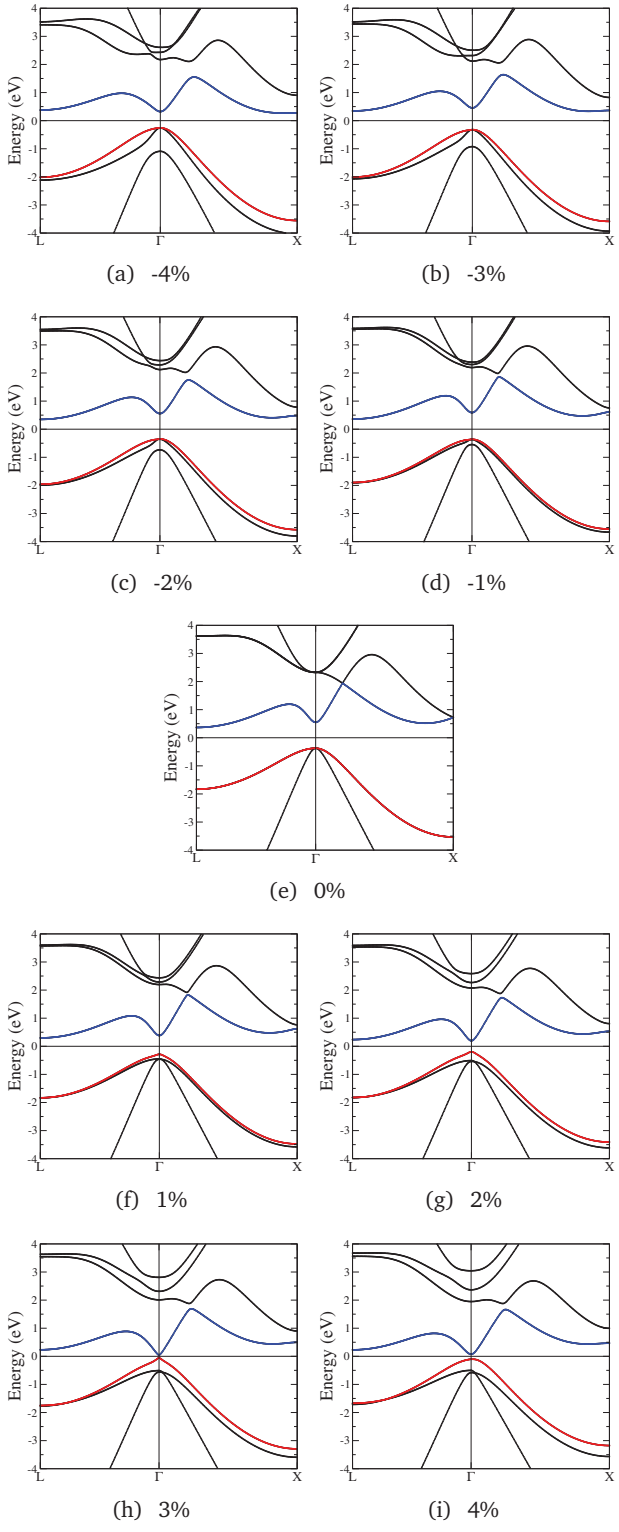

Figure 4.3.: The changes in the band structure of Ge when biaxial strain is applied parallel to the (001) plane.

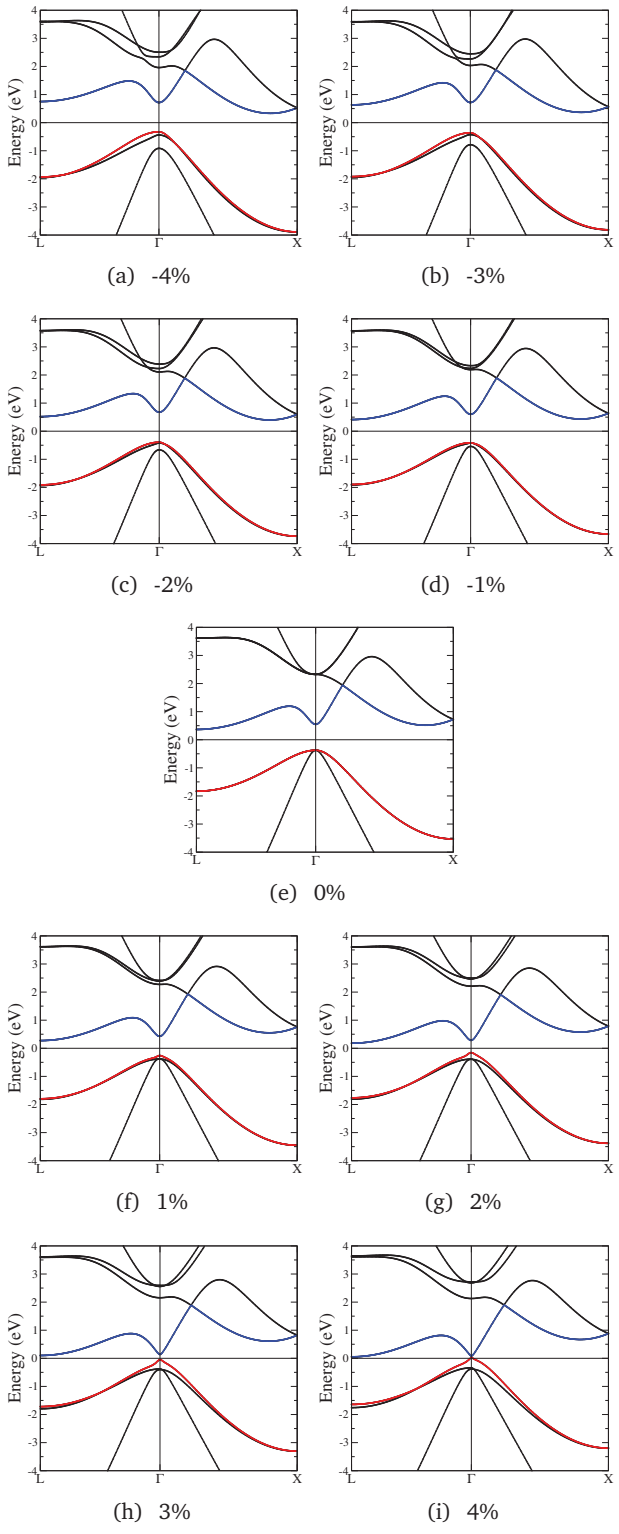

Figure 4.4.: The changes in the band structure of Ge when biaxial strain is applied parallel to the (110) plane.

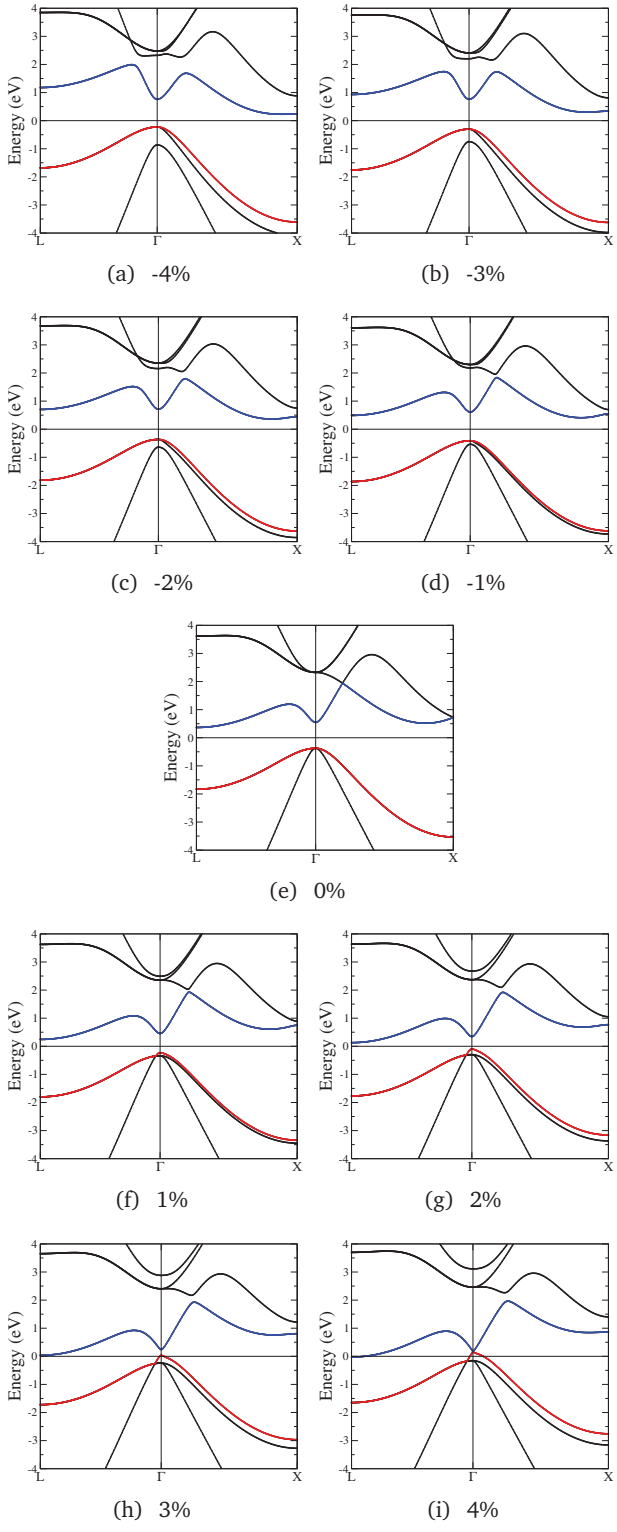

Figure 4.5.: The changes in the band structure of Ge when biaxial strain is applied parallel to the (111) plane.

4.3.3. Biaxial Strain (111)

For the (111) plane, compression leads to similar effects as with the (110) case. E_g^{Γ} exhibits a greater increase with strain but as before no transition in the band gap nature occurs. Under tensile strain $\mathrm{E_g}^{\Gamma}$ and $\mathrm{E_g}^{L}$ drop at nearly the same rate maintaining an energy difference of about 0.18 eV for any given strain level.

4.3.4. Uniaxial Strain [001]

For strain along the [001] direction, $\mathrm{E_g}^{L}$, $\mathrm{E_g}^{\Gamma}$, and $\mathrm{E_g}^{X}$ drop with both compression and tension. The rate at which $\mathrm{E_g}^{\Gamma}$ decreases is greater than the other two band gaps giving rise to a transition from indirect to direct at -2.41% and 3.05% where the direct band gaps are about 0.41 eV and 0.59 eV respectively. All the bands respond linearly to strain except $\mathrm{E_g}^{\Gamma}$ under tensile strain, in which case a quadratic behaviour is observed.

Compressive strain in the [001] direction allows a transition to a direct band gap. This is advantageous as it is more feasible to grow Ge on materials with smaller lattice constants (e.g. $\mathrm{Si}_{1-x}\mathrm{Ge}_x$).

4.3.5. Uniaxial Strain [110]

As strain is applied in tension parallel to [110], the three bands exhibit a varied response. $\mathrm{E_g}^{L}$ increases slowly whereas $\mathrm{E_g}^{X}$ remains nearly constant for the range of strain investigated as can be seen from Fig. 4.8. Only $\mathrm{E_g}^{\Gamma}$ drops with tensile strain. This leads to a band cross-over at 1.71 % strain with a direct band gap of 0.78 eV.

Under compression, however, the bands' energies decrease at nearly the same

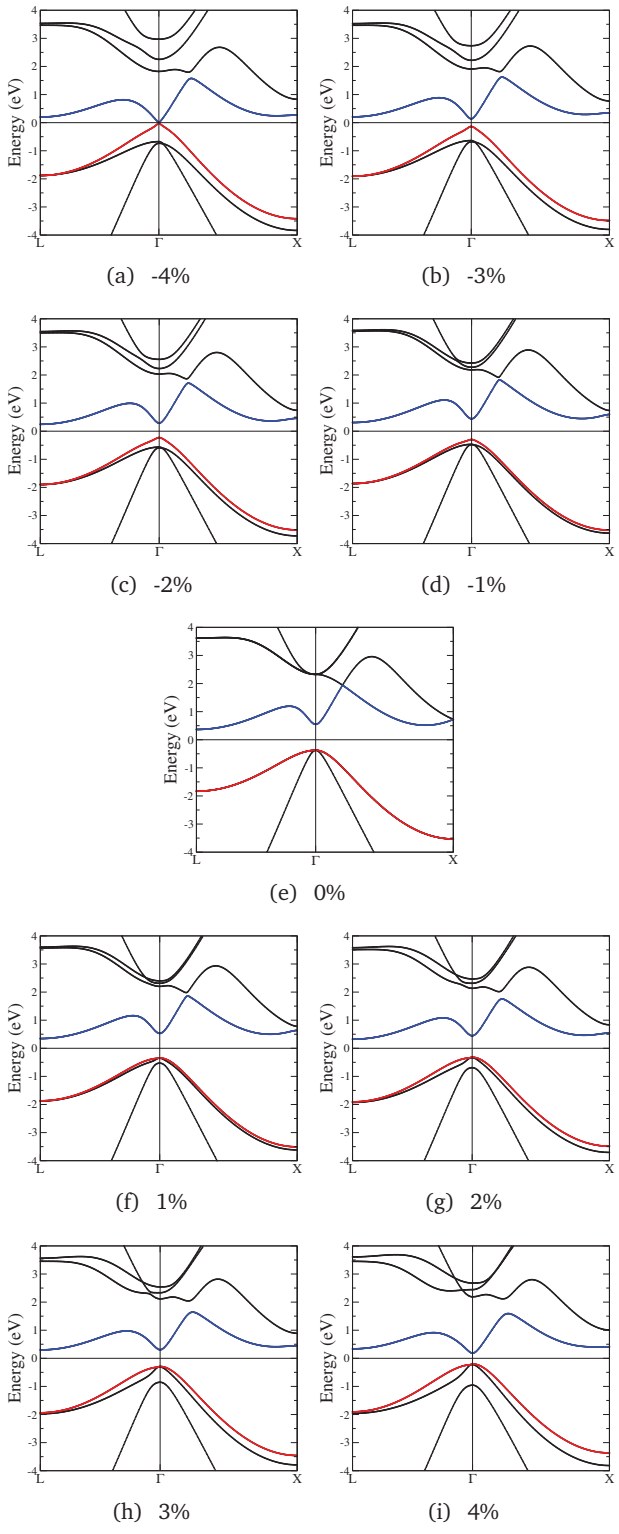

Figure 4.6.: The changes in the band structure of Ge when uniaxial strain is applied along the [001] direction.

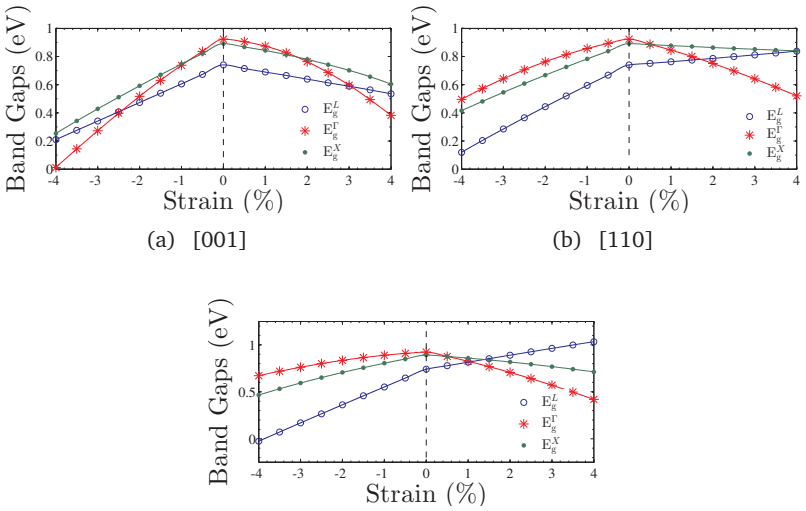

(a) [001] (b) [110]

(c) [111]

Figure 4.7.: The change in band gaps, $E_g{}^L$, $E_g{}^\Gamma$ and $E_g{}^X$ with uniaxial strain along the [001], [110] and [111] directions.

rate maintaining approximately equal energy barrier between them. This does not permit an indirect→direct band gap transition.

Tensile [110] strain does not have an appreciable effect on the degeneracy of the heavy and light hole bands under tensile strain and only the split-off band is lowered in energy as shown in Fig. 4.8. Compression on the other hand only affects the heavy holes leaving the light holes and split-off band degenerate.

4.3.6. Uniaxial Strain [111]

The [111] tensile strain allows a transition to direct band gap to occur at relatively small strains (compared with the other strain conditions considered), while at the same time maintaining a band gap that is large enough for practical use. This agrees qualitatively with recent work performed by Zhang *et al.* [111] Their finding was that 4.2% uniaxial strain along [111] is needed to convert Ge to a 0.34 eV direct band gap material. While this level of strain might be achiev-

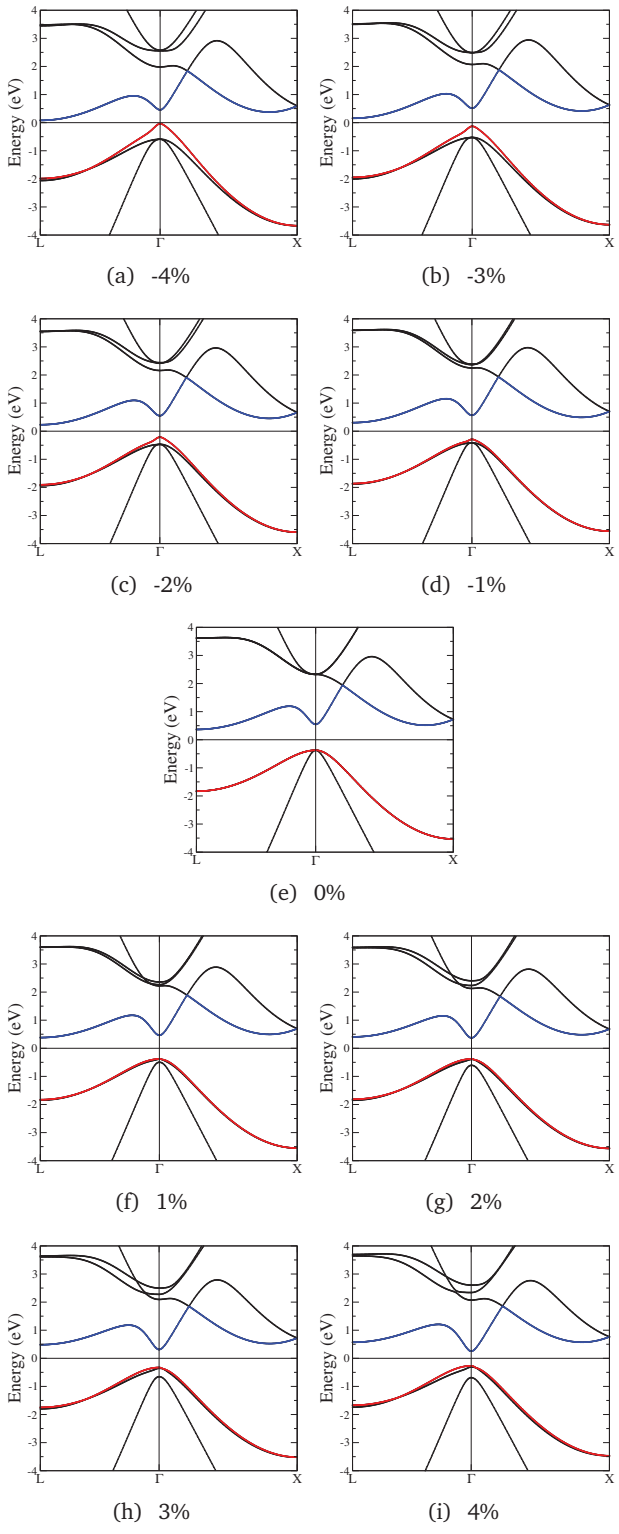

Figure 4.8.: The changes in the band structure of Ge when uniaxial strain is applied along the [110] direction.

able in nanowires, it has not been reported experimentally for bulk materials [112], and is beyond the limit of Si/Ge lattice mismatch.

Another complication in real materials arises due to the formation of cracks and the fact that the linearity of stress/strain relations breaks beyond a certain stress [112]. The results for [111] strain, are within the realm of what could be achieved experimentally.

4.3.7. Origin of the Changes in the Band Structure with Applied Strain

Figs. 4.3-4.9 show the changes induced in the conduction and valence band minima for the various strain conditions studied in this chapter. The valence band electrons of each Ge atom are composed of spherical s orbitals and directional p_x, p_y and p_z orbitals, with each atom forming tetrahedral bonds with its neighbours as shown in Fig. 4.10. These in-plane orbitals form the heavy holes, whereas out of plane orbitals form light holes [113]. Tensile or compressive strain causes elongations of bonds along one direction, shrinking in another and a change in the bonds' orientation. The result of this is a change in the orbitals' weights and interactions, which changes the energies of the heavy and light holes. The orbitals' rehybridization also affects the energies of the conduction band that is mainly composed of p electrons. Depending on the plane or direction and whether it is in compressive or tensile strain, these lead to a variation in the edges of the valence and conduction band minima and hence the width of the band gap.

4.3.8. Effective Masses

The effective mass was calculated using the relation $\frac{1}{m^*} = \frac{1}{\hbar^2}\frac{\partial^2 E}{\partial k^2}$. The required data are obtained from the band structure by approximating the curvature of

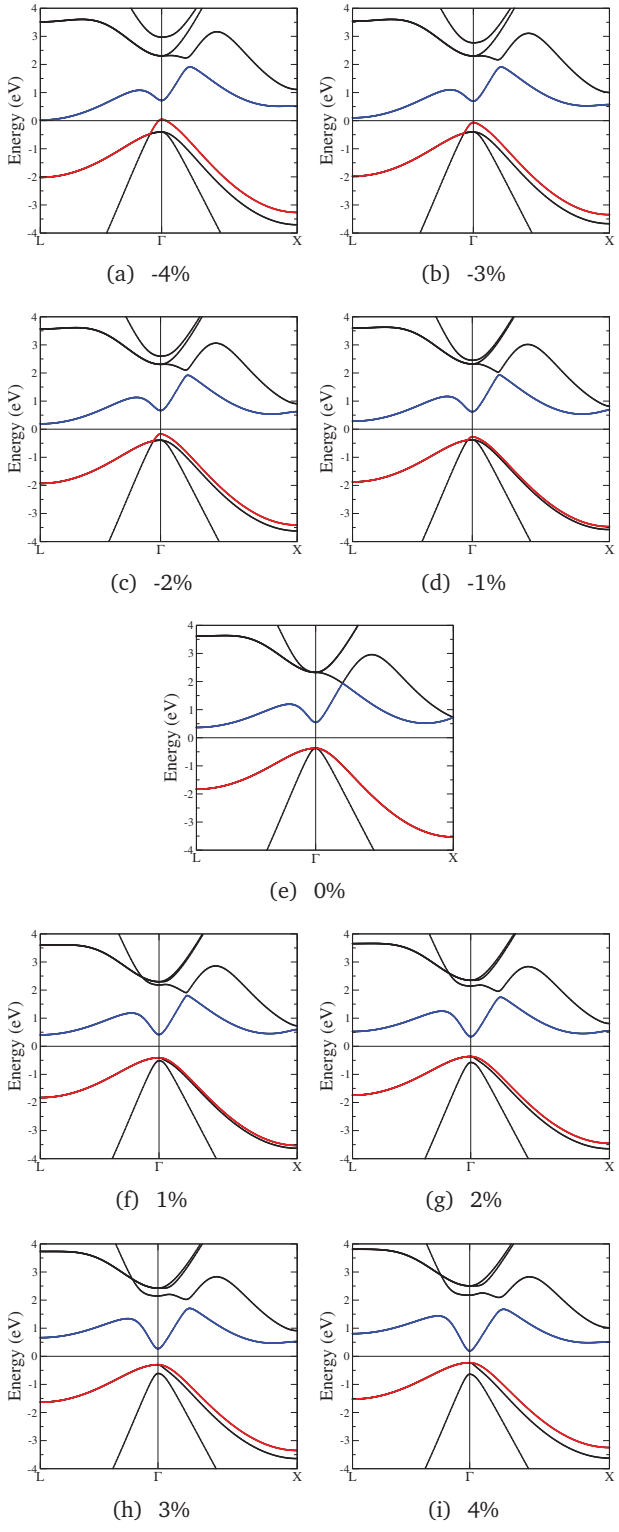

Figure 4.9.: The changes in the band structure of Ge when uniaxial strain is applied along the [111] direction.

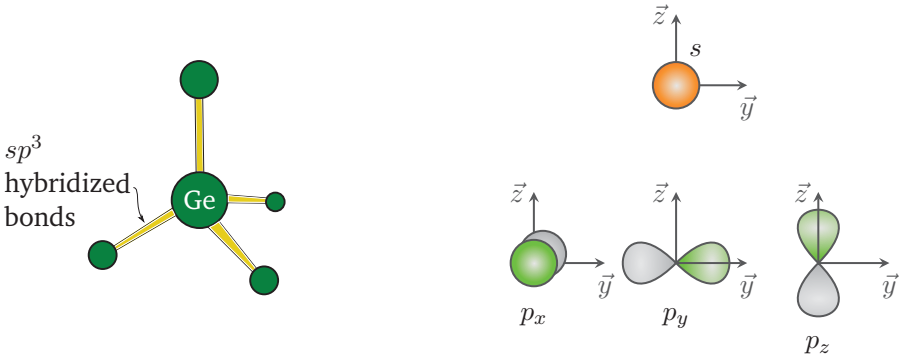

Figure 4.10.: A schematic of (a) the tetrahedral bonding in Ge and (b) the orbitals making up these bonds.

the energy eigenvalues by fitting the bandstructure $E(k)$ near the valence band maxima and conduction band minima to parabolas of the form $E(k) = ak^2 + bk + c$. The maxima and minima of interest are those at L(0.5,0.5,0.5) and Γ(0,0,0) from which we can calculate the electron effective masses m_e^{*L} and $m_e^{*\Gamma}$ and the hole's effective mass, $m_h^{*\Gamma}$. For unstrained Ge, calculations reveal that $m_e^{*L} \approx 1.79m_e$, $m_e^{*\Gamma} \approx 0.06m_e$ and $m_h^{*\Gamma} \approx 0.52m_e$, which are compared with the experimental values of $m_e^{*L} \approx 1.74m_e$, $m_e^{*\Gamma} \approx 0.038m_e$ [114, 115] and $m_h^{*\Gamma} \approx 0.35m_e$ [116].

At the point where Ge makes the transition to a direct band gap material the excited electrons in the conduction band, formed either thermally or by n-doping, start occupying the Γ valley, and scatter back to the valence band via this channel. The calculations are consistent with experimental [103, 111] results indicating that the electrons occupying the Γ valley have a much smaller effective mass than those occupying the L valley. Consequently an enhancement in the carrier mobility is expected when the transition occurs since it is inversely proportional to the effective mass of the carrier.

4.4. Summary

In summary, the impact of biaxial and uniaxial strain on the electronic structure of Ge was investigated. For tensile strains the band gap undergoes a transition from indirect to direct for biaxial strain parallel to the (001) plane and for uniaxial strains parallel to the [001], [110] and [111] directions. For compressive strain this transition occurs for the only uniaxial [001] direction. Uniaxial tensile strain parallel to the [111] direction transforms Ge to a direct band gap material at a relatively low strain.

Part II.

Defect Processes in Germanium

Parts of the work presented here appears in Tahini *et al.* Appl. Phys. Lett. **99**, 072112 (2011) [117] and Appl. Phys. Lett. **99**, 162103 (2011) [118].

5. Diffusion of E-Centres and Tin in Germanium

5.1. Introduction

Previous experimental [2, 119] and theoretical [120–122] studies provided evidence that donor atoms such as phosphorous (P), arsenic (As) and antimony (Sb) diffuse in Ge via their interaction with vacancies (V_{Ge}).

Notably, the V_{Ge} is the dominant defect as its formation energy is lower compared to the self-interstitials. Recent experimental work [2] determined that donor diffusion in Ge increases with the square of the free electron concentration. This strong doping dependence of diffusion is accurately described by neg-

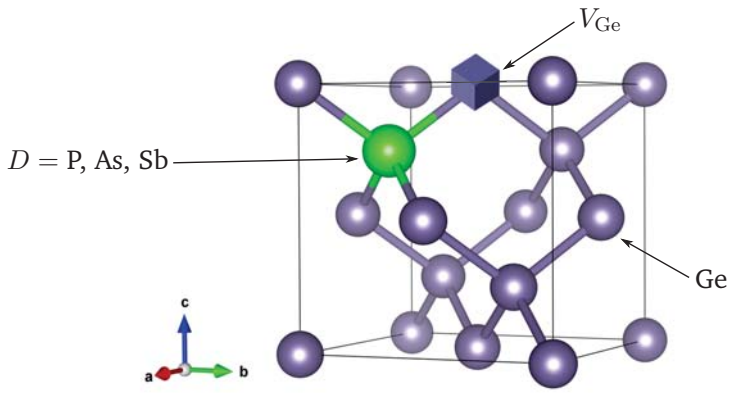

Figure 5.1.: An E-centre in which a dopant atom D (D=P, As or Sb) is coupled to a nearest neighbour V_{Ge}.

atively charged E-centres, $(DV_{\mathrm{Ge}})^{-1}$, which are formed via the reaction:

$$(DV_{\mathrm{Ge}})^{-1} \longleftrightarrow D_s^{+1} + V_{\mathrm{Ge}}^{-2} \tag{5.1}$$

where D_s^{+1} denotes the singly positively charged substitutional donor atom and V_{Ge}^{-2} the doubly negatively charged vacancy. The relevance of doubly negatively charged vacancies has been proved by means of donor diffusion in Ge isotope multilayer structures, which directly reveal the impact of doping on vacancy mediated self-diffusion in Ge.

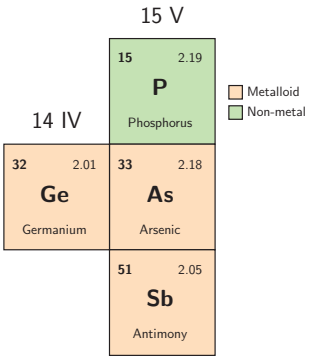

Figure 5.2.: The positions of Ge, P, As and Sb in the periodic table. The atomic numbers and electronegativities are shown in the upper left and right corners respectively.

From a theoretical viewpoint a previous DFT study has considered systematically only charge neutral E-centres [122], while another DFT study investigated only the PV_{Ge} pair [121]. These previous investigations were limited due to the incomplete description of the exchange-correlation by the GGA or LDA, which both led to severe underestimations of the band gap of Ge [123].

5.2. Methodology

In the present study we employ a GGA+U approach, which increases the band gap of Ge. This technique allows for the investigation of the energetics of both neutral and charged E-centres and other defects (or dopant-defect clusters) in Ge. The aim is to calculate the formation energies, binding energies and activation energies for diffusion of the technologically important E-centres in Ge.

The formation and binding energies of donor atoms (P, As, Sb) to V_{Ge} were calculated based on the DFT approach as implemented in the VASP [55, 101]. The pseudopotentials are generated by the PAW method [54]. The exchange and correlation are described using the PBE functional [37]. The Ge core states that were approximated by a pseudopotential are [Ar]$3d^{10}$, whereas the $4s^2 4p^2$ states were explicitly treated as valence electronic states. Integrations over the Brillouin zone were carried out using a $4 \times 4 \times 4$ k-point set generated according to the Monkhorst-Pack scheme [38] using a 64 atom supercell. This cell size has been employed in a number of previous studies [120, 122, 124, 125]. Previous studies [124, 125], for example, showed that the use of a 256 atom cell changed the defect energies by about 1.5%, which provides an estimate of the cell size related uncertainty for the present simulations. The cutoff energy is 400 eV which yields a converged total energy to within 2 meV (see Sec. 2.2.2). Self-consistency was achieved by restricting the change in total energy to no more than 1×10^{-5} eV, whereas the forces were relaxed to below 0.001 eV/Å.

While the GGA+U approach used here is able, potentially, to generate a band gap in predicted structures, it is only a first order correction but has the advantage of being very efficient. Conversely the HSE06 functional [46] which employs a screened short range Hartree-Fock exchange is a more sophisticated approach but more computationally intensive.

The minimum energies of diffusion were calculated using CI-NEB [65]. The migration energy corresponds to the barrier with the highest energy along the minimum energy path (MEP).

The formation energies of the defects are a function of the Fermi level, μ_e, and the chemical potentials, μ_α, of the corresponding atoms and are calculated according to the formula [61]:

$$E^f_{D,q}(\mu_e, \mu_\alpha) = E_{D,q} - E_H + \sum_\alpha n_\alpha \mu_\alpha + q(E_{\mathrm{VBM}} + \mu_e) + E_{\mathrm{pa}} \tag{5.2}$$

where $E^f_{D,q}$ is the total energy of the supercell containing the defect D in charge state q embedded in the Ge host and E_H is the total energy of the defect free Ge host. μ_α represents the chemical potentials of the number of different atoms added ($-n_\alpha$) or removed ($+n_\alpha$) when the defect is formed. μ_α is obtained as the energy per atom in its stable solid form. The Fermi level μ_e is referenced with respect to the VBM such as $0 \leq \mu_e \leq E_g$. Here E_g is the band gap and E_{VBM} is the valence band maximum. The introduction of a defect affects the band structure and gives rise to a shift in the electrostatic potentials between the perfect Ge host and the supercell containing the defect. This shift is corrected by using a potential alignment correction method [126] $E_{\mathrm{pa}} = q\Delta V_{\mathrm{pa}}$, where ΔV_{pa} is the average electrostatic potential difference between the defect supercell and the Ge host.

Defect levels or charge state transitions are defined as the point along the Fermi level where two defects with charges q and q' have the same formation energy:

$$\epsilon(q/q') = \frac{E^f(D,q) - E^f(D,q')}{q' - q} \tag{5.3}$$

where $E^f(D,q)$ and $E^f(D,q')$ are the defect formation energy with charges q and q' and electron chemical potential $\mu_e = 0$, respectively.

5.3. Diffusion of E-Centres in Ge

5.3.1. V_{Ge} Formation Energy

Theoretical studies of the vacancies in Ge have shown the possibility of the existence of different charged states whose lattice relaxations are charge dependent [127, 128]. The atoms around the vacancy relax inward, the extent of this relaxation increases with the charge state of the vacancy. This allows the surrounding atoms to reduce the energy of the system by forming extended bonds between them.

Using perturbed angular correlation spectroscopy (PACS), which employs probe atoms to trap vacancies and by studying their Coulomb and elastic interactions with the vacancies it was found the acceptor level $\varepsilon(0/-) = E_v + 0.20 \pm 0.04$ eV [129]. Another study [130] using deep level transient spectroscopy (DLTS) gave an acceptor level $\varepsilon(0/-) = E_v + 0.14$ eV.

Fig. 5.3 represents the formation energies of V_{Ge} for various charge states. The doubly negatively charged vacancy, V_{Ge}^{-2}, is dominant for intrinsic and n-type doping conditions. This prediction is supported by previous experiments on the impact of n-type doping on self-diffusion in Ge. According to the present calculations, neutral vacancies are expected to mediate self-diffusion in Ge under p-type doping. Such behaviour was recently observed in the experimental work of Südkamp *et al.* [131].

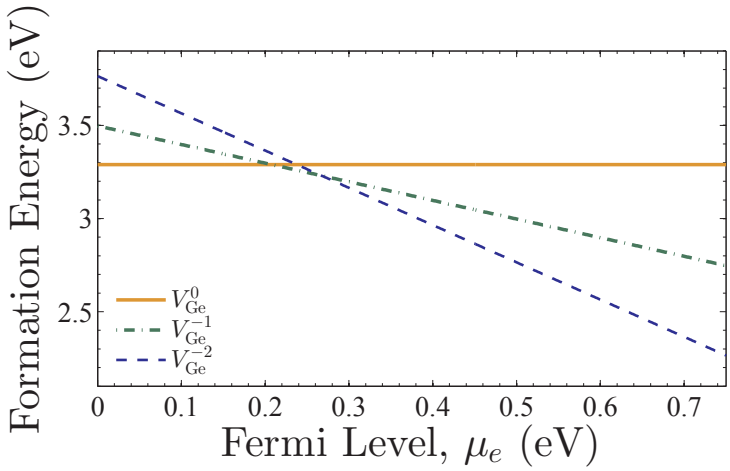

Figure 5.3.: The formation energies of vacancies in Ge.

Table 5.1.: The calculated stable charge transition energies for the E-centres and V_{Ge} (eV) for neutral (0), singly positive (+), singly negative (−) and doubly negative (=) charge states.

	$\mathrm{PV}_{\mathrm{Ge}}^{q}$	$\mathrm{AsV}_{\mathrm{Ge}}^{q}$	$\mathrm{SbV}_{\mathrm{Ge}}^{q}$	V_{Ge}
$\epsilon(+/0)$	···	···	0.02	···
$\epsilon(0/-)$	0.28	0.26	0.17	0.21
$\epsilon(-/=)$	0.52	0.47	0.19	0.27

The formation energy of a charge neutral V_{Ge} is calculated to be 3.30 eV. This is at variance with the value calculated by Śpiewak *et al.* [132] which was reported to be 2.33 eV using LDA+U. However, the agreement is more clear when using hybrid functional such as HSE06 such as the work by Weber *et al.* [133] who calculated the formation energy of V_{Ge} to be 3.01 eV.

V_{Ge}^{0} exists under p-doping conditions until a transition to V_{Ge}^{-1} takes place at $\mu_e = 0.21$ eV. V_{Ge}^{-1} will only be stable for a narrow range of Fermi levels before a second transition to V_{Ge}^{-2} occurs at $\mu_e = 0.27$ eV. This suggests that V_{Ge}^{-1} are never present in high concentrations in Ge samples, a fact that was enhanced by previous theoretical work by Jones *et al.* [134] and by the experimental work of Südkamp *et al.* [131] who observed that V_{Ge}^{-1} is not expected to control self-

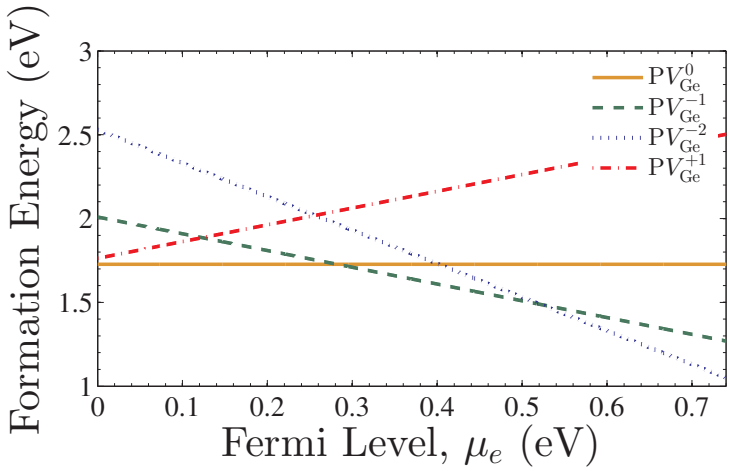

Figure 5.4.: The formation energies of PV^q pairs in Ge for various charge states as a function of the Fermi level.

diffusion under any doping conditions.

5.3.2. Formation Energies of PV_{Ge}^{q} Defects

Under p-doping conditions it is predicted that PV_{Ge}^{q} pairs favour the neutral charge state, which has a formation energy of 1.73 eV. This is much lower than the formation energy of V_{Ge}^{0}. The charge transition level $\epsilon(0/-)$ occurs at $E_v + 0.28$ eV, so the PV_{Ge}^{-1} cluster dominates in the intrinsic regime and up to light n-doping levels.

Upon capturing a second electron at $\mu_e = 0.52$ eV, PV_{Ge}^{-2} becomes the low energy specie and dominates up to the CBM.

5.3.3. Formation Energies of AsV_{Ge}^{q} Defects

Similar to PV_{Ge}^{q} pairs, AsV_{Ge}^{q} forms in the neutral, singly and doubly negatively charged states. AsV_{Ge}^{0} has a formation energy of 1.62 eV which is marginally lower than the formation energy of PV_{Ge}^{0}.

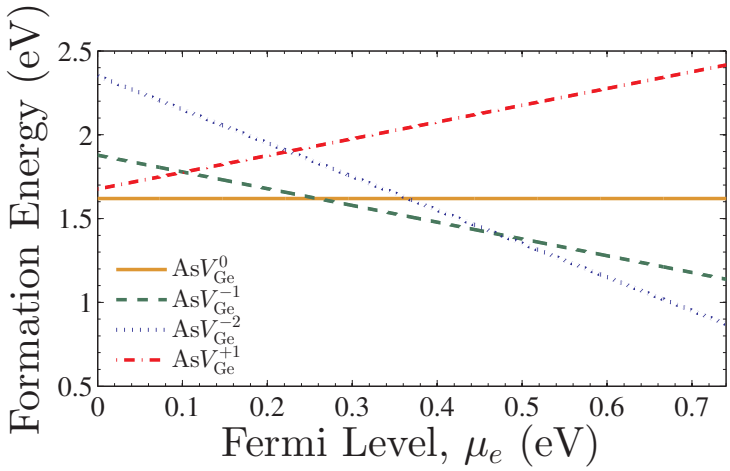

Figure 5.5.: The formation energies of AsV^q pairs in Ge for various charge states as a function of the Fermi level.

A transition to As$V_{\rm Ge}^{-1}$ occurs at $\mu_e = 0.26$ eV before a second transition at $\mu_e = 0.47$ eV occurs, implying that As$V_{\rm Ge}^{-1}$ is stable under intrinsic and near intrinsic doping conditions.

5.3.4. Formation Energies of Sb$V_{\rm Ge}^{q}$ Defects

The formation energies of Sb$V_{\rm Ge}^{q}$ pairs are lower than those of P$V_{\rm Ge}^{q}$ or As$V_{\rm Ge}^{q}$ indicating a possible relation between the dopants' size and electronegativities and their ease of formation. Sb$V_{\rm Ge}^{q}$ are at variance with the two pairs mentioned above in that Sb$V_{\rm Ge}^{+1}$ could form at or near the VBM before making a transition to Sb$V_{\rm Ge}^{0}$ at $\mu_e = 0.02$ eV creating a shallow acceptor state.

Sb$V_{\rm Ge}^{-1}$ are predicted to exist only for a narrow range in the band gap before Sb$V_{\rm Ge}^{-2}$ pairs form and dominate for a wide range of the band gap extending from $\mu_e = 0.18$ eV to the CBM.

According to the calculations, the E-centres are more likely doubly negative than singly negatively charged under n-type doping. This, in particular, should hold

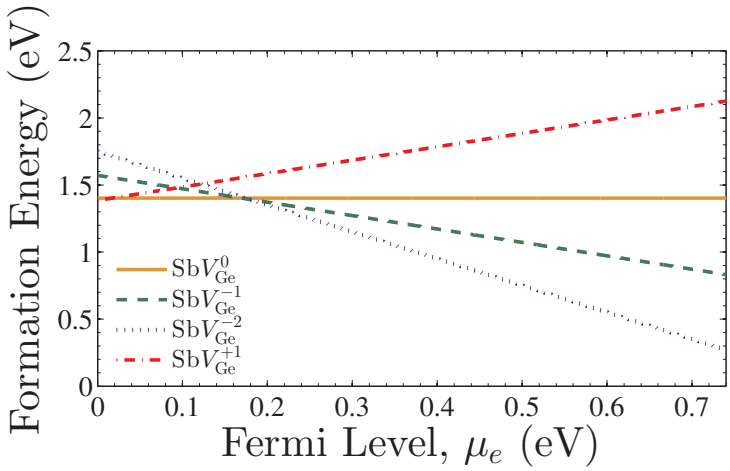

Figure 5.6.: The formation energies of SbV^q pairs in Ge for various charge states as a function of the Fermi level.

for SbV pairs even under intrinsic conditions, but is at variance with previous experiments that reveal the dominance of singly negatively charged E-centres [2]. Of course, the calculations are representative for 0 K while experiments are carried out at high temperatures (873 K∼1193 K [2]). Thus a direct comparison is always difficult without any information about the impact of temperature on the level position. This would imply that entropy effects should also be considered.

Table 5.1 summarizes the charge transition levels determined for the vacancy and the E-centres.

Having presented the formation of the neutral and negatively charged E-centres their binding energies, migration energies and activation energies of diffusion are then calculated.

The binding energy is a measure of the attraction of the defect cluster and is defined by the total energy of the cluster minus the energy of the isolated defect components. With this definition a negative binding energy corresponds to a stable defect cluster. Two distinct geometries were considered: (a) the formal

Table 5.2.: The binding (for the formal ΔE^1_{DV} and split-V $\Delta E^1_{D-\mathrm{split}-V}$ configurations.

	ΔE^1_{DV}		$\Delta E^1_{D-\mathrm{split}-V}$	
	$(-)$	(0)	$(-)$	(0)
PV_{Ge}	-0.54	-1.57	0.38	-0.47
AsV_{Ge}	-0.74	-1.68	-0.30	-1.08
SbV_{Ge}	-0.81	-1.89	-0.93	-2.01

vacancy-substitutional donor atom configuration and (b) the split$-V$ configuration where the donor atom is positioned in between two semi-vacancies. In Table 5.2 the calculated (GGA+U) binding energies are reported for the formal, ΔE^1_{DV}, and split$-V$, $\Delta E^1_{D-\mathrm{split}-V}$ configurations of E-centres in neutral and charged states. Only for the largest donor atom (i.e. Sb) is the split$-V$ configuration energetically favourable over the formal vacancy configuration (Table 5.2), consistent with the DFT study of Höhler *et al.* [135]. When the donor atom is separated at the next nearest neighbour site to the V, or beyond, the binding energies were calculated to be smaller in magnitude.

5.3.5. Migration Energies

E-centres migrate in the Ge lattice via the so-called ring mechanism of diffusion [136]. In this, the V_{Ge} moves around the donor atom and approaches it from a different direction. For the displacement of a donor the V_{Ge} must move away to at least the third-nearest neighbour site and return along a different path. As it exchanges position, the donor atom effectively progresses in the lattice by one site.

Figs. 5.7 and 5.8 represents the relative energies along the ring for the neutral and negatively charged E-centres respectively. In such calculations, several NEB simulations are performed which are then combined and connected to produce the profiles shown in Figs. 5.7 and 5.8 and similar figures in the next chapters.

Table 5.3.: The migration energies of DV_{Ge} pairs.

	$H^m_{DV_{\mathrm{Ge}}}$	
	$(-)$	(0)
$\mathrm{P}V_{\mathrm{Ge}}$	0.91	1.08
$\mathrm{As}V_{\mathrm{Ge}}$	0.99	0.95
$\mathrm{Sb}V_{\mathrm{Ge}}$	1.17	1.14

The migration energy barriers H^m_{DV} are defined as the largest relative energy barriers along the ring (Table 5.7). The activation enthalpy of diffusion, Q_a, is calculated by using the following definition [122]:

$$Q_a = H^f_V + \Delta E^1_{DV} + H^m_{DV} \tag{5.4}$$

where H^f_V is the formation enthalpy of an isolated V_{Ge}.

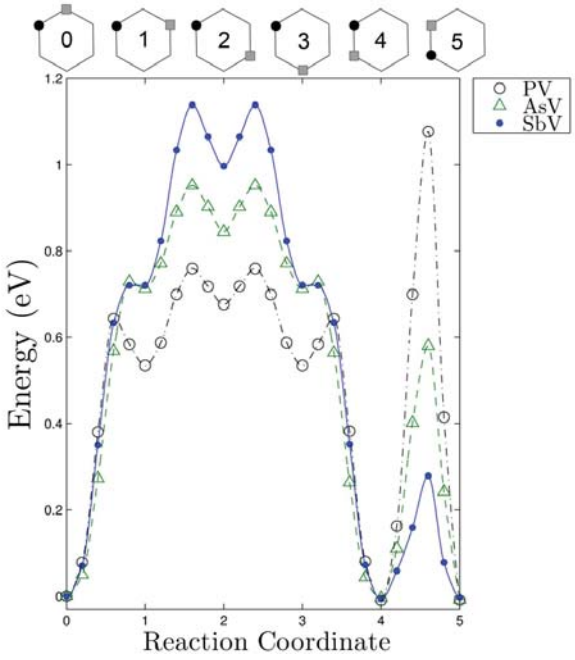

Figure 5.7.: Migration barriers for the diffusion path of the E-centres in the neutral charge state using the NEB technique.

Table 5.4 compares the calculated activation enthalpies of diffusion, using Eq. 5.4

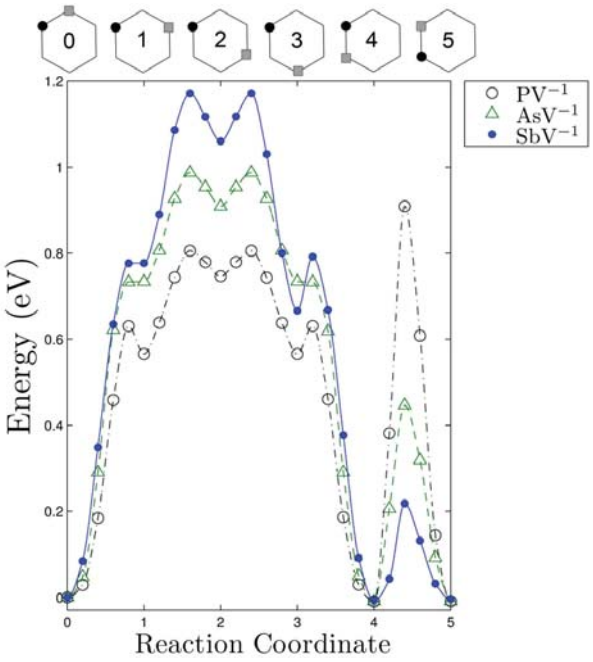

Figure 5.8.: Migration barriers for the diffusion path of the E-centres in the singly negatively charge state using the NEB technique.

Table 5.4.: The activation enthalpies (Q_a) for the E-centres (in eV) in their neutral and negative charge states. These are compared to experimental Q_a from SIMS analyses [2].

	Q_a		
	(-1)	(0)	Exp
PV_{Ge}	2.79	2.80	2.85
AsV_{Ge}	2.67	2.56	2.71
SbV_{Ge}	2.66	2.42	2.55

with previous experimental results from SIMS analyses of impurity diffusion profiles [2]. The calculated results for the singly negative charged E-centres are in good agreement with the experimental values (i.e. within 0.15 eV) [2]. Importantly both theoretical results and experiment are consistent with the trend that the activation energy for diffusion decreases with increasing donor atom size [2, 122], although for the (AsV_{Ge})$^{-1}$ and (SbV_{Ge})$^{-1}$ the differences are very small. Interestingly, the calculated activation energies for diffusion of AsV_{Ge} and

SbV_{Ge} are lower than the (AsV_{Ge})$^{-1}$ and (SbV_{Ge})$^{-1}$ indicating that they could diffuse faster. Nevertheless, under n-type conditions the V_{Ge}^{-2} defect should be dominant and the formation of (DV_{Ge})$^{-1}$, via Eq. 5.1, will prevail.

5.4. Diffusion of Tin in Ge

Previous investigations demonstrated that the mobilities of holes and electrons can be increased by the introduction of strain [137]. Recent studies propose the fabrication of strained-Ge (sGe) complementary metal-oxide-semiconductor (CMOS) with germanium-tin ($Ge_{1-x}Sn_x$) alloys as stressors [138, 139]. Studies on $Ge_{1-x}Sn_x$ alloys are also motivated by their advantageous optical properties; however, there are still issues that need to be addressed [87, 140]. SnV interactions and their diffusion properties have been previously investigated using DFT but only for neutral defects and defect clusters [87, 122, 140]. As it is possible for Sn atoms to diffuse from the $Ge_{1-x}Sn_x$ alloy into doped-Ge layers, an understanding of Sn-diffusion in both n-type and p-type Ge is important.

As was mentioned in the sections above, vacancies are the dominant intrinsic defect species in Ge, with previous work establishing their interaction with impurity atoms (D) to form DV_{Ge} pairs and larger clusters [2, 141, 142]. As with other dopants (P, As, Sb, etc), the diffusion of Sn in Ge is mainly mediated by vacancies [2, 141, 142]. The Sn atoms occupy substitutional lattice positions. This was confirmed by DFT simulations and experimental work by Weyer *et al*. [143] who employed Mössbauer spectroscopy and Rutherford backscattering spectrometry in a channelling geometry.

The structure of these SnV_{Ge} pairs is more complicated but can be reasonably described by two geometries: (a) the formal vacancy-substitutional Sn atom configuration and (b) the split$-V_{\mathrm{Ge}}$ configuration [135, 144, 145]. In the latter the Sn atom is positioned in between two semi-vacancies [135, 144, 145]. For all

the SnV_{Ge} pairs it was calculated that the split$-V_{\mathrm{Ge}}$ configuration is energetically favourable.

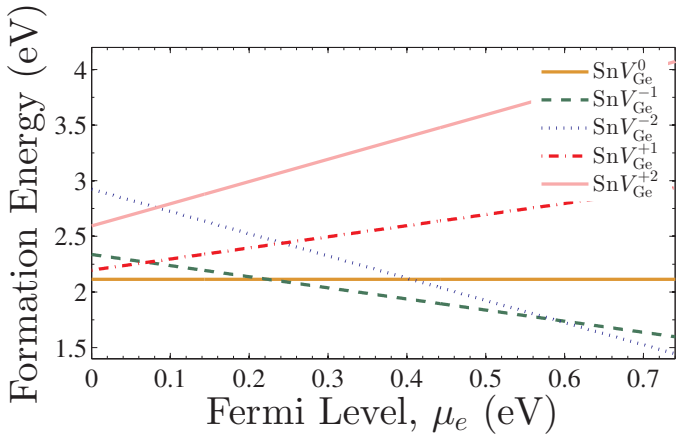

Figure 5.9.: The formation energies of the SnV_{Ge} pairs, as a function of the Fermi level.

It is important to identify the charge states of the SnV_{Ge} pairs for different doping conditions. Fig. 5.9 presents the formation energies of the SnV_{Ge} pairs, with respect to the Fermi level, for various charge states. From Fig. 5.9 it is deduced that the SnV_{Ge} pairs are charge neutral up to a Fermi level of 0.22 eV, above which the singly negatively charged state becomes dominant. Finally, at a Fermi level of 0.55 eV the doubly negatively charged pairs are most stable. Positive charge states of this cluster are always significantly less stable.

Having established the dominant charge states of the SnV_{Ge} pairs their diffusion behaviour merits investigation. Similar to the dopant-vacancy pairs presented above, SnV_{Ge} pairs will diffuse via the ring mechanism [136]. Fig. 5.10 presents the relative energies along the ring for neutral and singly and doubly negatively charged SnV_{Ge} pairs. From this figure the migration energy barrier, $H^m_{\mathrm{Sn}V}$, is defined as the largest relative energy barrier along the ring. The activation enthalpy of diffusion, Q_a, is calculated by using Eq. 5.4 as defined above.

Doping changes the concentration of free charge carriers in a material. For ex-

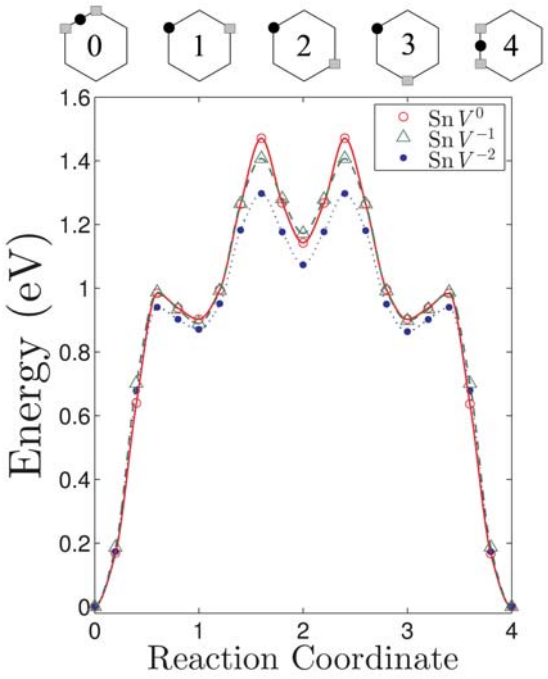

Figure 5.10.: Diffusion path of the SnV_{Ge}. On the top of the figure is the ring mechanism of diffusion for the SnV_{Ge} pair projected onto the (111) surface of Ge.

ample, n-type doping will increase the concentration of electrons in the system, causing the Fermi level, located close to the middle of the band gap in an intrinsic material, to shift to higher energies or to shift to lower ones in the case of p-type doping. The formation energies of charged defects such as vacancies depend upon the position of the Fermi level, where different charged states dominate at different values of the Fermi level. This dependence should also be reflected in the diffusion activation energies which depend upon the formation energies of the vacancies. It therefore becomes necessary to study the activation energy as a function of the Fermi level. Previous studies, for example those by Bernholc *et al.* [146] or Branz *et al.* [147] found a strong relation between Q_a and μ_e. One such study, which investigated the diffusion of hydrogen in poly-silicon, found that the activation energy might vary between 0.1 and 1.69 eV [148].

The studies of Vogel *et al.* [149] and Werner *et al.* [150] have revealed that

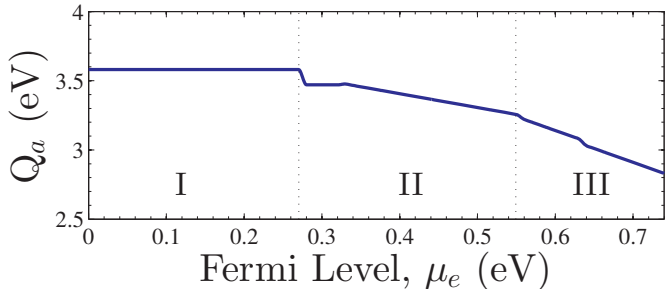

Figure 5.11.: The activation energy's dependence on the Fermi level.

n-type doping enhances self-diffusion in Ge whereas p-type doping retards it. To investigate the dependence of the activation energy on the doping levels, three regions within the band gap were studied. Region I lies between 0 and 0.22 eV. Here the binding and migration energies of a neutral SnV_{Ge} pairs are used in Eq. 5.4. The vacancy formation energy as a function of the Fermi level is taken from a previous study [117]. Region II extends from 0.22 to 0.55 eV, where the singly negatively charged SnV_{Ge} pair prevails. Here the binding and migration energies of a singly negatively SnV_{Ge} pair were used along with the vacancies formation energies in that region of the Fermi level. Finally, in region III, which extends from 0.55 eV to the edge of the conduction band minimum, the values of the binding and migration energies of a doubly negatively charged SnV_{Ge} pair were used.

This significant variation in the activation energy with respect to the Fermi level can explain the many differing experimental results previously obtained. Overall the range of the calculated activation energies is consistent with the experimentally determined values [151–153]. SIMS studies gave a value of 3.26 eV for the activation energy while two radiotracer studies gave 2.90 eV [153] and 3.05 eV [154]. From Fig. 5.11 we can see that for the intrinsic case, when the Fermi level is close to the middle of the band gap (i.e. $E_{\mathrm{F}} \sim 0.37$ eV), we obtain a value of about 3.21 eV for the activation energy, which is in good agreement with the SIMS results [148]. Shifting the Fermi level below the middle of the band gap

(i.e. p-type doping the material) results in an increase in the activation energy. This trend is consistent with the results of Riihimäki *et al*. [153] who measured the activation energy of Sn diffusion in intrinsic Ge to be 2.90 eV and in p-type doped Ge to be 3.33 eV.

5.5. Summary

In summary, a GGA+U approach was used to calculate the binding energies, formation energies and activation enthalpies of diffusion for the technologically important n-type donor atoms in Ge. The SbV_{Ge} pair, in contrast to PV_{Ge} and AsV_{Ge}, is more bound in the split$-V_{\mathrm{Ge}}$ configuration. In good qualitative and quantitative agreement with the most recent and accurate experiments [2] we predict the underlying trend observed in the activation enthalpy of P, As and Sb diffusion: that is, with increasing donor size, Q_a decreases.

SnV_{Ge} pairs will form in their neutral (Fermi level up to 0.22 eV), singly negatively charged (Fermi level between 0.22 eV and 0.55 eV) and doubly negatively charged (Fermi level exceeding 0.55 eV) states. Positively charged states are not predicted to form. Depending upon the Fermi level, the activation energies for diffusion were calculated to be in the range 2.48-3.65 eV, in agreement with available experimental data.

Some of the work presented here appear in Tahini *et al.*
Phys. Chem. Chem. Phys. **15**, 367 (2013) [155].

6. Defect Engineering Strategies to Retard Phosphorous Diffusion in Germanium

6.1. Introduction

Forming p-type doped regions in germanium (Ge)-devices can be achieved by using boron (B) but n-type dopants such as phosphorous (P) diffuse quickly and consequently the formation of ultra-shallow junctions, with high active dopant concentrations, is a challenge [156–158]. It has previously been established that P diffuses via a vacancy (V_{Ge}) mechanism, which is the dominant intrinsic point defect in Ge [2, 117, 122]. It was determined by Brotzmann and Bracht [2] that P diffusion increases with the square of the free electron concentration. This strong doping dependence is explained by the formation

of negatively charged phosphorous-vacancy, $(\mathrm{P}V_{\mathrm{Ge}})^{-1}$, pairs via the reaction:

$$(\mathrm{P}V_{\mathrm{Ge}})^{-1} \leftrightarrow \mathrm{P_s}^{+1} + V_{\mathrm{Ge}}^{-2} \tag{6.1}$$

where P_s^{+1} denotes the singly positively charged P substitutional atom and V_{Ge}^{-2} the doubly negatively charged vacancy. The key to controlling n-type dopant diffusion in Ge is the annihilation or confinement of the vacancies, as they are the vehicles for diffusion [142, 159]. The diffusion of P in Ge can be affected not only by the intrinsic point defects but also by codopants. For example, in recent studies it has been verified that the introduction of small isovalent codopants such as carbon (C) can retard n-type dopant diffusion in Ge as C traps mobile $\mathrm{P}V_{\mathrm{Ge}}$ pairs thereby forming stable $\mathrm{CP}V_{\mathrm{Ge}}$ complexes [2, 120].

The introduction of larger isovalent codopants can affect dopant-defect interactions in group IV semiconductors [160–162]. The aim of the present contribution is to discover point defect engineering strategies based upon isovalent doping that will retard the V_{Ge}-mediated diffusion of P in Ge. In particular using DFT calculations the impact of Sn and Hf on the migration and binding energies of $(\mathrm{P}V_{\mathrm{Ge}})^{-1}$ pairs in Ge will be investigated.

6.2. Methodology

DFT as implemented in the VASP [101] was used to calculate the total energies of the defects and their migration energies in Ge. Calculation parameters with similar setting as those described in Chapter 5 are used here. All calculations were performed so as to account for the spin-polarization. The GGA+U approach used here has been discussed and employed in previous chapters. In order to verify this methodology, the HSE06 [43, 44] hybrid function is used, setting the fraction of the non-local Hartree-Fock potential to its default value of 25% and the screening parameter, μ, to 0.207 Å^{-1}. For HSE06, the same **k**-point

grid and the same energy and forces convergence criteria were used as above. This hybrid functional gives a fairly accurate description of the electronic structure of many solids [163] including Ge, for which a band gap of ~ 0.75 eV is reproduced (compared to the experimental value of 0.74 eV).

In this chapter we will investigate the migration energies and mechanisms of vacancies in bulk Ge, which has been codoped with P and Sn or Hf. This is achieved through studying the interactions of both the dopant atoms with the host lattice and with each other, by analysing their migration energies from one configuration to another and by considering the charge densities for selected geometries.

6.3. Results and Discussions

Substitutional Sn and Hf species next to a vacancy will relax to a split-vacancy configuration. In accordance with Eq. 6.1 the migration of vacancies was investigated as constitutive elements of the singly negatively charged clusters (PSnV_{Ge})$^{-1}$ and (PHfV_{Ge})$^{-1}$. Fig. 6.1 shows the migration barriers, associated with Sn, obtained as the vacancy hops from one site to another.

The migration energy, which corresponds to the step along the ring with the highest energy barrier, is 1.54 eV. This energy is comparable to the migration energy of a vacancy in the presence of Sn alone (i.e. 1.47 eV) as was presented the previous chapter (see Chapter 5). Hf, on the other hand, dramatically increases the migration energy to about 3.04 eV (see Fig. 6.2).

To understand the origin of the high migration energy, the binding energies for (PSnV_{Ge})$^{-1}$ and (PHfV_{Ge})$^{-1}$ clusters were calculated for all the configurations shown at the top of Figs. 6.1 and 6.2. The binding energy is a measure of the stability of the cluster with respect to its constituent components (i.e. P, Sn and

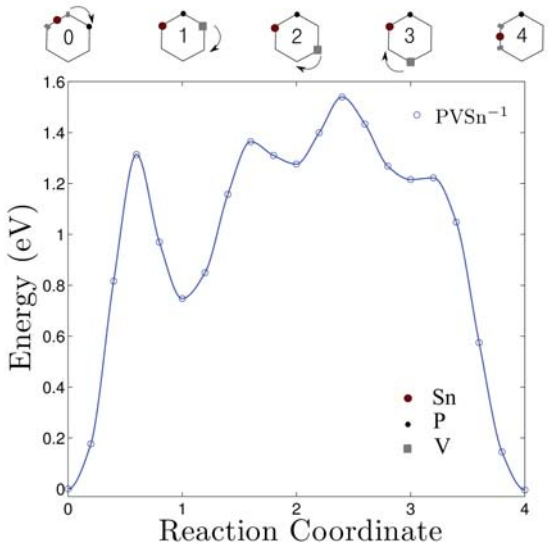

Figure 6.1.: Diffusion path of the PV_{Ge} pairs in the presence of Sn. On the top of the figures is the ring mechanism of diffusion for the PV_{Ge} pair in the presence of Sn, respectively, projected onto the (111) surface of Ge. In configurations 0 and 4 the Sn atoms are surrounded by two semi-vacant sites in what is known as the split-vacancy configuration.

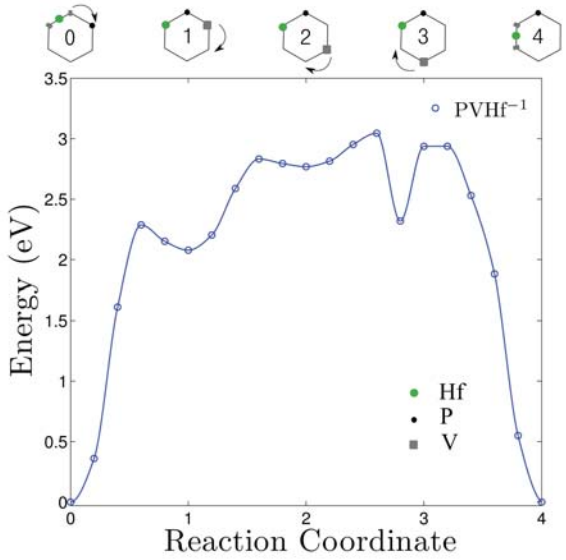

Figure 6.2.: Diffusion path of the PV_{Ge} pairs in the presence of Hf. On the top of the figures is the ring mechanism of diffusion for the PV_{Ge} pair in the presence of Hf, respectively, projected onto the (111) surface of Ge. In configurations 0 and 4 the Hf atoms are surrounded by two semi-vacant sites in what is known as the split-vacancy configuration.

V_{Ge}^{-2} or P, Hf and V_{Ge}^{-2}). For example, the binding energy of a substitutional P atom to a Hf atom and a V_{Ge} to form a PHfV_{Ge} cluster in Ge is given by:

$$\begin{aligned} E_b(\mathrm{PHf}V_{\mathrm{Ge}}\mathrm{Ge}_{N-3}) = E(\mathrm{PHf}V_{\mathrm{Ge}}\mathrm{Ge}_{N-3}) - E(\mathrm{PGe}_{N-1}) \\ - E(\mathrm{HfGe}_{N-1}) - E(V_{\mathrm{Ge}}\mathrm{Ge}_{N-1}) + 2E(\mathrm{Ge}_N) \end{aligned} \tag{6.2}$$

where $E(\mathrm{PHf}V_{\mathrm{Ge}}\mathrm{Ge}_{N-3})$ is the energy of a N lattice site supercell (here $N = 64$) containing $N-3$ Ge atoms, a P atom, one Hf atom and a V_{Ge}; $E(\mathrm{PGe}_{N-1})$ is the energy of a supercell containing one P atom and $N-1$ Ge atoms; $E(\mathrm{HfGe}_{N-1})$ is the energy of a supercell containing one Hf atom and $N-1$ Ge atoms; $E(V_{\mathrm{Ge}}\mathrm{Ge}_{N-1})$ is the energy of a supercell containing a V_{Ge} and $N-1$ Ge atoms; and $E(Ge_N)$ is the energy of the N Ge atom supercell. Therefore, here a negative binding energy corresponds to a defect cluster that is stable with respect to its constituent point defect components.

Table 6.1.: Calculated binding energies of the different configurations forming the (PSnV_{Ge})$^{-1}$ and (PHfV_{Ge})$^{-1}$ clusters calculated using GGA, GGA+U and HSE06.

	Binding Energy (eV)					
	(PSnV_{Ge})$^{-1}$			(PHfV_{Ge})$^{-1}$		
Configuration	GGA	GGA+U	HSE06	GGA	GGA+U	HSE06
0	−0.58	−1.49	−1.20	−2.33	−3.55	−3.51
1	−0.43	−0.75	−0.81	−1.06	−1.48	−1.52
2	−0.16	−0.22	−0.43	−0.76	−0.70	−0.95
3	−0.30	−0.28	−0.47	−0.80	−0.62	−0.91
4	−0.58	−1.49	−1.20	−2.33	−3.55	−3.51

The binding energies were calculated using GGA, GGA+U and the HSE06 functional as shown in Table 6.1. A comparison of these three modes of calculation reveals a good agreement between the GGA+U and HSE06.

Based on the good agreement between the GGA and HSE06 values values given

in Table 6.1, it is safe to assume that the GGA+U method (which is at least an order of magnitude computationally faster than HSE06) is valid for this type of study. To further validate this model, the densities of states (DOS) of bulk Ge and for supercells containing one Sn or Hf atom using GGA+U and HSE06 were calculated as shown in Figs. 6.3 and 6.4 respectively. For such calculations a denser $6 \times 6 \times 6$ **k**-point grid was used. It is evident that in both cases the defects do not introduce states into the band gap, which can be attributed to the isovalent nature of these defects. Furthermore, the energies and natures of the orbitals (*s*, *p* and *d*) are nearly identical with these two different functionals.

We therefore proceed in analysing the clusters formed using GGA+U. The values show that those configurations which involve Hf are more bound than the corresponding configurations that incorporate Sn. For the starting configuration when Sn or Hf occupies the split-vacancy configuration next to a P atom, the binding energies are -1.49 eV and -3.55 eV respectively. As the V_{Ge} exchanges position with the P atom the binding energies drop to -0.75 eV and -1.48 eV for the pairs containing Sn or Hf respectively, which are nearly half the equivalent original energies in each case.

The charge densities of these two particular configurations for the (PSnV_{Ge})$^{-1}$ and (PHfV_{Ge})$^{-1}$ clusters are shown in Figs. 6.5 and 6.6 respectively. As can be seen in the left panel of Fig. 6.5, when Sn occupies the split-V_{Ge} configuration (configuration 0) it tends not to share electrons with the P atom, which in turn draws additional electron density to its vicinity. This is to be expected because P has a high electronegativity, 2.19, compared to 1.96 for Sn and 2.01 for Ge. The right panel shows the charge distribution when V_{Ge} and P species exchange positions (configuration 1). Now P and Sn share electrons, which implies that they are bonded. Equivalently, in Fig. 6.6 the two configurations for Hf are shown, but it is clear that Hf still forms a bond even when it is in the split-V_{Ge} configuration.

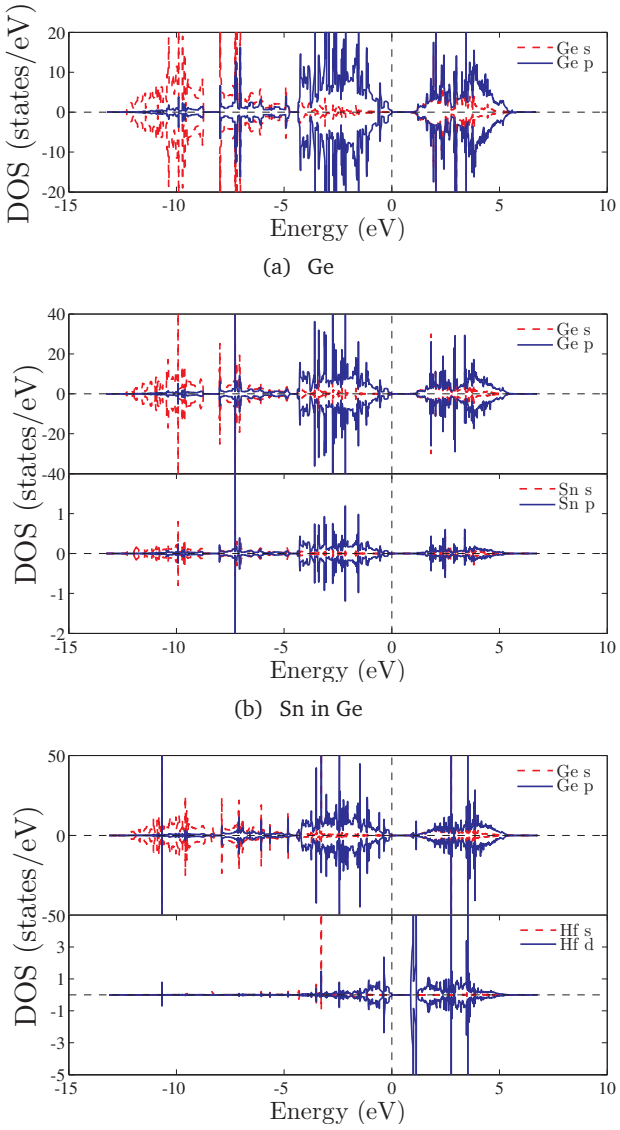

(a) Ge

(b) Sn in Ge

(c) Hf in Ge

Figure 6.3.: Partial densities of states of (a) perfect Ge, (b) one Sn atom in Ge and (c) one Hf atom in Ge calculated using GGA+U.

At first, configuration 1 might appear to be more bound as the Sn/Hf atoms form bonds with the P atom, but as the calculations show, the binding energies of configuration 0 are nearly twice those of configuration 1 for both Sn and

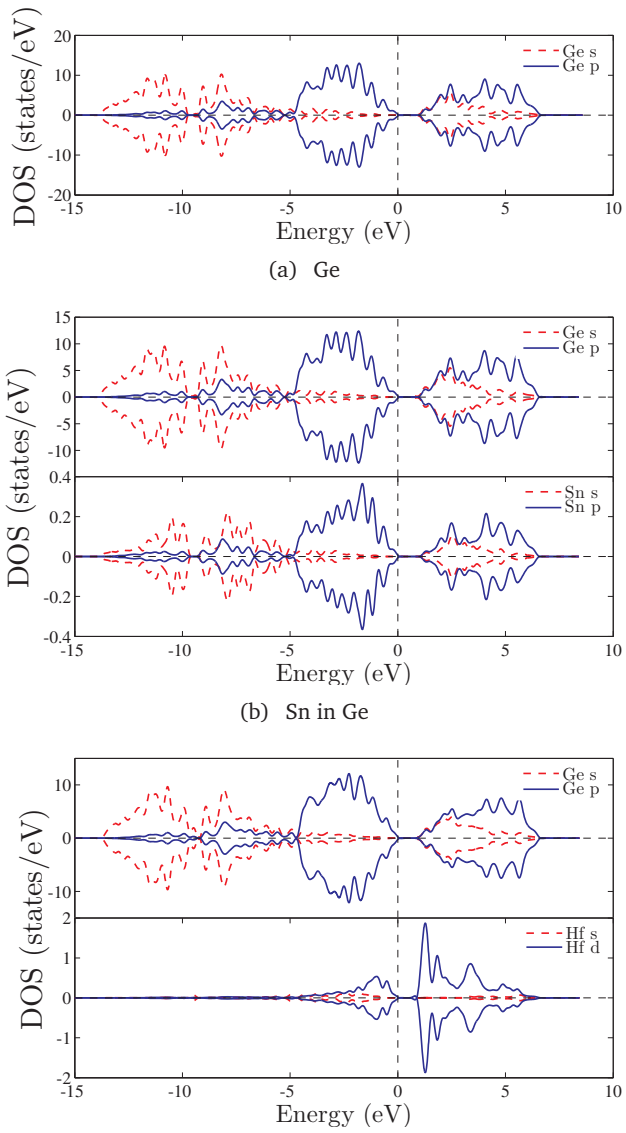

(a) Ge

(b) Sn in Ge

(c) Hf in Ge

Figure 6.4.: Partial densities of states of (a) perfect Ge, (b) one Sn atom in Ge and (c) one Hf atom in Ge calculated using HSE06 functional.

Hf.

To better understand this, the neighbours of each species forming these clusters

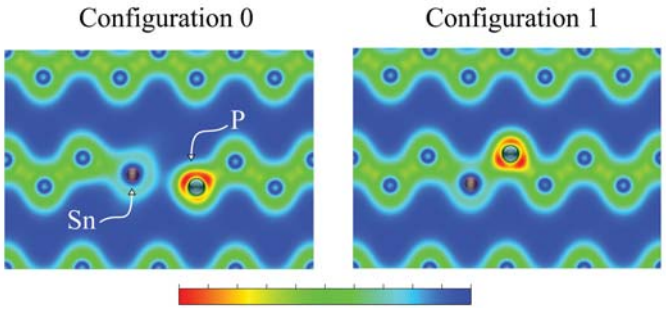

Figure 6.5.: The charge density plots of configuration 0 (left) which shows the Sn atom in the split-V_{Ge} configuration and configuration 1 for (PSnV_{Ge})$^{-1}$.

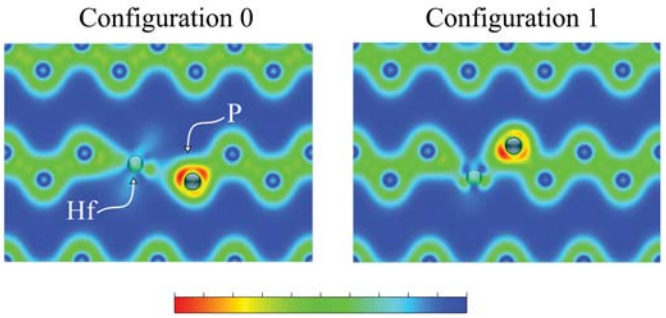

Figure 6.6.: The charge density plots of configuration 0 (left) which shows the Sn atom in the split-V_{Ge} configuration and configuration 1 for (PHfV_{Ge})$^{-1}$.

were analysed and their bond lengths compared. The bond lengths of the nearest neighbours (NN) to P are always shorter than those formed between Sn/Hf and their neighbouring Ge atoms. The left panel of Fig. 6.7 shows there are two NN Ge atoms with an average P-Ge bond length equal to 2.38 Å, whereas the five Ge atoms form Sn-Ge bonds with lengths varying between 2.69 Å to 2.95 Å. For configuration 1 the P atom is only surrounded by 2 NN Ge atoms with bond lengths of about 2.37 Å and the Sn atom forms bonds of length 2.59 Å with 3 Ge atoms. This explains the much greater binding energy of configuration 0 compared to configuration 1 even when the P and Sn atoms do not share electrons (see Fig. 6.5).

Similar atomic arrangements are exhibited by the (PHfV_{Ge})$^{-1}$ cluster (see Fig. 6.8),

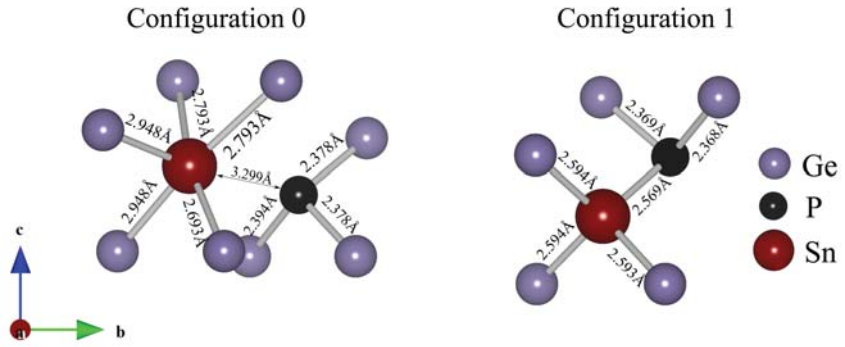

Figure 6.7.: The nearest neighbours surrounding the P and Sn atoms in a $(\mathrm{PSn}V_{\mathrm{Ge}})^{-1}$. The number of nearest neighbours and their bond lengths determines the stability of the cluster.

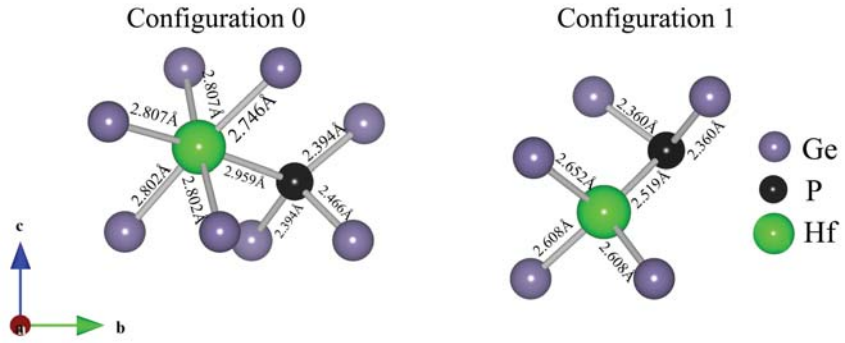

Figure 6.8.: The local environment showing the nearest neighbours species surrounding the P and Hf atoms in a $(\mathrm{PHf}V)^{-1}$.

however, the P and Hf species come close enough to form a bond, which is about 2.96 Å long, resulting in a much higher binding energy compared to the $(\mathrm{PSn}V_{\mathrm{Ge}})^{-1}$ cluster. In order to verify the role that Sn or Hf play in retarding the diffusion of P, the binding energies of $\mathrm{Sn}V_{\mathrm{Ge}}$ and $\mathrm{Hf}V_{\mathrm{Ge}}$ clusters were calculated. These were found to be -1.09 eV and -2.70 eV respectively as compared to the binding energy of the $(\mathrm{P}V_{\mathrm{Ge}})^{-1}$ cluster, which is -0.54 eV. These high binding energies, in particular for Hf, mean that as the vacancy migrates across the lattice and encounters an oversized atom, it is trapped, reducing the mobility of these mediating species, even before they become part of the larger clusters.

6.4. Conclusions

In summary, a GGA+U approach was used to investigate the impact of oversized isolated co-dopants on the migration of P in Ge. Codoping with Hf and to some extent with Sn was predicted to significantly increases the migration energy barriers of P via a V_{Ge}-mediated mechanism. In particular, we find that strongly bound (PSnV_{Ge})$^{-1}$ and (PHfV_{Ge})$^{-1}$ clusters form, which trap the migrating (PV_{Ge})$^{-1}$ pair. Thus, the introduction of oversized isovalent codopants is proposed as a possible point defect engineering strategy to limit P migration in Ge. However, more work is needed to assess the damage caused by implantation of Ge which could lead to high concentrations of vacancies and interstitials that could participate in more complex defect reactions. Also the properties of the residual PSn and PHf complexes need to be fully addressed to further support the validity of this engineering approach.

Aspects of this chapter have been published in Tahini *et al.* J. Appl. Phys. **113**, 073704, (2013) [164].

7. Codopoing with Antimony to Control Phosphorous Diffusion in Germanium

7.1. Introduction

Germanium is emerging as an important material for nanoelectronic devices, not only due to its superior properties (lower dopant activation temperatures, smaller band gap and high carrier mobilities) but also because it has the highest dielectric constant (high-κ) of the group IV semiconductors [156, 157, 160]. Although Si and Ge are isostructural, the vacancy is the dominant intrinsic point defect only in Ge [2]. Vacancies can have a deleterious impact on the fabrication of high performance Ge-metal-oxide-semiconductor field-effect transistor (MOSFETs) or other Ge based devices [142]. In particular in the

channel region of the device vacancies provide scattering centres degrading the carrier mobility; in the source and drain junctions they act as recombination sites increasing the leakage current. Finally in the n-type regions vacancies can enhance donor atom diffusion or cause the deactivation of donor atoms via cluster formation [2, 142]. It is important to constrain or reduce the concentration of vacancies in Ge as they are the vehicle mediating donor atom diffusion and also an important constituent of the clusters related to deactivation (for example $As_n(V_{Ge})_m$ or $Sb_n(V_{Ge})_m$ clusters) [144, 165]. To control vacancies a number of point defect engineering strategies have been proposed [2, 122, 142, 158, 166]. A DFT study on P and As co-doping proposed that double-donor doping can be an effective way to engineer the active donor concentrations [167]. That study inspired the experimental investigation of Tsouroutas *et al*. [166] on P and As co-doping. Tsouroutas *et al*. [166], however, concluded that although there is a retardation of As diffusion the activation level of co-doped Ge is lower than that of single-doped Ge. Recently Kim *et al*. [158] used P and Sb co-doping to improve Ge n+/p junction diode characteristics. They concluded that P and Sb co-doping has a beneficial impact upon the n-type dopant activation leading to an increased forward biased current density in shallow junction diodes. Kim *et al*. [158] hypothesise that the mechanism for the enhanced activation in P and Sb co-doped Ge might be linked to local strain compensation (P is smaller than Ge, whereas Sb is larger). The aim of the present study is to quantify the binding of P and Sb to vacancies and the impact of co-doping on the migration energy of these donor atoms in Ge.

7.2. Methodology

DFT implemented numerically in VASP was used to calculate the defect energetics (binding energies, migration energies) [101]. A $2 \times 2 \times 2$ Monkhorst-Pack mesh was used to sample the Brillouin zone [38]. Energy and force convergence

criteria and pseudopotentials similar to the ones used in previous chapters are used here. All simulations were carried out at constant volume using the calculated perfect lattice parameter of Ge (5.5985 Å) in a 216 atom supercell. Electron spin-polarisation was accounted for in the simulations. DFT calculations using semi-local exchange-correlation functionals underestimate the band gap of Ge. In order to correct for this a GGA+U approach was used as implemented previously, which was positively compared to the performance of the HSE06 hybrid functional [43, 155, 163]. Charged defect clusters were created by adding or removing electrons from the simulation supercell. The 216 atoms supercell was chosen to minimise the effect of the charged defect-defect interactions. In addition, NEB results are taken as the differences between successive images leading to the cancellation of spurious interactions.

7.3. Results

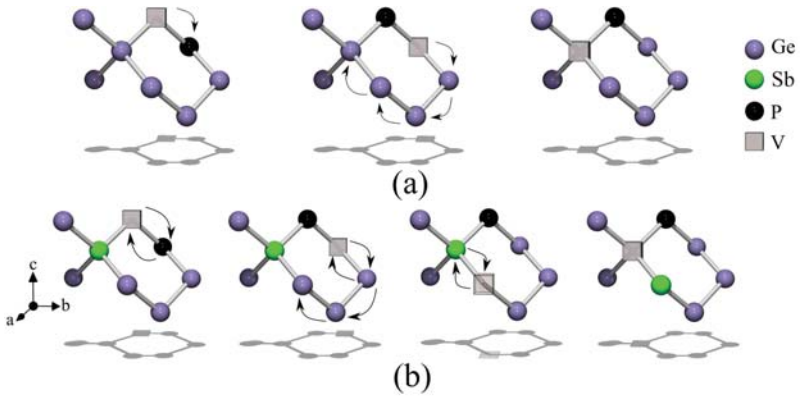

Figure 7.1.: Schematic of the ring mechanism of diffusion.

We first investigate the migration energy of the single negatively charged pair $(PV_{Ge})^{-1}$. It has been previously established that the V-mediated diffusion of dopants in Ge proceeds via the ring mechanism of diffusion [2]. Fig. 7.1(a) shows the ring diffusion mechanism for the $(PV_{Ge})^{-1}$ cluster and Fig. 7.2 the

energies associated with each step.

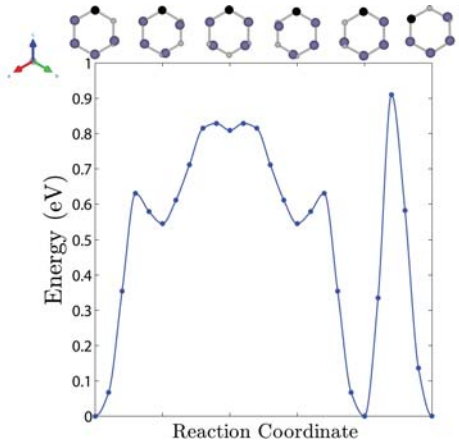

Figure 7.2.: Diffusion path of PV_{Ge}^{-1} pairs.

The migration energy barrier (i.e. the step along the ring with the highest energy barrier in Fig. 7.2) for the single negatively charged pair $(PV_{Ge})^{-1}$ is 0.91 eV. For completeness the migration energy barrier of the $(SbV_{Ge})^{-1}$ pair was also calculated (1.17 eV).

To consider the trapping of the $(PV_{Ge})^{-1}$ pair to further donor atoms (P or Sb) the following reactions were considered:

$$\begin{aligned} (PV_{Ge})^{-1} + P_s^{+1} &\leftrightarrow P_2V_{Ge} \\ (PV_{Ge})^{-1} + Sb_s^{+1} &\leftrightarrow PSbV_{Ge} \end{aligned} \tag{7.1}$$

The formation of these neutral clusters is promoted by the attraction of the oppositely charged components. The $PSbV_{Ge}$ cluster is more bound compared to the P_2V_{Ge} cluster (-2.03 eV and -1.83 eV respectively) because the oversized Sb atom benefits more from the relaxation near the vacant space of the $(PV_{Ge})^{-1}$ pair. This is also indicated by the binding energies of the $(SbV_{Ge})^{-1}$ and $(PV_{Ge})^{-1}$ pairs, which are -1.19 eV and -0.93 eV respectively. Interestingly, for the $(SbV_{Ge})^{-1}$ pair, the oversized Sb atom occupies the space between two

semi-vacant lattice sites, leading to a configuration known as the split-vacancy configuration [135]. The present study reproduces this configuration in agreement with the previous DFT study of Höhler *et al.* [135]. Importantly, the difference in binding energies, in favour of the Sb atom, reveal that it will have a greater *radius of influence* to attract migrating $(PV_{Ge})^{-1}$ pairs as compared to P atoms.

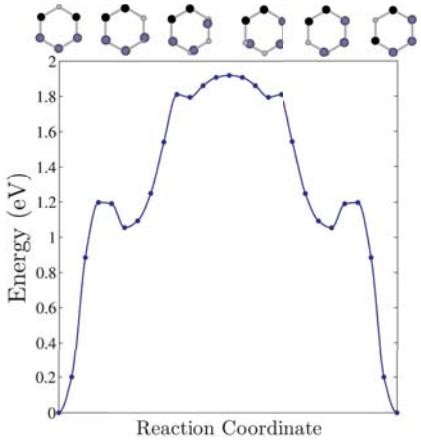

Figure 7.3.: Diffusion path of PV_{Ge} pairs in the presence of a second P atom.

The next issue that needs to be considered is the mobility of the P_2V_{Ge} and $PSbV_{Ge}$ clusters. Figs. 7.3 and 7.4 show the energies of the diffusion paths for the P_2V_{Ge} and $PSbV_{Ge}$ clusters along the ring mechanism (Fig. 7.1(b)). The P_2V_{Ge} and $PSbV_{Ge}$ clusters have migration energy barriers 1.92 eV and 1.94 eV respectively, indicating that there is practically no difference. Both these migration energy barriers are higher by more than 1 eV compared to the $(PV_{Ge})^{-1}$ pair and therefore the association of the pair with a further donor atom via Eq. 7.1 will lead to it being less mobile. For the P_2V_{Ge} pair, this was previously established by the study of Brotzmann *et al*. [168]; however, for mixed clusters there has been no such information.

As mentioned earlier, Kim *et al*. [158] hypothesised that the mechanism for enhanced activation in P and Sb co-doped Ge is linked to local strain compensation. The present study quantifies that mixed clusters such as $PSbV_{Ge}$ are more bound

than P_2V_{Ge} (by -0.2 eV); however, we also find that such larger clusters (P_2V_{Ge} and/or PSbV_{Ge}) will be less mobile compared to the $(PV_{Ge})^{-1}$ pair.

Next we consider how these binding and migration energies compare with P co-doped with an isovalent dopant. In a recent DFT study it was shown that the binding energy of the $(PHfV_{Ge})^{-1}$ cluster is -3.55 eV and therefore more energetically favourable compared to the PSbV_{Ge} cluster by about 1.5 eV [168]. This in turn implies that Hf will be more effective than Sb in trapping the $(PV_{Ge})^{-1}$ pair. However, the singly positivly charged Sb atom can have an advantage in attracting the negatively charged $(PV_{Ge})^{-1}$ pair via a Coulombic interaction (and as such it is expected to have a larger radius of influence).

At this point, one needs to consider whether the $(PHfV_{Ge})^{-1}$ or the PSbV_{Ge} clusters would be more efficient precursors for the formation of the larger P-vacancy clusters that could lead to the deactivation of a significant part of the P dose. Considering that the $(PHfV_{Ge})^{-1}$ clusters are singly negatively charged it is unlikely that they will attract the migrating $(PV_{Ge})^{-1}$ pairs or the doubly negatively charged vacancies. They are also practically immobile as they have high migration energies. Conversely, the P_2V_{Ge} and PSbV_{Ge} clusters are neutral and thus larger clusters may still be formed as predicted via DFT/mass action analysis approaches (see Chroneos *et al*. [144]). The formation of these clusters is also supported by experimental work in n-type doped Si [169–171] and Ge (Bruno *et al*. [165]).

The recent study of Schneider and Bracht [172] highlighted that a supersaturation of Ge interstitials can suppress the formation of dopant-vacancy clusters. This approach is thus advantageous to maximise the activation level of donor atoms in implanted Ge [172]. The difference between P-doped Ge and Ge co-doped with P and Sb may in part be reconciled by the differences in the defect structure established under implantation and the subsequent rapid thermal annealing. The impact of Ge interstitial in these processes needs to be detailed in

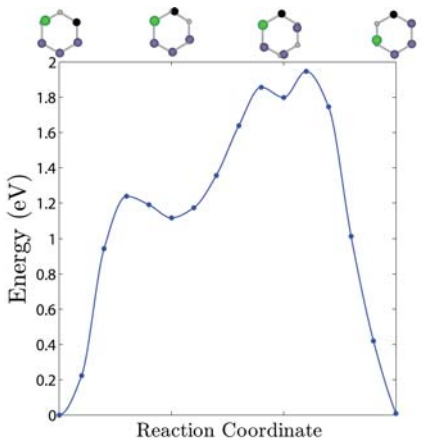

Figure 7.4.: Diffusion path of PV_{Ge} pairs in the presence of an Sb atom.

future theoretical work.

7.4. Conclusions

In this chapter, a GGA+U approach was used to quantify the influence of co-doping and the formation of PSbV_{Ge} clusters on the activation energy for migration of P or Sb in Ge. It is predicted that the formation of strongly bound PSbV_{Ge} clusters, results in the trapping of the $(\mathrm{P}V_{\mathrm{Ge}})^{-1}$ pair and retards its transport by increasing the migration activation energy. The present study is consistent with previous experimental studies but the exact mechanism of donor-vacancy cluster formation and deactivation in Ge needs to be further clarified.

8. Interaction of Palladium Defects in Germanium

8.1. Introduction

Metal induced lateral crystallisation (MILC) is regarded as an efficient pathway to produce polycrystalline-Ge with large grains, at much lower temperatures than Si [173]. Several metals are conventionally used as crystallisation inducers including copper (Cu) [174], nickel [175, 176] and palladium(Pd) [177], with the latter having the largest effect in reducing the crystallisation temperature [177, 178]. With MILC, Ge is grown on a thin film of Pd, which acts as a seed initiating crystallisation. The relative thickness [179] and residual Pd remaining after crystallisation are detrimental to device operations.

Unlike Si, diffusion in Ge is vacancy (V_{Ge}) mediated (established both theoretically and experimentally) [2, 122]. Experimental work carried out by Timmers *et al*. [180] suggests that Pd binds to a neighbouring Ge vacancy. This was further supported by Abiano *et al.* [181] who used a mixture of time differential perturbed angular correlation spectroscopy and DFT calculations to study the interactions of Pd with V_{Ge}, concluding that these are more bound under p-type than n-type doping conditions.

The aim of this chapter is to study in more detail the formation of charged Pd−defect clusters and determine their stability across the band gap of the host Ge crystal and also to investigate the migration energy of this defect through the lattice along with its electronic activity.

8.2. Methodology

The calculations presented employ the screened hybrid functional HSE06 [43, 44], as implemented in VASP [101]. The standard mixing fraction of 25% is used for the short-range portion of the exchange potential while the remaining 75% together with the long-range portion are described using the traditional semilocal potential given by the PBE functional [37]. The value of the screening parameter $\mu = 0.207$ Å^{-1}. Pseudopotentials employing projector-augmented wavefunctions [55] are used treating 4 and 10 electrons as valence for Ge and Pd respectively. To describe wavefunctions, a basis set using plane-waves was expanded up to 400 eV. Supercells with 64 atoms were used to model point defect interactions in Ge. The Brillouin zone was sampled using a $3 \times 3 \times 3$ mesh generated using the Monkhorst-Pack scheme [38]. Convergence tests presented in Chapter 2 showed that total energies were converged to within 2 meV. Energies and forces were iterated with tolerances set to 1×10^{-5} eV and 0.01 eV/Å respectively. Defect formation energies are calculated using Eq.5.2.

The chemical potential of Pd, μ_{Pd} is calculated as the energy per atom of Pd metal in its solid state assuming a face-centred cubic structure [182].

The calculations entail periodic repetitions of the supercells in space. This introduces spurious interactions that are inversely proportional to the defect-defect separation [58, 126]. The computational cost of hybrid calculations hinders the use of large supercells. An accurate and efficient scheme is needed to account for any unphysical Coloumbic interactions. One such scheme is that formulated by Freysoldt *et al.* [8, 9] which has proven efficient in several previous studies [183, 184].

8.3. Results and Discussions

The accuracy of the HSE06 functional is reflected in a good electronic and structural description of solid systems [67–69]. In the case of Ge a lattice parameter of 5.71 Å is obtained compared to the experimental value [71] of 5.66 Å at 0 K as was shown in Sec.3.2. In particular, a band gap for Ge was calculated which agrees well with experimental values.

Large substitutional atoms next to a vacancy in Ge often occupy a split-vacancy (split$-V_{\mathrm{Ge}}$) configuration [135] in which the substitutional species occupies an interstitial site with two adjacent V_{Ge}. The covalent radius of Pd is 1.39 Å[185] which is the same as that of tin (Sn) or antimony (Sb) both of which have been shown to favour the split$-V_{\mathrm{Ge}}$ configuration over a simple substitutional-vacancy ($\mathrm{Pd}_{\mathrm{Ge}}V_{\mathrm{Ge}}$) pair [117, 118]. Thus, the formation energies of $\mathrm{Pd}_{\mathrm{Ge}}V_{\mathrm{Ge}}$ and Pd$-$split$-V_{\mathrm{Ge}}$ were calculated in both the neutral state and for charges ranging from $+4$ to -4 as a function of the Fermi level as shown in Fig. 8.1. The difference in energy between $\{\mathrm{Pd}-\mathrm{split}{-}V_{\mathrm{Ge}}\}^q$ and $\{\mathrm{Pd}_{\mathrm{Ge}}V_{\mathrm{Ge}}\}^q$ is about 1 eV across the entire band gap. Therefore the split$-V_{\mathrm{Ge}}$ configuration is significantly more stable. This was not considered in previous studies and the assump-

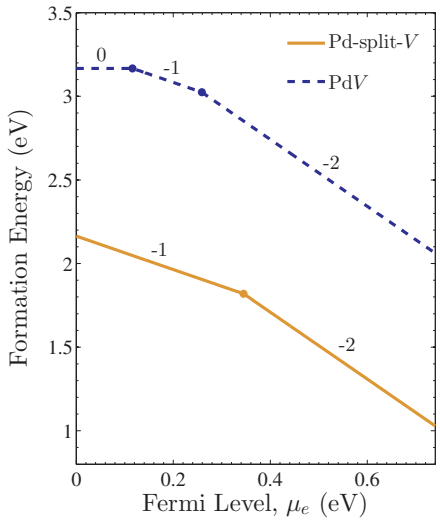

Figure 8.1.: Formation energies of Pd-vacancy pairs in the formal vacancy (PdV_{Ge}) and the split-vacancy (Pd-split-V_{Ge}) configuration.

tion was made that a Pd atom will occupy a substitutional site and pair with a neighbouring V_{Ge} [181]. Fig. 8.1 also shows that the neutral, -1 and -2 charge states are likely to form for $\{\mathrm{Pd}_{\mathrm{Ge}}V_{\mathrm{Ge}}\}^q$ while only the -1 and -2 charge states will exist for $\{\mathrm{Pd-split}{-}V_{\mathrm{Ge}}\}^q$. When the electron chemical potential is at the top of the valence band $\{\mathrm{Pd-split}{-}V_{\mathrm{Ge}}\}^{-1}$ has a formation energy of 2.16 eV which drops linearly with μ_e until a transition, $\epsilon(-/=)$, occurs at $\mu_e = 0.34$ eV (which is nearly half way through the band gap) to form $\{\mathrm{Pd-split}{-}V\}^{-2}$. The absence of other charge states can be attributed to the small band gap of Ge. This indicates that $\{\mathrm{Pd-split}{-}V_{\mathrm{Ge}}\}^q$ and $\{\mathrm{Pd}V_{\mathrm{Ge}}\}^q$ can act as single and double electron acceptors. Palladium atoms occupying interstitial and substitutional sites, $\mathrm{Pd_{int}}$ and $\mathrm{Pd_{Ge}}$ respectively, were also investigated for the same charge range. $\mathrm{Pd_{int}}$ appears only as a neutral species across the entire band gap (see solid line at 0.83 eV in Fig. 8.2). $\{\mathrm{Pd}_{\mathrm{Ge}}\}^q$ maintains a neutral charge state until a transition occurs at $\epsilon(0/-) = 0.46$ eV. Pd interstitials and substitutional atoms possess lower formation energies than $\{\mathrm{Pd-split}{-}V\}^q$, or $\{\mathrm{Pd}_{\mathrm{Ge}}V_{\mathrm{Ge}}\}^q$ pairs and as such they are expected to be present in higher concentrations.

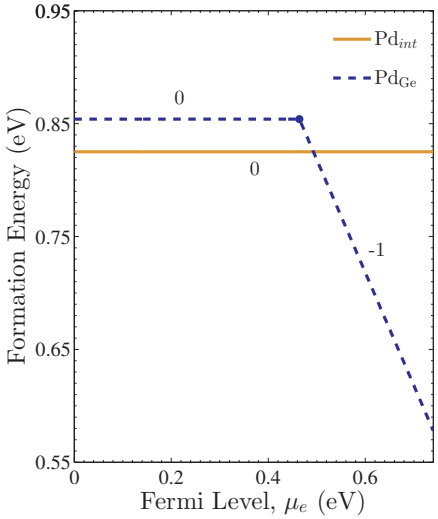

Figure 8.2.: Formation energies of substitutional and interstitial Pd defects.

It was observed experimentally that the concentration of $Pd_{Ge} - V_{Ge}$ pairs increased under p-doped compared to n-doped conditions [181]. This difference was attributed to size effects. At first sight this seems to be at variance with our calculations which indicate that the formation energy of $Pd_{Ge} - V_{Ge}$ pairs is higher closer to the top of the valence band. However, in order to maintain crystal charge neutrality, equal concentrations of unlike charges should be present at all times [186]:

$$\sum_{D,q} q[D^q] + [h^\bullet] - [e'] = 0 \tag{8.1}$$

where $[D^q]$ is the defect concentration, and $[h^\bullet]$ and $[e']$ are the hole and electron concentrations respectively. Therefore, unless there are charge compensating species present, low defect formation energies are not a guarantee for these defects to form. From Fig. 8.1, under p-doping conditions neutral and singly negatively charged Pd$-V$ pairs are present; the former will not need a compensating defect while the latter will need singly positively charged defect or holes in the valence band, which is accessible under p-type doping conditions.

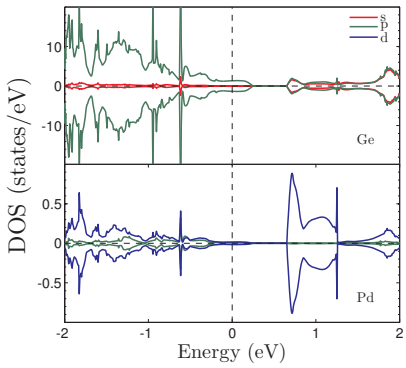

(a) Pd-split-V_{Ge}^{-1}

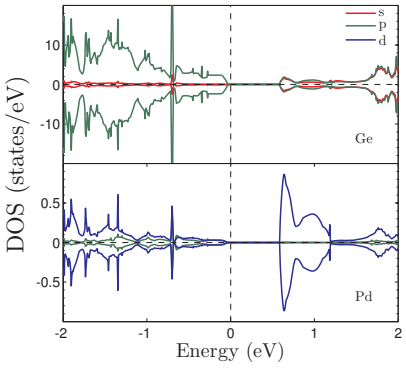

(b) Pd-split-V_{Ge}^{-2}

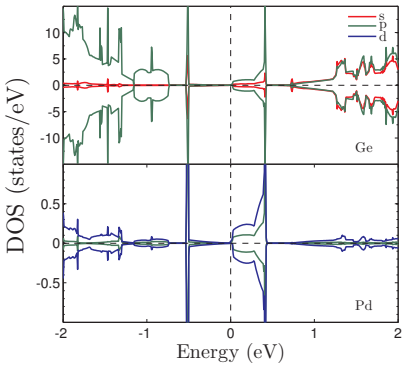

(c) $\mathrm{Pd}_{\mathrm{Ge}}^{0}$

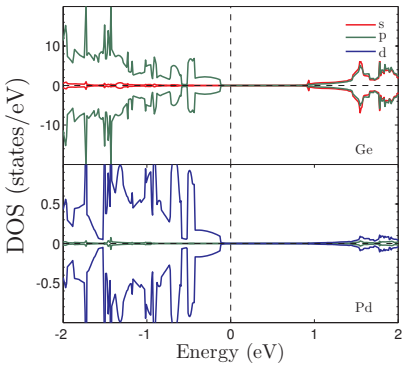

(d) $\mathrm{Pd}_{\mathrm{int}}$

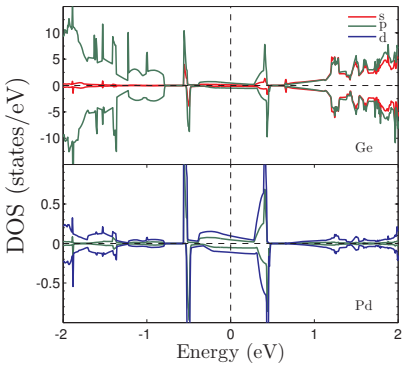

(e) $\mathrm{Pd}_{\mathrm{Ge}}^{-1}$

Figure 8.3.: The densities of states of the defects most likely to form in ascending order of stability, with Pd-split-V_{Ge}^{-1} being the least and $\mathrm{Pd}_{\mathrm{Ge}}^{-1}$ the most stable.

Figs. 8.3(a)-8.3(e) show the densities of states of the defects shown in Fig. 8.1 and 8.2 in increasing order of stability. In all cases, the top of the valence band is dominated by Ge$-p$ orbitals followed by Pd$-d$ orbitals. Fig. 8.3(a) and 8.3(b) show DOS for the split$-V_{\mathrm{Ge}}$ configuration. $\{\mathrm{Pd}-\mathrm{split}-{V_{\mathrm{Ge}}}^{-1}\}$ shows states due to Ge above the Fermi level close to the valence band.

The states introduced into the band gap would be detrimental to semiconductor device operation. After the transition to charge -2 we see that the Ge electronic structure is retained and the band gap recovers with the absence of any states within the band gap. This is also the case for $\mathrm{Pd}_{\mathrm{int}}$ which shows no states within the band gap. It should be noted that due to the small supercell size used, it is possible for defects in neighbouring images to interact forming an artificial band of states. This could explain the appearance of a continuous energy states throughout the band gap in the case of $\mathrm{Pd}_{\mathrm{Ge}}^{-1}$.

In Ge, vacancy mediated diffusion processes are common. Thus here the transport of Pd is modeled using the ring mechanism, which have been studied in previous chapters. This is shown on the top of Fig. 8.7. The migration barrier for this process, which corresponds to the step with the highest energy, is 1.77 eV. This is higher than the barriers calculated for atoms of similar size in Ge. In the case of Sb the barrier is 1.14 eV and for Sn it is 1.47 eV (see Chapter 5). This, coupled with the low formation energies of Pd defects, will result in them being mobile posing problems in devices requiring well defined dopants profiles.

Three more mechanisms for the diffusion of Pd were investigated. These are the direct interstitial mechanism, $\mathrm{Pd}_{\mathrm{int}} \rightleftharpoons \mathrm{Pd}_{\mathrm{int}}$, and the dissociative mechanism, $\mathrm{Pd}_{\mathrm{Ge}} \rightleftharpoons \mathrm{Pd}_{\mathrm{int}} + V_{\mathrm{Ge}}$, similar to the one used by Frank and Turnbull to explain the fast diffusion of Cu in Ge [7] and finally the kick-out mechanism in which an interstitial Pd atom moves towards a Ge atom displacing it from its normal lattice site towards an interstitial site and occupying its place, $\mathrm{Pd}_{\mathrm{int}} \rightleftharpoons \mathrm{Pd}_{\mathrm{Ge}} + \mathrm{Ge}_{\mathrm{int}}$.

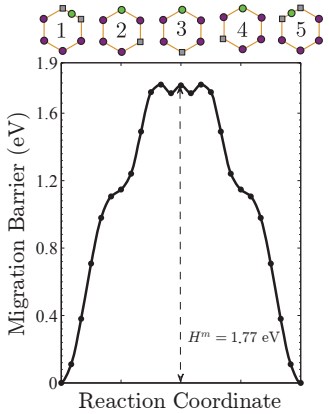

Figure 8.4.: The migration barrier for a PdV_{Ge} following the ring mechanism process of diffusion.

The mechanism of Pd diffusion in Ge exhibits a resemblance to the mechanism of Cu diffusion. The barrier for a direct interstitial mechanism of Pd in Ge is 0.03 eV which is very low making Pd a very fast diffuser in Ge (compare this to 0.08 eV for $\mathrm{Cu_{int}}$ in Ge [187]). The start and end points of Fig. 8.5 are hexagonal interstitial sites. The two barriers are due to Pd passing through tetrahedral sites, one before and one after the saddle point. The energies of these two sites differ by no more than 0.001 eV. The low formation energies of $\mathrm{Pd_{int}}$ (see Fig. 8.2) indicates that these defects will be present in high concentrations and can take part in diffusion processes.

The activation energy is defined as the sum of the formation and migration (H^m) energies of the defect under consideration [18]:

$$Q_a = E^f + H^m \tag{8.2}$$

This results in an activation energy of 0.86 eV. In comparison, the activation energy of direct interstitial diffusion of Cu in Ge was found to be 1.46 eV [188]. This indicates that Pd is a very fast diffuser in Ge.

The migration energy of $\mathrm{Pd_{Ge}}$ to move from a substitutional site into an intersti-

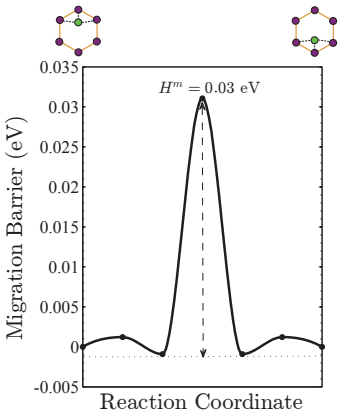

Figure 8.5.: The migration barrier for a direct interstitial process, $\mathrm{Pd_{int}} \rightleftharpoons \mathrm{Pd_{int}}$.

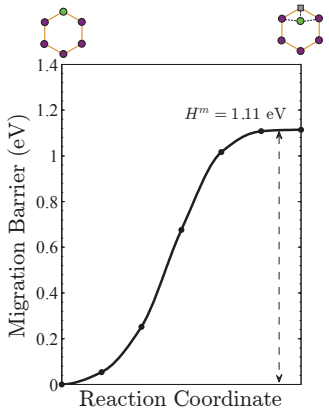

Figure 8.6.: The migration barrier for a dissociative mechanism (Frank-Turnbull [7]), $\mathrm{Pd_{Ge}} \rightleftharpoons \mathrm{Pd_{int}} + V_{\mathrm{Ge}}$.

tial site leaving a behind a vacancy is 1.11 eV as shown in Fig. 8.6. The reverse process, that is, $\mathrm{Pd_{int}} + V_{\mathrm{Ge}} \rightleftharpoons \mathrm{Pd_{Ge}}$ is a favourable process that proceeds without a kinetic barrier.

The kick-out mechanism by which $\mathrm{Pd_{int}}$ displaces a $\mathrm{Ge_{Ge}}$ has an energy barrier of 2.63 eV, whereas, the reverse reaction has a barrier of only 0.65 eV (see Fig. 8.7). It is therefore possible with the low interstitial formation energies to create a high concentration of Pd atoms which can diffuse via a direct interstitial mechanism, and which will follow a Frank-Turnbull mechanism when encountering a V_{Ge} forming $\mathrm{Pd_{Ge}}$. This can then be displaced by $\mathrm{Ge_{int}}$ as mentioned above

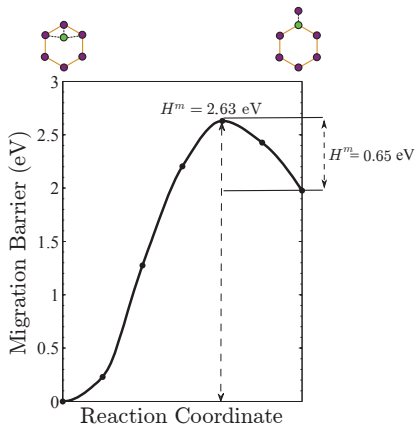

Figure 8.7.: The migration barrier for the kick-out mechanism, $\mathrm{Pd_{int}} \rightleftharpoons \mathrm{Pd_{Ge}} + \mathrm{Ge_{int}}$.

with a low barrier. This interplay between the three mechanisms above (direct interstitial, Frank-Turnbull and the kick-out mechanisms) can provide a pathway for diffusion of Pd in Ge at a low cost, making this defect very mobile.

8.4. Conclusions

In this chapter, first principles hybrid DFT was used to investigate the formation and interaction of Pd-vacancy pairs, Pd interstitial and substitutional defects. It was found that Pd favours a configuration where it is surrounded by two vacant sites. Interstitial and substitutional Pd are also found to be dominant given their low formation energies. Transport of Pd is facilitated by a direct interstitial mechanism coupled to Frank-Turnbull and Kick-out mechanisms, leading to highly mobile Pd defects. This, together with the fact that many of the Pd defects are electronically active, will overshadow many of the benefits brought about by speeding the crystallization process in Ge.

Part III.

Defects in III-V Semiconductors

Parts of this chapter have been published in Tahini *et al.* J. Appl. Phys. **114**, 063517 (2013) [184].

9. Vacancies in III-V Semiconductors

9.1. Introduction

The III-V family of semiconductors has been researched intensively for the past three decades. In particular, gallium arsenide (GaAs) is the most studied semiconductor after silicon [189] and many of its bulk properties are well understood and characterised [190].

The interest in these materials is due to their wide range of applications. For instance, gallium antimonide (GaSb) is of interest for mid-infrared optoelectronics and could play an important role in nanoelectronic devices [191]. GaAs, indium arsenide (InAs) and their ternary alloys are increasingly used in fabricating high speed electronics and they are at the heart of the *International Technology Roadmap for Semiconductors* [192, 193]. The direct gaps of materials such as InAs (0.42 eV), GaSb (0.81 eV) and indium phosphide (InP, 1.42 eV)

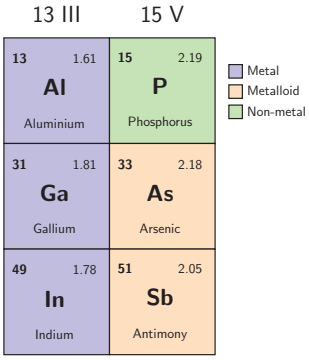

Figure 9.1.: Period III and V elements.

[194] make them efficient light emitters, particularly in lasers and light emitting diodes. The indirect band gap members (for example aluminium arsenide (AlAs) and aluminium antimonide (AlSb)) find use in radiation detectors, where the indirect band gap suppresses radiative recombination, allowing the electron-hole pair that was generated by an incoming photon more time to be detected.

With the constant downscaling and miniaturisation of electronic devices it is always crucial to understand the nature and the evolution of the defects formed during the growth processes and the interaction of these defects with various doping species. The most simple case, that of self-diffusion, is still not fully understood.

Atomic scale simulations are used extensively in studying III-V compounds [195–197]. Nevertheless, there are still many open questions related to the formation and migration of intrinsic and extrinsic defects and the charge transition levels of the various species.

The principal aim of this chapter is to provide a consistent and systematic survey of vacancies in binary III-V compounds. The chapter is organised as follows: in Sec. 9.2 the methodology is discussed in terms of the computational parameters employed. Sec. 2.4.1 briefly discusses the various charge correction schemes and the method of choice. Results regarding each III-V semiconductor are pre-

sented in Sec. 9.3. Finally, some remarks are made concerning trends, in terms of electronegativity and covalent atom radii, and conclusions are drawn.

9.2. Methodology

VASP [101] was employed to predict defect formation energies, atomic and electronic structure. Electron electron exchange and correlation is described according to the version of the GGA due to Perdew, Burke and Ernzerhof formalism [37]. Pseudopotentials were generated according to the PAW method [54] and a plane-wave basis with a cutoff energy of 400 eV was used. A few calculations were carried out using 64 atom supercells but the majority employed 216 atom supercells. The Brillouin zone was sampled according to the Monkhorst-Pack scheme [38] using meshes of $3 \times 3 \times 3$ and $2 \times 2 \times 2$ for the 64 and 216 supercells respectively, in order to maintain a **k**-point density as constant as possible across the various supercells. Energies and forces were iterated until convergence thresholds of 1×10^{-5} eV and 1×10^{-3} eV/Å were achieved respectively. The calculations were all spin-polarised and the simulations of the defect containing supercells were carried out under constant volume conditions (i.e. lattice parameters and angles were fixed) while allowing atoms to fully relax. Formation energies (E^f) were calculated based on the formulation of Zhang and Northrup [198] as detailed by El-Mellouhi and Mousseau [199]:

$$\begin{aligned} E^f = {} & E_{\mathrm{tot}}(D,q) - E_{\mathrm{tot}}(\mathrm{perfect}) + \sum_{\alpha} n_\alpha \mu_\alpha + q\mu_e \\ & \pm 1/2\Delta\mu + E_{\mathrm{corr}} \end{aligned} \tag{9.1}$$

where $E_{\mathrm{tot}}(D,q)$ is the energy of the defective cell with a charge q and $E_{\mathrm{tot}}(\mathrm{perfect})$ is the energy of the perfect cell. n_α is the number of atoms of type α that must

be added (negative n_α) or removed (positive n_α) to the supercell to create the defect, and μ_α is the chemical potential of species α. μ_e is the Fermi level referenced to the top of the valence band. $\Delta\mu$ is the chemical potential difference given by:

$$\Delta\mu = (\mu_{\text{V}} - \mu_{\text{III}}) - (\mu_{\text{V}}^{\text{bulk}} - \mu_{\text{III}}^{\text{bulk}}) \tag{9.2}$$

The upper sign of $\Delta\mu$ in Eq. 9.1 stands for group V vacancies and the lower sign stands for group III vacancies. This term has upper and lower bounds given by $-\Delta G \leq \Delta\mu \leq +\Delta G$, where ΔG represents the Gibbs free energy of formation of a compound and is given by:

$$\Delta G_{\text{III}-\text{V}} = \mu_{\text{III}-\text{V}}^{\text{bulk}} - \mu_{\text{III}}^{\text{bulk}} - \mu_{\text{V}}^{\text{bulk}}. \tag{9.3}$$

Finally, E_{corr} is a formation energy correction term generated using the Freysoldt *et al.* scheme [8, 9].

In this work standard PBE was used rather than hybrid functionals. In several cases hybrid functionals have been shown to outperform other functionals in describing the electronic structure and optical properties of materials, and thus, they were assumed to be accurate and superior in all other cases. However, the focus here is not on the absolute values of the formation energies but rather on the the trends produced by changes in the composition from group III to group V as will be shown in Sec. 9.3.

9.3. Results

9.3.1. Lattice, Elastic, Thermodynamic and Electronic Properties

The effectiveness of the computational approach used to predict property trends is first tested by calculating the lattice parameters, thermodynamic, electronic

and elastic properties of III-V binary compounds (see Chapter 3). Lattice parameters are all in fairly good agreement with experimental data but, as expected from GGA calculations, are all slightly overestimated in comparison with experiments. The calculated Gibbs free energy of formation as defined by Eq. 9.3 were compared with experimental values as presented in Sec.3.3.4, and are all within the level of accuracy expected using this technique [84, 85]. Conversely, predicted dielectric constants are both larger and smaller than experimental values. Compounds incorporating larger atoms have higher dielectric constants. The elastic constants (c_{11}, c_{12} and c_{44}) are shown in Table 3.6. Again the predictions follow the experimental data with compounds (AlP, AlSb, GaP and GaSb) showing very good agreement. Overall, the computational approach is seen to reproduce a range of perfect lattice properties including those (i.e. elastic and dielectric constants) that are important indicators of the ability to model the response of a lattice to the incorporation of a defect.

9.3.2. Charge Correction

As mentioned above, in order to correct for the spurious interactions between the periodic charged defects, the correction scheme due to Freysoldt *et al* [8, 9] was employed. The technique has been demonstrated to efficiently correct for charged defect interactions in smaller supercells [183, 200]. Tests were performed on charged Ga and P vacancies in GaP using 64 and 216 atom supercells (see Fig. 9.2). The uncorrected energies derived from the two cells clearly differ for higher charges. The application of the charge correction scheme brings these values into agreement, within $\sim$0.1 eV per vacancy.

The corrected results will be presented along with their interpretation focusing on the stoichiometric conditions of the crystal. The figures show that the formation energies change under different growth conditions although we will initially discuss defects under stoichiometric conditions.

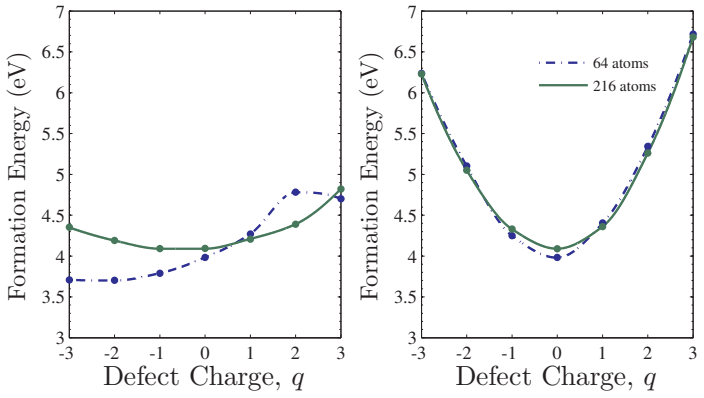

(a) V^q_{Ga}

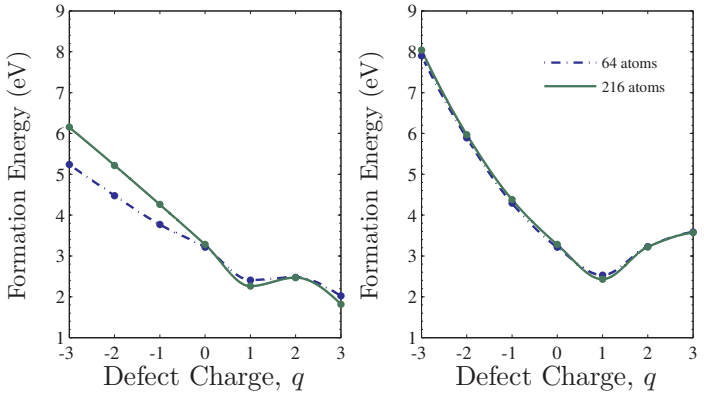

(b) V^q_{P}

Figure 9.2.: Formation energies of (a) Ga and (b) P vacancies in GaP using 64 atom and 216 atom supercells. The left panels are the uncorrected energies while those on the right are the formation energies corrected using the correction scheme due to Freysoldt *et al.* [8, 9]. Lines are guide to the eye.

9.3.3. Aluminum-Ⅴ Compounds

9.3.3.1. Aluminium Phosphide

AlP is an indirect band gap semiconductor (E_g=2.5 eV) that has found application in light emitting diodes. Unlike other Ⅲ-Ⅴ materials this compound has not been widely studied and as such many defect properties are incompletely understood. A few studies [201, 202] were carried out on AlP that mostly focused on

the electronic structure. Fig. 9.3 shows the formation energies of vacancies in AlP for the charge that is most likely to form (i.e. of lowest energy at a given value of the Fermi level). Thus aluminium vacancies are most stable in their neutral, -1, -2 or -3 charge states depending on the level of doping in the material. Positive charge states have higher formation energies and are thus not likely to form. The formation energy of V_{Al}^{0} is 4.42 eV at a Fermi level of 0 eV and under stoichiometric conditions. Here and subsequently, the term stoichiometric conditions is used to imply $\Delta\mu = 0$, that is assuming a dilute limit where the elemental compositions are equal. This point occurs by definition between the two extrema which corresponds to group $\mathbb{III}$ ($\Delta\mu = -\Delta G$) and group $\mathbb{V}$ ($\Delta\mu = \Delta G$) rich conditions [203]. The defect formation energy then indicate the driving force to alter the stoichiometry of the system. This defect begins to decrease in concentration as the charged defect V_{Al}^{q} starts to form as the Fermi level increases. The formation energies of charged defects can fall as low as 1.26 eV (for V_{Al}^{-3}). The defect energy transition levels, $\epsilon(0/-)$ and $\epsilon(-/=)$ occur at 0.81 eV and 1.42 eV above the valence band and $\epsilon(= / \equiv)$ occurs at 0.38 eV below the conduction band. For all charges V_{Al}^{q} exhibits T_d point group symmetry.

Phosphorous vacancies occur in the $+1$, 0, -1, -2 charge states. Under extreme p-doping conditions V_{P}^{+1} will have a formation energy of $\sim$ 2.61 eV; this will keep rising with increasing μ_e until the neutral vacancy becomes dominant under nearly intrinsic doping conditions, with a formation energy of 3.88 eV. The lower formation energy of V_{P}^{+1} implies that up to $\mu_e = 1.2$ eV P vacancies will dominate in AlP, and beyond this V_{Al}^{-2} and V_{Al}^{-3} are more easily formed.

9.3.3.2. Aluminium Arsenide

AlAs, with a 2.23 eV indirect band gap, is important for high electron mobility transistors and optoelectronic devices [194]. It exhibits trends similar to those of AlP in terms of what charge states are favourable and the dominant vacancy at

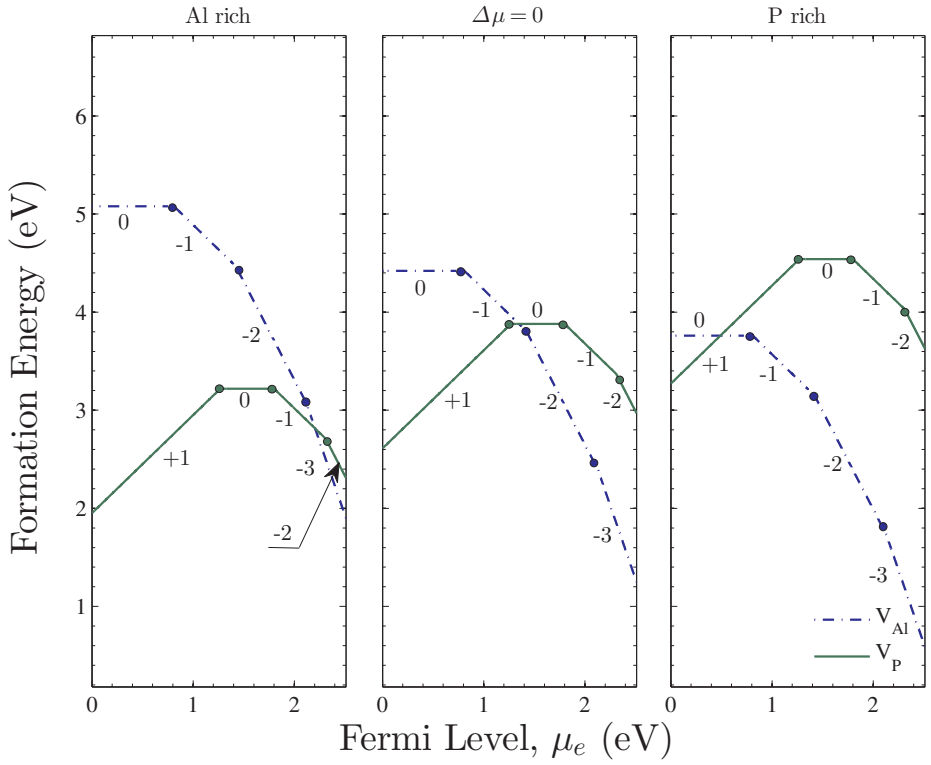

Figure 9.3.: Lowest energy vacancy formation energies for V^q_{Al} and V^q_{P} in AlP assuming the most stable charge state (neutral or charged) as a function of the Fermi level.

a given doping level. V^0_{Al} is most stable under heavy to moderate p-doping with a formation energy of 3.62 eV. Under intrinsic conditions V^{-1}_{Al} and V^{-2}_{Al} are most likely to compete as they both have similar formation energies but, as would be expected, at higher Fermi level the more negative charge state will become more prevalent. The V^q_{Al} defect level transitions occur at or near the middle of the band gap implying that they are all deep level traps. The point group symmetry of V^q_{Al} in all the charge states considered here is T_d.

V^q_{As} favours the $+1$ charge state under p-doping up to intrinsic levels where V^0_{As} with a formation energy of 3.83 eV prevails. With higher n-doping levels the vacancy captures more electrons moving from 0, -1 to -2 with formation energies reaching 2.42 eV in highly n-doped regimes. This is also accompanied

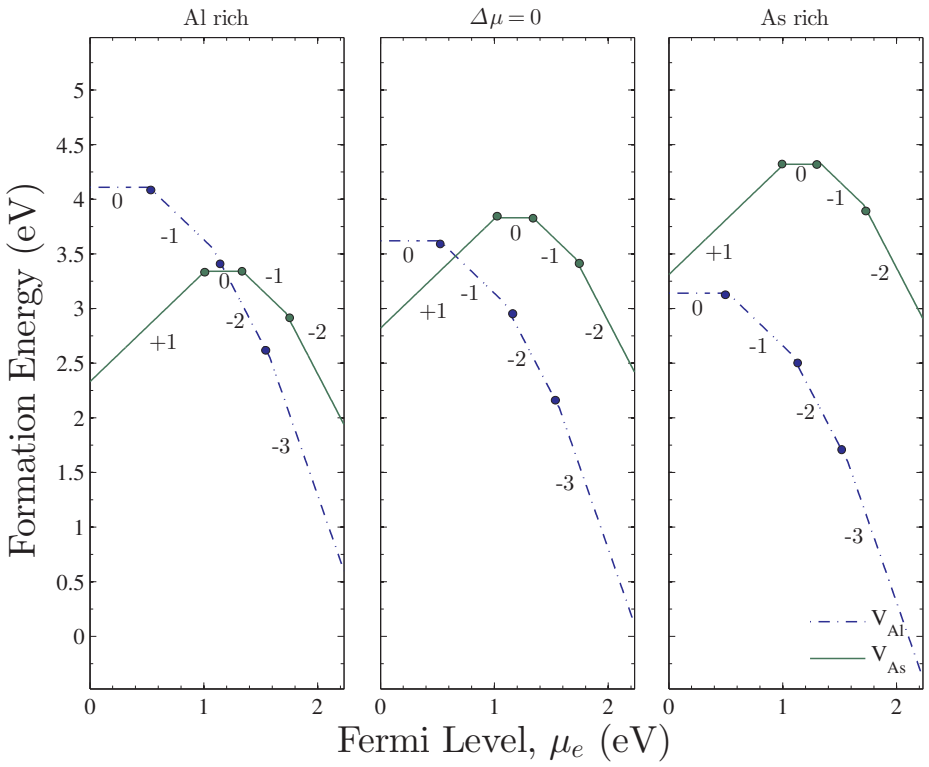

Figure 9.4.: Lowest energy vacancy formation energies for V^q_{Al} and V^q_{As} in AlAs assuming the most stable charge state (neutral or charged) as a function of the Fermi level.

by a series of changes in point group symmetry from D_{2d} for V^0_{As} to C_{2v} for V^{-1}_{As} and back to D_{2d} for V^{-2}_{As}. The formation energies of these defects remain, however, higher than the corresponding values for V^q_{Al}, which for most of the Fermi level region maintain a difference of about 1 eV from V^q_{As}.

9.3.3.3. Aluminium Antimonide

Similar to AlP and AlAs, AlSb has an indirect band gap of 1.69 eV with applications in long-wavelength optoelectronic and photon detectors [204]. Fig. 9.5 suggests that V^0_{Al} appears only for a narrow range of Fermi levels close to the valence band. This then gives way to -1, -2 and the -3 charge states. V^0_{Al}

has a formation energy of 2.61 eV, which is the same value obtained by Åberg *et al.* [205]. The formation energies for negatively charged states fall until, under heavy doping conditions, the formation energy of V_{Al}^{-3} drops to a negative value of about -0.5 eV, close to the prediction of Du [206]. This implies that under heavy n-doping conditions it will be energetically favourable for V_{Al}^{-3} to form.

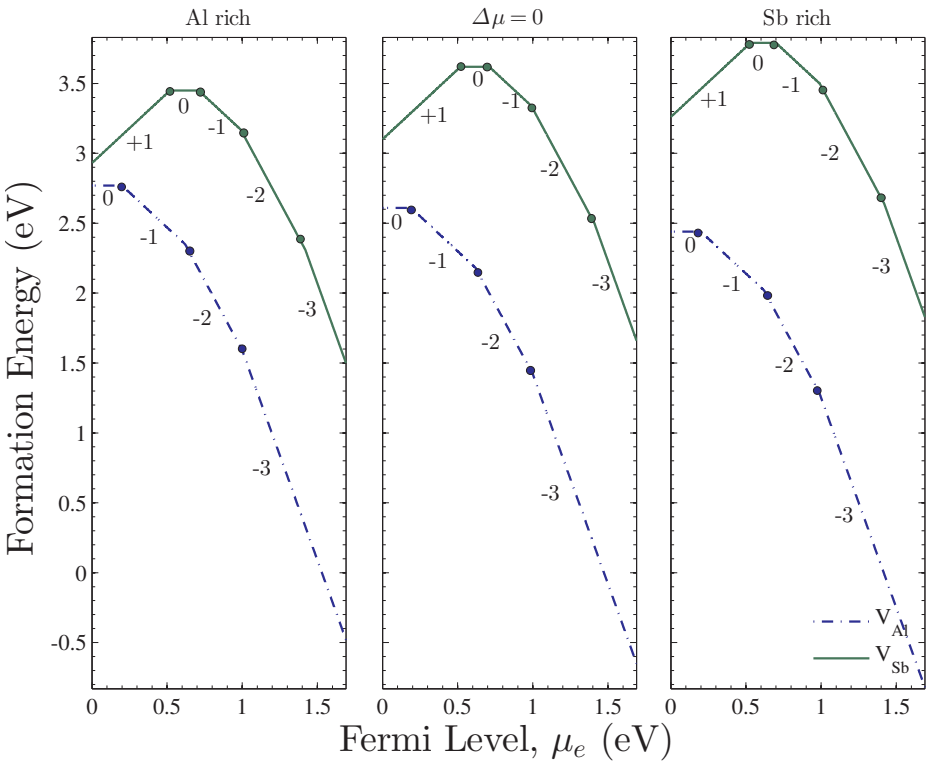

Figure 9.5.: Lowest energy vacancy formation energies for V_{Al}^{q} and V_{Sb}^{q} in AlSb assuming the most stable charge state (neutral or charged) as a function of the Fermi level.

V_{Sb}^{q} has higher formation energies than V_{Al}^{q} across the entire bandgap. Under p-doping the $+1$ charge state will form and remains stable up to $\mu_e = 0.55$ eV where the neutral vacancy supersedes it with a formation energy of 3.62 eV. This value is only slightly different to that reported by Åberg *et al.* [205], who calculated an equivalent energy of 3.42 eV.

9.3.4. Gallium-$\mathbb{V}$ Compounds

9.3.4.1. Gallium Phosphide

GaP has a 2.35 eV indirect band gap, and when doped with nitrogen could be used in light emitting diodes. The vacancies and defect levels have been studied from both experimental and computational points of view [207–210]. V_{Ga}^{0} has a formation energy of 4.09 eV, which is in good agreement with the value of 4.17 eV reported by Höglund *et al.* [210]. The neutral vacancy V_{0}^{Ga} is only present at low values of μ_e, and is rapidly replaced by negatively charged vacancies as μ_e rises In the first half of the band gap V_{Ga}^{-1} and V_{Ga}^{-2} are more likely to form, but give way to V_{Ga}^{-3} from close to intrinsic doping conditions up to extreme Ga n-doping conditions. The stable transition levels $\epsilon(0/-)$, $\epsilon(-/=)$ and $\epsilon(=/\equiv)$ occur at 0.24 eV, 0.72 eV and 1.18 eV respectively above the valence band and hence form shallow and deep defect transition levels.

V_{P}^{+1} starts from the top of the valence band with a formation energy of 2.43 eV and continues to about 0.9 eV above the valence band when it captures an electron forming V_{P}^{0} with an energy of 3.28 eV, in good agreement with the value predicted by Höglund *et al.* [210] of 3.33 eV. This species appears to be stable under light p-doping beyond which -1, -2 and -3 charge states form respectively. The defect transition levels $\epsilon(+/0)$, $\epsilon(0/-)$, $\epsilon(-/=)$ occur at 0.85, 1.10 and 1.59 eV above the valence band respectively and $\epsilon(=/\equiv)$ at 0.28 eV below the conduction band.

9.3.4.2. Gallium Arsenide

GaAs has been studied extensively [211–215]. Its 1.52 eV direct band gap makes it suitable for uses ranging from integrated circuits to solar cells [189]. Remarkably, Fig. 9.7 indicates an absence of neutral Ga or As vacancies. V_{Ga}^{q} does

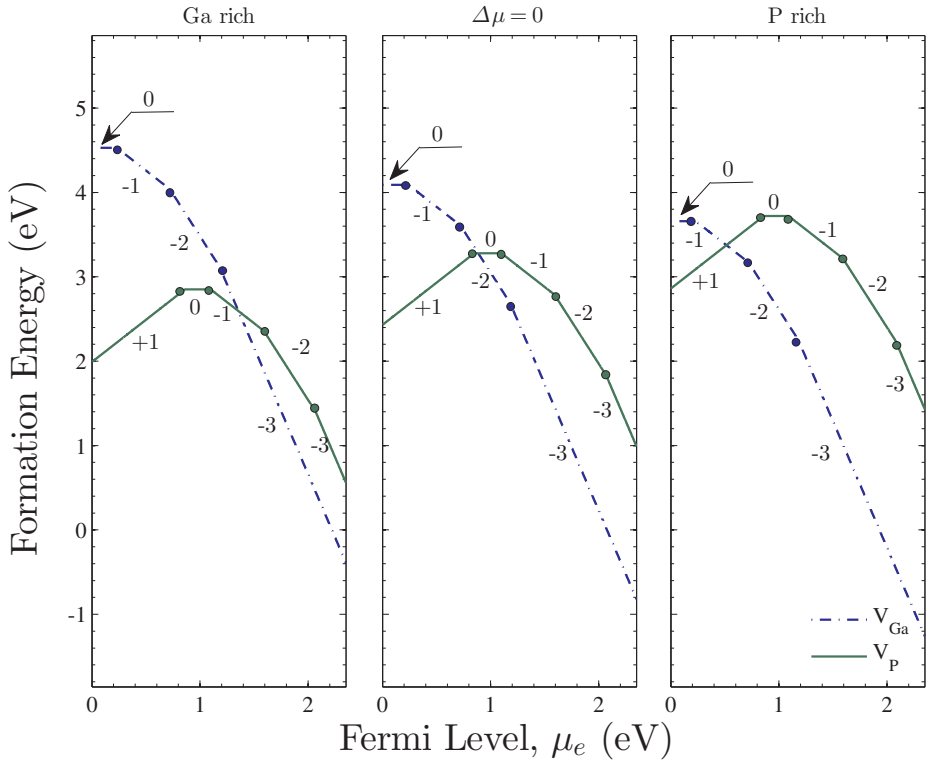

Figure 9.6.: Lowest energy vacancy formation energies for V^q_{Ga} and V^q_{P} in GaP assuming the most stable charge state (neutral or charged) as a function of the Fermi level.

not favour any of the positively charged states and it starts by adopting the -1 charge at the top of the valence band. The defect level transition $\epsilon(-/=)$ occurs at 0.45 eV followed by $\epsilon(=/\equiv)$ at 0.79 eV above the valence band implying that under intrinsic and n-doping conditions V^{-3}_{Ga} is the most prevalent charge state. V^{+1}_{As} has the lowest formation energy of 2.49 eV at the top of the valence band, but captures two electrons when the Fermi energy reaches 0.56 eV to form V^{-1}_{As}. This is known as a negative-*U* transition, which is consistent with the observations of El-Mellouhi and Mousseau [199] and in agreement with other work [215–217]. The negative-*U* transition, $\epsilon(+/-)$, takes place at 0.56 eV above the valence band. The other two transitions, $\epsilon(-/=)$ and $\epsilon(=/\equiv)$, occur at 0.49 eV and 0.18 eV below the conduction band. The neutral and negatively charged As

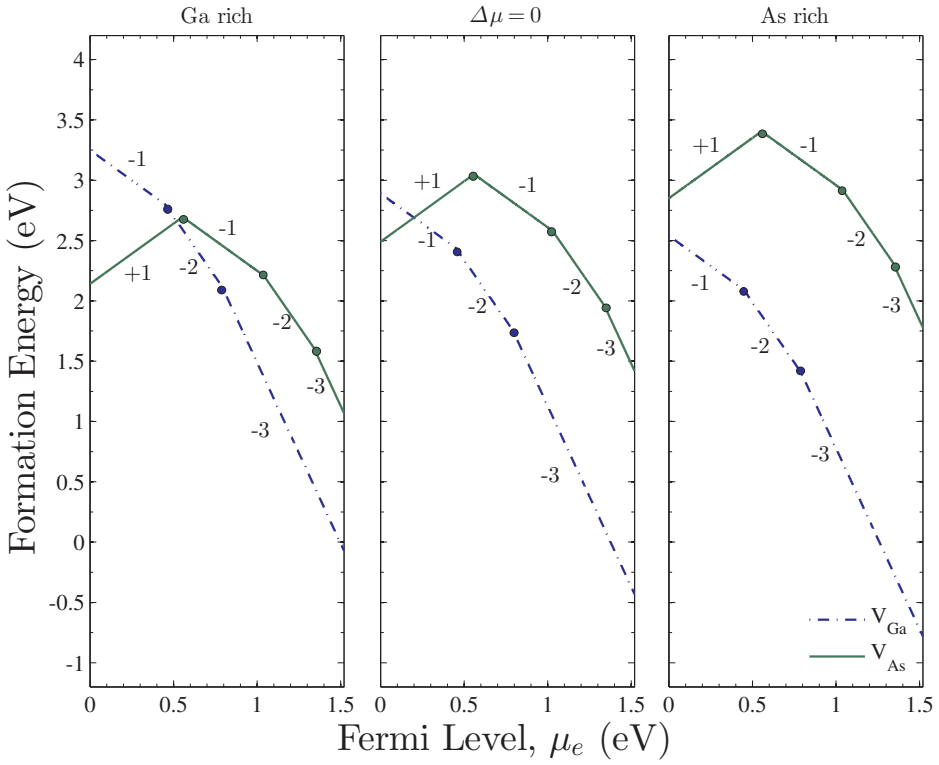

Figure 9.7.: Lowest energy vacancy formation energies for V^q_{Ga} and V^q_{As} in GaAs assuming the most stable charge state (neutral or charged) as a function of the Fermi level.

vacancies exhibit D_{2d} point group symmetry while V^{+1}_{As} possesses C_{3v} symmetry. Even though its existence is not predicted, the calculated value for the formation of V^0_{As} at $\Delta\mu = 0$ is 3.07 eV compared to 2.85 eV predicted by Murphy *et al.* [218].

9.3.4.3. Gallium Antimonide

GaSb is an intermediate band gap material (E_g=0.81 eV) that could be used in laser diodes, high frequency devices and photodetectors with high quantum efficiency [191].

In GaSb, V^0_{Ga} occurs at doping levels near the top of the valence band with a for-

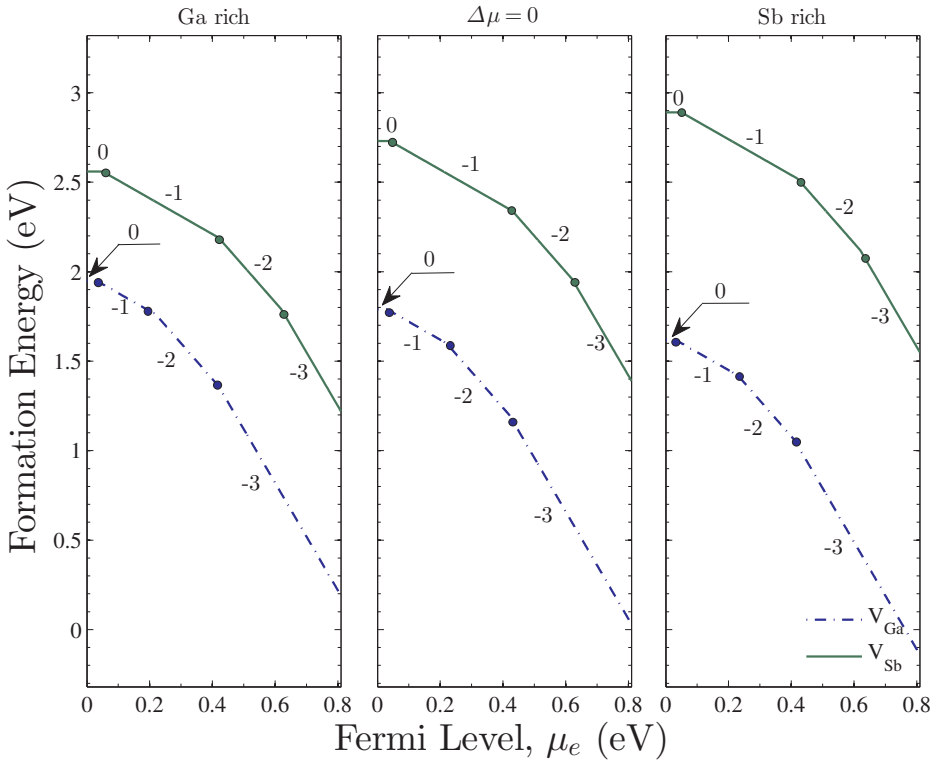

Figure 9.8.: Lowest energy vacancy formation energies for V^q_{Ga} and V^q_{Sb} in GaSb assuming the most stable charge state (neutral or charged) as a function of the Fermi level.

mation energy of 1.79 eV. This undergoes a transition to V^{-1}_{Ga} at $\epsilon(0/-)$= 0.03 eV, which renders it a shallow state. With increasing Fermi level, higher negative charge states form leading to two more transitions $\epsilon(-/=)$ and $\epsilon(=/\equiv)$ at 0.22 and 0.42 eV above the valence band. Under very high n-doping conditions V^{-3}_{Ga} will achieve very low formation energies ($\sim$ 0.05 eV). V^q_{Sb} follows similar trends to those of V^q_{Ga}. V^0_{Sb} has a formation energy of 2.73 eV, which is 0.94 eV higher than V^0_{Ga}. The formation energies of Sb vacancies remain 1.2-1.4 eV higher than those of Ga vacancies at any given level of μ_e reported here. These large differences in the formation energies between the two species suggest that V^q_{Ga} will dominate and are likely to have much higher concentrations than V^q_{Sb}. This has significant consequences for the self-diffusion in GaSb. The prevalence of V^q_{Ga}

for all the charge states and values of μ_e considered is consistent with the significantly higher diffusion of Ga (diffusion mechanism involving V_{Ga}) compared with Sb [167, 219].

9.3.5. Indium-$\mathbb{V}$ Compounds

9.3.5.1. Indium Phosphide

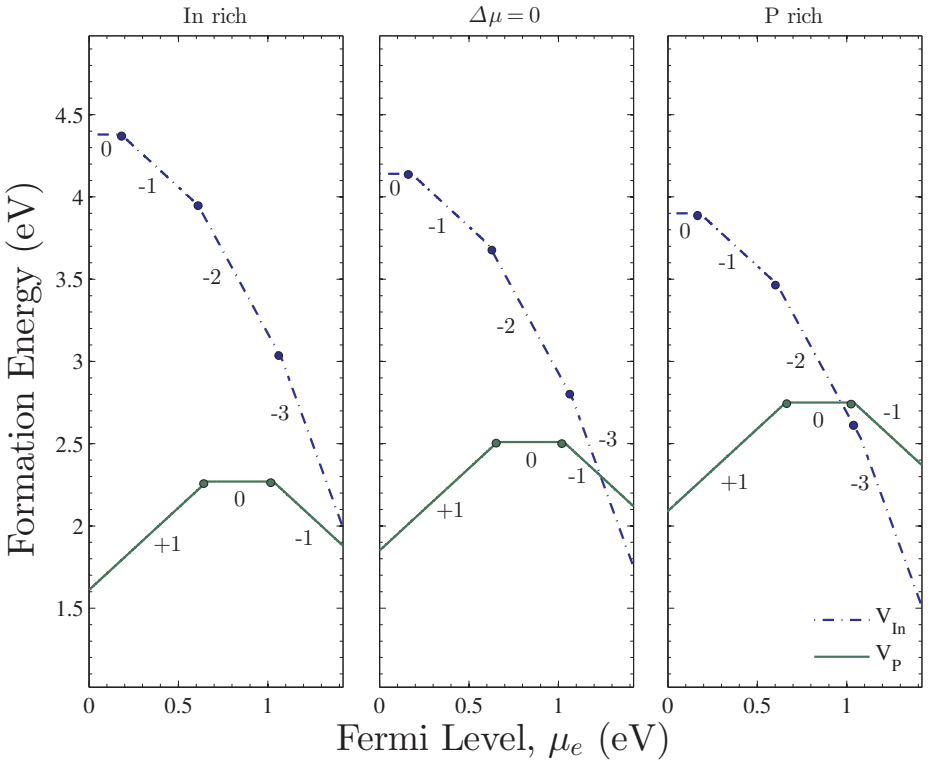

Figure 9.9.: Lowest energy vacancy formation energies for V_{In}^q and V_{P}^q in InP assuming the most stable charge state (neutral or charged) as a function of the Fermi level.

InP is used as a substrate in optoelectronic devices and as a high-frequency electronic material due to its high electron mobility [220]. The calculated value for the formation energy of V_{In}^0 is 4.14 eV, in good agreement with several previously calculated values [221–223]. The neutral vacancy is stable above the

valence band and in the extreme p-doping regime, but eventually captures an electron forming V_{In}^{-1} with a transition $\epsilon(0/-)$=0.18 eV. The following transitions $\epsilon(-/=)$ and $\epsilon(=/\equiv)$ occur at 0.61 and 1.08 eV respectively. V_{P}^{+1} becomes dominant from the top of the valence band with a formation energy of 1.85 eV, which is 2.29 eV less than V_{In}^{0}. $\epsilon(+/0)$ occurs at 0.66 eV where V_{P}^{0} becomes more favourable with a formation energy of 2.51 eV. A second transition, $\epsilon(0/-)$, takes place at 1.03 eV. V_{P}^{+1} exhibits T_d point group symmetry, while V_{P}^{0} and V_{P}^{-1} possess D_{2d} point group symmetry.

The lower formation energy of V_{P}^{q} compared to V_{In}^{q} for a wide Fermi level range (up to $\mu_e \sim 1.23$ eV) implies that until the high n-doping regime P vacancies will be the dominant species.

9.3.5.2. Indium Arsenide

InAs has a small direct band gap of 0.42 eV and as such has been used in long-wavelength optoelectronics and electron quantum wells [194]. The In vacancy forms in three charge states 0, -1 and -2. V_{In}^{0} has a formation energy of 3.01 eV and dominates at the lower end of the Fermi level. At $\epsilon(0/-)$=0.06 eV V_{In}^{-1} is favoured and dominates over a wide Fermi level range until μ_e=0.35 eV whereupon V_{In}^{-2} forms. However, V_{In}^{q} remains much higher in energy than V_{As}^{q}, which under p-doping and light n-doping occurs as V_{As}^{+1} with a formation energy of 2.00 eV at the top of the valence band. The stability of V_{As}^{+1} extends to μ_e=0.27 eV at which point V_{As}^{0} forms at a cost of 2.27 eV in agreement with the value 2.30 eV reported by Murphy *et al.* [218]. The As vacancy maintains a much lower formation energy than V_{In}^{q} suggesting that this will be the major vacancy defect during the actual growth conditions of the crystal (see Sec. 9.4).

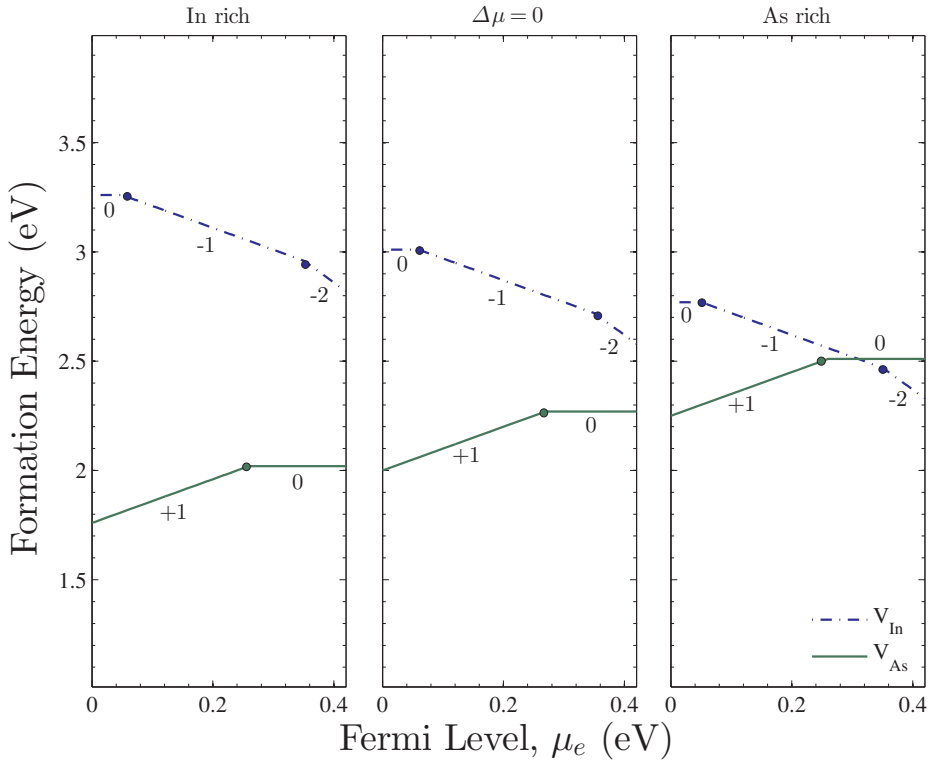

Figure 9.10.: Lowest energy vacancy formation energies for V^q_{In} and V^q_{As} in InAs assuming the most stable charge state (neutral or charged) as a function of the Fermi level.

9.3.5.3. Indium Antimonide

InSb has one of the smallest band gaps in the III-V family of semiconductors (E_g=0.24 eV) and possesses the highest electron mobility. These properties make it useful in infrared optoelectronics including infrared detectors [224]. The small band gap limits the possibility of different charge states forming and hence limits the defect level transitions to at most one. For nearly the entire Fermi level range V^{-1}_{In} dominates except under extreme n-doping conditions when the transition $\epsilon(-/=) = 0.23$ eV results in V^{-2}_{In} with a formation energy of 2.44 eV. On the other hand, Sb vacancies have much lower formation energies starting with 1.62 eV for V^{+1}_{Sb} at the top of the valence band. This transforms into V^{0}_{Sb} at $\mu_e = 0.03$ eV with a formation energy of 1.65 eV. These values are both much

lower than those for V_{In}^{q}.

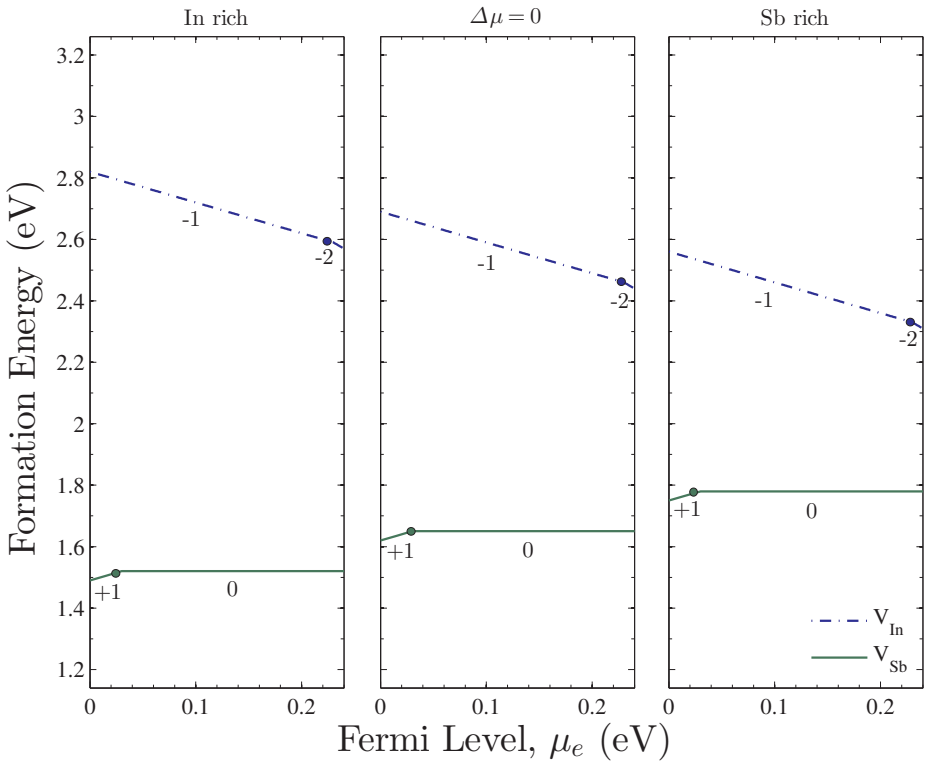

Figure 9.11.: Lowest energy vacancy formation energies for V_{In}^{q} and V_{Sb}^{q} in InSb assuming the most stable charge state (neutral or charged) as a function of the Fermi level.

9.4. The Influence of Growth Conditions: Stoichiometry

The above analysis assumed stoichimetric conditions, defined such that the compoundsâĂŹ chemical potentials satisfy $\Delta\mu = 0$. Varying $\Delta\mu$ between $-\Delta G$ (group Ⅲ rich) and $+\Delta G$ (group Ⅴ rich) allows investigation of poor and rich growth conditions, which might be present when synthesising the various compounds. In AlSb and GaSb the difference between the formation energies of Al and Ga vacancies on one side and Sb vacancies on the other is at least 0.49 eV and 0.94 eV respectively for stoichiometric conditions. Even under group Ⅲ rich

conditions Al and Ga vacancies remain lower in energy in these two compounds as E^f in Eq. 9.1 will only increase by $+\Delta G/2$ which is 0.165 and 0.16 eV in AlSb and GaSb respectively (see Fig. 9.5 and Fig. 9.8). The current values also indicate an equivalent situation for InSb, where group $\mathbb{V}$ vacancies will still dominate even under group $\mathbb{V}$ rich conditions (see Fig. 9.11) as $+\Delta G/2$ in this case is 0.13 eV. Thus, for AlSb, GaSb and InSb, the dominant vacancy is independent of the changes in growth conditions across the whole Fermi energy spectrum. For the other six compounds, however, growth conditions can alter the dominant vacancy type at some (although not necessarily all) values of the Fermi energy. For instance, both V^q_{Al} and V^q_{As} dominate in AlAs under Al rich and stoichiometric conditions depending upon the Fermi level. However, under As rich conditions, V^q_{Al} becomes dominant across the whole band gap (see Fig. 9.4). GaAs behaves similarly so that while V^q_{Ga} is always dominant under As rich conditions, irrespective of the Fermi level, V^q_{As} defects are dominant under Ga rich conditions for Fermi levels of less than 0.6 eV. For higher Fermi levels V^q_{Ga} again dominates.

9.5. Trends in Formation Energies

In order to investigate the influence of the physical properties of group $\mathbb{V}$ atoms on the vacancy formation energies, the compounds were categorised into three sets, Al-$\mathbb{V}$, Ga-$\mathbb{V}$ and In-$\mathbb{V}$ (where $\mathbb{V}$ = P, As and Sb). The Al-$\mathbb{V}$ compounds favour the formation of V^q_{Al} for larger group $\mathbb{V}$ ions. AlP tends to favour $V^q_{\mathbb{V}}$ in the first half of the band gap and then favours V^q_{Al} in the second half. Conversely, for AlAs, V^q_{Al} dominates at lower Fermi levels. Finally, in AlSb V^q_{Al} prevails across the Fermi level. The changes in the formation energies and these trends can be in part attributed to the electronegativities and the covalent bond radii of the constituents. The electronegativities of the group $\mathbb{V}$ elements change as P(2.19)→As(2.18)→Sb(2.05) and the covalent radii as P(1.07

Å)→As(1.19 Å)→Sb(1.39 Å) [185]. A similar trend is seen for Ga-Ⅴ where V^q_{Ga} is the favourable vacancy species and for GaSb, in particular, V^q_{Ga} forms with a much lower energy than V^q_{Sb}. However, for In-Ⅴ the situation is different: the group Ⅴ vacancies are the lower energy species and only in InP does V^q_{In} form and then only under high n-doping conditions.

Table 9.1.: The formation energies of the group Ⅲ and group Ⅴ vacancies (eV) for $\mu_e = E_g/2$ under stoichiometric conditions ($\Delta\mu = 0$). The values in parentheses correspond to the charge of the vacancy under intrinsic conditions.

	$V_{\mathrm{Ⅲ}^q}$		
	P	As	Sb
Al	3.98 (-1)	3.00 (-2)	1.74 (-2)
Ga	2.70 (-2)	1.82 (-2)	1.23 (-2)
In	3.51 (-2)	2.86 (-1)	2.57 (-1)
	$V_{\mathrm{Ⅴ}^q}$		
	P	As	Sb
Al	3.86 (+1)	3.83 (0)	3.50 (-1)
Ga	3.20 (-1)	2.85 (-1)	2.36 (-1)
In	2.51 (0)	2.21 (+1)	1.65 (0)

To further investigate these trends, the formation energies of $V^q_{\mathrm{Ⅲ}}$ and $V^q_{\mathrm{Ⅴ}}$ are shown in Table 9.1 for $\mu_e = E_g/2$, which to a good approximation corresponds to the Fermi level of an intrinsic semiconductor [70]. The formation energies decrease across the rows of the tables, that is, with increasing anion size and decreasing electronegativity. This trend is not surprising given that electrons are less bound to less electronegative atoms (which form weaker bonds that are easier to break, hence forming a vacancy with a relatively lower formation energy (see Table 9.1)). AlP and AlAs anion vacancies have almost the same formation energies of 3.86 and 3.83 eV at intrinsic Fermi levels, which is reflected by the similar anion electronegativities of 2.19 and 2.18 for P and As respectively. Conversely, Sb has a much lower electronegativity, which is reflected by the different and lower vacancy formation energy. The same is observed for Ga-Ⅴ and In-Ⅴ,

Table 9.2.: The transition levels (in eV above the VBM) of group III and group V vacancies.

System	Defect	Transition			
		$\epsilon(+1/0)$	$\epsilon(0/-)$	$\epsilon(-/=)$	$\epsilon(=/\equiv)$
AlP	V^q_{Al}	$\cdots$	0.81	1.42	2.13
	V^q_{P}	1.27	1.80	2.31	$\cdots$
AlAs	V^q_{Al}	$\cdots$	0.52	1.09	1.57
	V^q_{As}	1.01	1.34	1.71	$\cdots$
AlSb	V^q_{Al}	$\cdots$	0.19	0.62	1.00
	V^q_{Sb}	0.52	0.71	0.99	1.41
GaP	V^q_{Ga}	$\cdots$	0.24	0.72	1.18
	V^q_{P}	0.85	1.10	1.59	2.07
GaAs	V^q_{Ga}	$\cdots$	$\cdots$	0.45	0.79
	V^q_{As}	0.56	$\cdots$	1.03	1.34
GaSb	V^q_{Ga}	$\cdots$	0.03	0.22	0.42
	V^q_{Sb}	$\cdots$	0.04	0.43	0.62
InP	V^q_{In}	$\cdots$	0.18	0.61	1.08
	V^q_{P}	$\cdots$			$\cdots$
InAs	V^q_{In}	$\cdots$	0.06	0.35	$\cdots$
	V^q_{As}	0.27	$\cdots$	$\cdots$	$\cdots$
InSb	V^q_{In}	$\cdots$	$\cdots$	0.23	$\cdots$
	V^q_{Sb}	0.03	$\cdots$	$\cdots$	$\cdots$

where the antimonides always have much lower formation energies than other members in any given set.

Another important feature that can be seen in Figs. 9.3–9.11 is the absence of

positive charge states for the group III vacancies. Also, group V vacancies do not exhibit a positive charge beyond +1. There is some ambiguity in the literature about the stable charge states for each of the vacancy defects. For example the work here agrees with Du [206] and Åberg *et al.* [205] who predict 0, −1, −2 and −3 charge states for V^q_{Al} in AlSb; however, Åberg *et al.* [205] predict charges for V^q_{Sb} ranging from +3 to −2. In the case of GaAs the predicted charge states agree with El-Mellouhi and Mousseau [199], but are at variance with those of Schultz and von Lilienfeld [215] and Northrup and Zhang [225] who predict the stability of V^{+3}_{As}. Significantly El-Mellouhi and Mousseau [199] used the Makov-Payne [60] technique to correct for charged defects whereas Schultz and von Lilienfeld [215] and Northrup and Zhang [225] did not employ such correction schemes. For GaSb, we find that both vacancies are stable in charge states ranging from 0 to -3 depending on the Fermi level, which is in agreement with Virkkala *et al.* [226] in the case of V^q_{Ga}. However, they predict the stability of V^{+3}_{Sb} under high p-doping conditions, which exhibits a negative-*U* transition to the +1 charge state. Again we find a discrepancy when comparing to the work of Höglund *et al.* [227] who studied InP, InAs and InSb. They found that in InP V^q_{In} exists in the −3 and −4 charge states and in InAs only the −3 state, whereas the In vacancy in InSb undergoes a negative-U transition from charge state -1 to charge state -3, which are the only two stable states. These variations could stem in part from the different parameters used, such as the pseudopotentials and the supercell size. In particular the charge corrections which are quite substantial for the highly charged states do not normally yield the same results when different schemes are used.

9.6. Summary

Vacancies in III-V semiconductors were investigated using first principle calculations. The formation energies were calculated for each vacancy, in different

charge states, as a function of the Fermi level under stoichiometric conditions but also for Ⅲ and Ⅴ rich conditions. The correction scheme due to Freysoldt *et al.* [8, 9] was used throughout to correct for all charged defect interactions.

Considering vacancies at the semiconductor intrinsic Fermi level ($\mu_e = E_g/2$), the formation energies decrease with increasing ion size and decreasing electronegativity of the group Ⅴ ion. It is calculated that group Ⅲ vacancies and group Ⅴ vacancies have charge states in the range -3 to 0 and -3 to 1 respectively depending upon the Fermi level.

Fabrication of Ⅲ-Ⅴ semiconductors requires control of the concentrations of the defects that mediate transport, which include vacancies. This can be achieved by altering the growth conditions, that is, making Ⅲ or Ⅴ rich or poor. The results presented here suggest, however, that for Ⅲ-Sb the growth conditions do not alter the preference for one vacancy over the other. For all other compounds changing the growth conditions can change the type of the dominant vacancy at some values of the Fermi level but not for all Fermi level values.

The present systematic comparison of vacancy defects in the most important group Ⅲ-Ⅴ semiconductors aims to serve as a roadmap for future investigations.

10. Antisites in III-V Semiconductors

10.1. Introduction

In the previous chapter we discussed the formation of vacancies in binary III-V semiconductors under various growth conditions. We were able to demonstrate a trend in the formation energies and relate that to the electronegativities and covalent radii of the constituent atoms. We also showed that the antimonides prefer a specific type of vacancy regardless of the growth conditions.

In this chapter, the focus will be on the formation of antisite defects in this family of semiconductors. In highly ionic systems antisite defects are less favourable due to the high Coulombic penalty to place an atom in the wrong sublattice [18]. However, in covalent materials the tendency to form antisites becomes greater as will be shown in the subsequent sections.

10.2. Methodology

The calculations were performed using Vienna *Ab initio* Simulation Package [101] with parameters controlling pseudopotentials, energy and forces convergence criteria similar to those described in Chapter 9. The calculations were performed in a 216 atom supercell and the Brillouin zone was sampled using a Monkhorst-Pack grid [38] of $2 \times 2 \times 2$. Formation energies and the growth conditions are described by Eqs. 9.1 and 9.3. Charged defect interactions were corrected using the scheme due to Freysoldt *et al.* [8, 9] which was tested and described previously (see sections 2.4.5 and 9.3.2).

10.3. Results and Discussions

10.3.1. Aluminium-$\forall$ Compounds

10.3.1.1. Aluminium Phosphide

Under stoichiometric conditions P_{Al}^{q} is much easier to form than Al_{P}^{q}. Under p-doping conditions P_{Al}^{q} forms in the $+2$ charge state with a formation energy of 1.41 eV at the top of the valence band. This rises up to a Fermi level of 0.61 eV when a transition to $+1$ charge state occurs. P_{Al}^{0} occurs from near the middle of the band gap and extends up to the n-doping region with a formation energy of 3.01 eV before making transitions to -1 and -2 at $\mu_e = 1.95$ eV and $\mu_e = 2.12$ eV respectively. Al_{P}^{q} forms in the $+1$ charge state at a much higher formation energy (2.47 eV higher than P_{Al}^{+2} at the VBM). At $\mu_e = 0.59$ eV a transition to the neutral state occurs.

As we move towards Al-rich conditions Al_{P}^{q} becomes the dominant defect for the entire range of the band gap. The formation energy of P_{Al}^{+2} is about 0.2

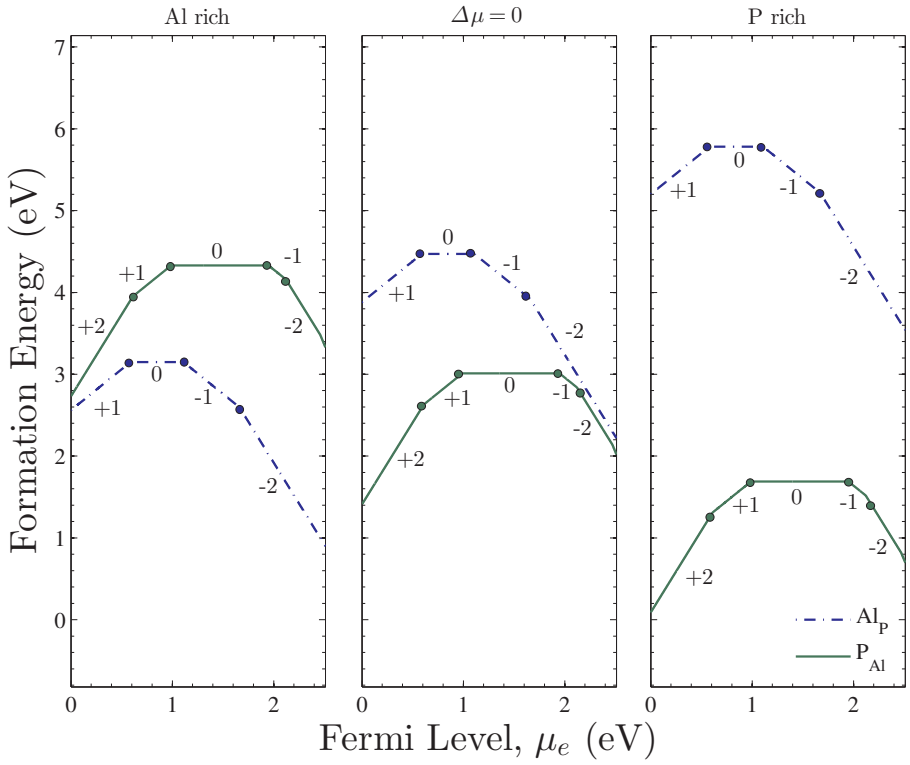

Figure 10.1.: Lowest antisite formation energies for Al_P^q and P_{Al}^q in AlP assuming the most stable charge state (neutral or charged) as a function of the Fermi level.

eV higher than that of Al_P^{+1} at the VBM. However, due to their charges, the formation energies of the two antisites diverge and the difference becomes more than 1 eV from the middle of the band gap up to the CBM where it reaches 2.45 eV.

As was mentioned above, P_{Al}^q is favoured under stoichiometric conditions; it is therefore even more favourable in the P-rich regime. At the top of the valence band P_{Al}^{+2} has a very low formation energy of 0.09 eV whereas Al_P^{+1} forms at 5.20 eV rendering it highly unlikely to be found in equilibrium even as the Fermi level is shifted towards the CBM.

10.3.1.2. Aluminium Arsenide

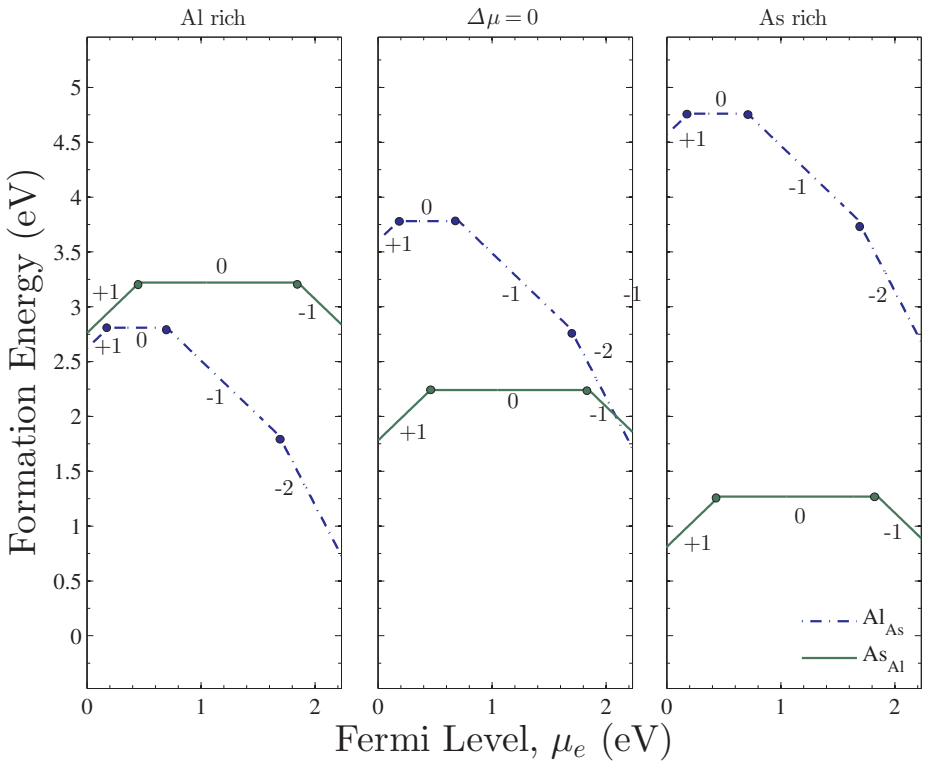

Figure 10.2.: Lowest antisite formation energies for Al^q_{As} and As^q_{Al} in AlAs assuming the most stable charge state (neutral or charged) as a function of the Fermi level.

For stoichiometric conditions, As^q_{Al}, which can form in the $+1$, neutral and -1 charge states, exhibits lower formation energies than Al^q_{As} which in addition to the charge states exhibited by As^q_{Al} can also form in the -2 charge state. At the top of the valence band As^{+1}_{Al} needs 1.78 eV to form with a transition occurring at $\mu_e = 0.46$ eV to As^0_{Al} which extends into the n-doping regime where an electron is accepted at $\mu_e = 1.85$ eV to form As^{-1}_{Al}. Under p-doping and at the middle of the band gap Al^q_{As} is unlikely to form due to its large formation energy compared to As^q_{Al}. This starts to change rapidly as a transition $\epsilon(-/=)$ occurs at 1.68 eV which causes its formation energy to drop enough for it to form under extreme n-doping conditions.

Under Al-rich conditions Al^q_{As} is dominant for the entire band gap with the separation in formation energies between Al^q_{As} and As^q_{Al} reaching its maximum of 2.1 eV at the CBM. Moving to As-rich conditions will favour the Arsenic antisites for the whole Fermi level region with large formation energy difference between the two antisites (3.76 eV and 1.90 eV at the VBM and CBM respectively) making Al^q_{As} unlikely to form in equilibrium.

10.3.1.3. Aluminium Antimonide

AlSb exhibits a behaviour different to that of AlP or AlAs such that no one single specie is favoured under certain growth conditions for the entire band gap.

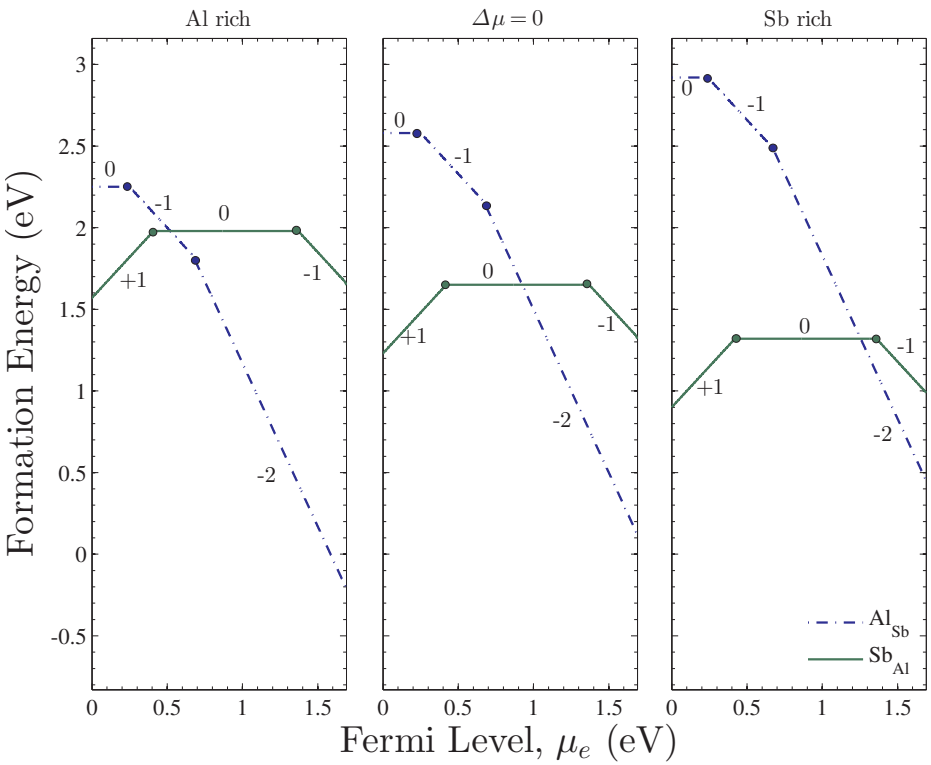

Figure 10.3.: Lowest antisite formation energies for Al^q_{Sb} and Sb^q_{Al} in AlSb assuming the most stable charge state (neutral or charged) as a function of the Fermi level.

Under stoichiometric conditions Sb^{q}_{Al} which exists in singly positively, neutral or singly negatively charged states dominates under p-doping conditions. At the VBM the formation energy of Sb^{+1}_{Al} is 1.23 eV. This undergoes a transition to Sb^{0}_{Al} at $\mu_e = 0.41$ eV. The region of stability of Sb^{0}_{Al} extends the middle of the band gap into the n-doping regime. Al^{q}_{Sb}, on the other hand, can form in the neutral, singly negatively and doubly negatively charged states. The transitions $\epsilon(0/-)$ and $\epsilon(-/=)$ occur at 0.25 eV and 0.67 eV respectively. The -2 charge on Al^{-2}_{Sb} guarantees that its formation energy will fall rapidly and will overtake that of Sb^{q}_{Al} at $\mu_e = 0.93$ eV until it reaches its minimum of 0.11 eV at the CBM.

Moving towards Al-rich conditions will lower the overall formation energies of Al^{q}_{Sb} while at the same time raising that of Sb^{q}_{Al} allowing the Al antisites a wider range of stability which extends from $\mu_e = 0.52$ eV to the CBM. Below this Fermi level Sb^{+1}_{Al} will dominate under p-doping conditions and also marginally in the neutral charge state (see the left panel of Fig. 10.3). Under Sb-rich conditions the preferences are reversed. Now, Sb^{q}_{Al} will exist over a wider Fermi level range extending from the VBM for which it has a formation energy of 0.90 eV up to $\mu_e = 1.23$ eV where Al^{q}_{Sb} takes over. The formation energy of Al^{q}_{Sb} antisites decreases as the level of n-doping is increased until its lowest formation energy of 0.45 eV is achieved at the CBM.

10.3.2. Gallium-∇ Compounds

10.3.2.1. Gallium Phosphide

In GaP, Ga^{q}_{P} and P^{q}_{Ga} show a competition under p-doping conditions where the difference in formation energy is only about 0.7 eV at the VBM with P^{q}_{Ga} being the favourable specie. As the P antisite is in the $+2$ charge state, its formation energy increases with the Fermi level until a transition to the $+1$ charge state occurs at 0.48 eV; the formation energy of the singly charged antisite also increases

with Fermi energy, but at a slower rate. This increase reduces the difference in formation energies with the Ga antisite which exists very briefly in the $+1$ charge state which acts as a shallow acceptor with a transition at $\mu_e = 0.07$ eV to the neutral charge state and a further transitions to the -1 charge state at $\mu_e = 1.00$ eV.

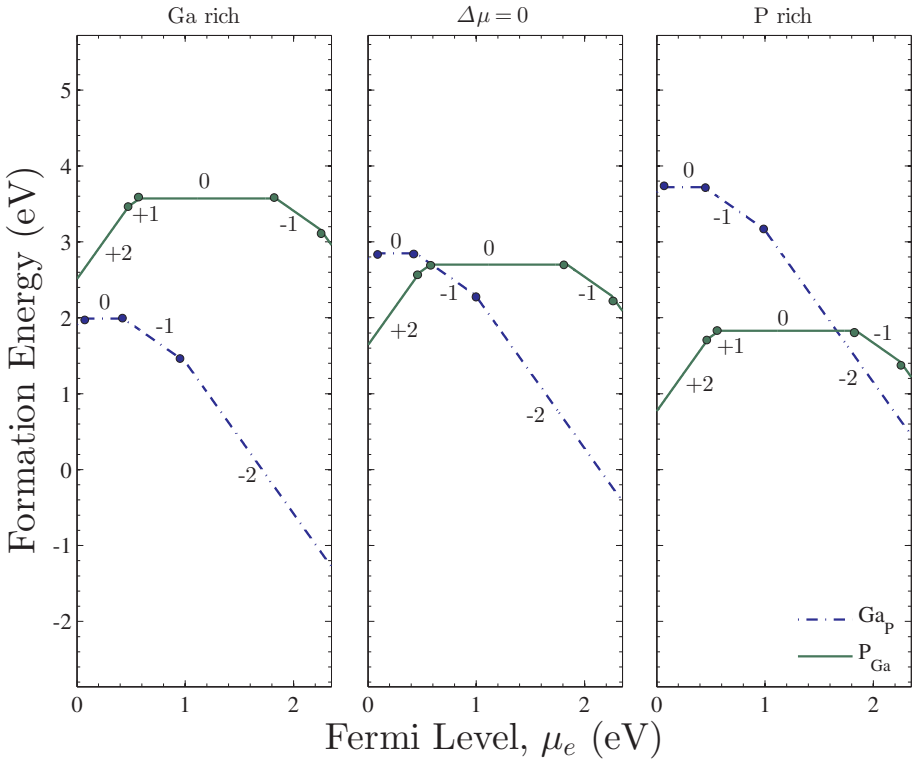

Figure 10.4.: Lowest antisite formation energies for Ga_P^q and P_{Ga}^q in GaP assuming the most stable charge state (neutral or charged) as a function of the Fermi level.

Above a Fermi level of 0.59 eV Ga_P^{-1} becomes the lowest energy specie. This defect accepts an additional electron as the Fermi level rises above 1.05 eV, making it more sensitive to further changes in the Fermi level. Under extreme n-doping conditions, but before the Fermi energy reaches the CBM, its formation energy drops below 0 eV.

Under Ga-rich conditions, Ga antisites are clearly the favoured species for the

entire band gap with the much higher formation energy of P^q_{Ga} hindering their formation in comparison to their Ga counterparts. In the realm of P-rich growth conditions, P^q_{Ga} are stable for a wider range of values of the Fermi energy and are only superseded by Ga^q_P at $\mu_e = 1.66$ eV.

10.3.2.2. Gallium Arsenide

Antisites and their complexes are widely studied in GaAs [228, 229] as many interesting optical and electrical properties are attributed to them. These include the EL2 centres which are deep donor levels at the midgap [230, 231], the presence of which was associated to As_{Ga} under As-rich conditions [231, 232].

In GaAs, the two antisites, Ga^q_{As} and As^q_{Ga}, are possible to form under stoichiometric conditions. As^q_{Ga} is favoured under p-doping up to a Fermi level of 0.52 eV when Ga^q_{As} takes over. As^q_{Ga} is stable in the +1 and neutral charge states. As^0_{Ga} has a formation energy of 1.95 eV which is in close agreement with the results of Pöykkö *et al.* [217] who obtained 2.29 eV for the same defect under the same conditions. The stable charges for Ga^q_{As} are -1, -2 and -3. These highly negative charges will lead to a rapid decrease in the formation energies of Ga^q_{As} defects with increasing Fermi level.

Under Ga-rich conditions, Ga^q_{As} dominates for the entire of the band gap. Ga^0_{As} has a formation energy of 1.50 eV which is comparable to the 1.70 eV found by Northrup and Zhang [225]. As mentioned above, the -2 and -3 charge states of the Ga^q_{As} antisite imply a rapid decrease in its formation energy as a function of the Fermi level. Above $\mu_e = 1.19$ eV the formation energy drops below zero.

As-rich growth conditions will favour As^q_{Ga} for most of the band gap. Only under extreme n-doping conditions will Ga^{-3}_{As} become favourable having nearly the same formation energy as As^{-2}_{Ga}. For comparison the calculated formation ener-

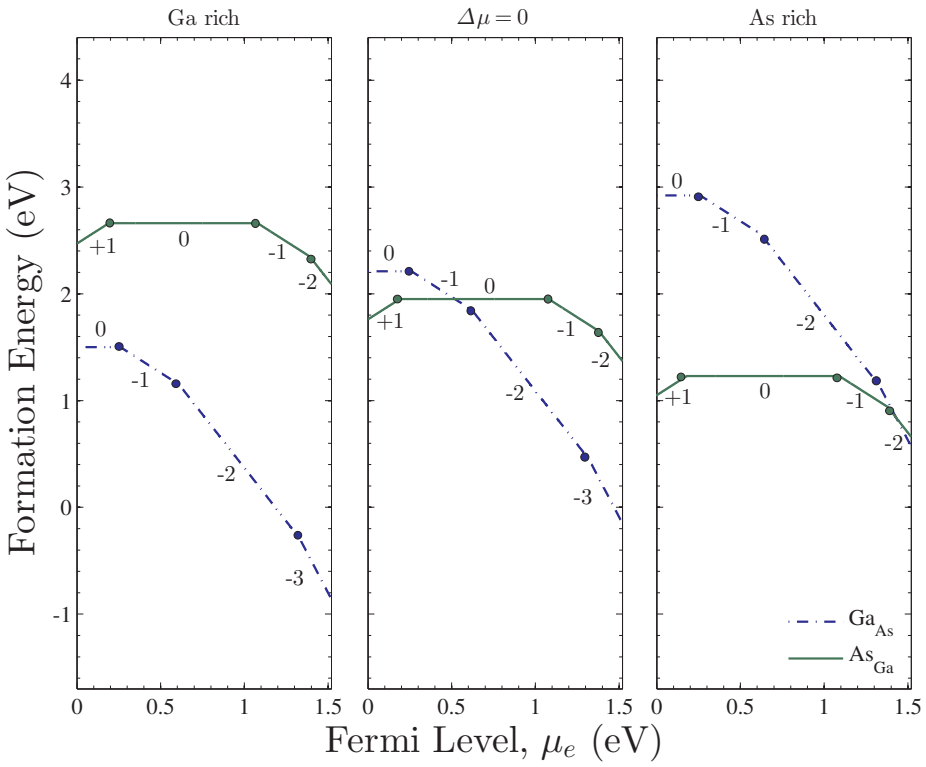

Figure 10.5.: Lowest antisite formation energies for Ga^q_{As} and As^q_{Ga} in GaAs assuming the most stable charge state (neutral or charged) as a function of the Fermi level.

gies for As^q_{Ga} and Ga^q_{As} are 1.23 eV and 2.92 eV respectively which is in very good agreement with the results of Schultz and von Lilienfeld [215] which are 1.27 eV and 3.20 eV for these defects under As-rich conditions. As^0_{Ga} is normally associated with EL2 centres either directly or in complexes incorporating V_{Ga} and As_{int} [215, 231, 232]. Experimentally two defect levels are linked to the EL centres one at $E_v + 0.54$ eV due to the $\epsilon(+2/+1)$ transition and the other at $E_v + 0.77$ eV due to $\epsilon(+1/0)$ transition [233]. Using PBE the +2 charge state is not predicted to be stable (see Fig. 10.5), whereas $\epsilon(+1/0)$ occurs at $E_v + 0.19$ eV. The recent work by Komsa *et al.* [234] addressed this issue by assessing the various functionals used to study As^q_{Ga} and came to the conclusion that hybrid functionals are required for accurate defect levels (see also Sec. 12.2.1). However, the

conclusions regarding the dominance of a certain defect under various growth conditions are not expected to change qualitatively as the difference in formation energies between some of these defects exceeds 1 eV on many occasions.

10.3.2.3. Gallium Antimonide

For GaSb, Ga^{q}_{Sb} is stable in the neutral charge state at the VBM with a formation energy of 1.09 eV which is 0.36 eV lower than that of Sb^{+1}_{Ga}. This result is in good agreement with Hakala et al. [235], whose calculated formation energy for Ga^{0}_{Sb} is 1.13 eV. This implies a complete dominance of Ga^{q}_{Sb} throughout the band gap under stoichiometric conditions as is shown in Fig. 10.6. The Ga^{0}_{Sb} antisite is only stable over a narrow range of Fermi energies above the VBM, before accepting an electron to form Ga^{-1}_{Sb}; the shallow Sb acceptor level is at $\epsilon(0/-)$=0.04 eV which is identical to that calculated by Hakala *et al.* [235]. The second transition occurs at $\epsilon(-/=) = 0.27$ eV, again in good agreement with $\epsilon(-/=) = 0.26$ eV calculated by Hakala *et al.* [235].

Under Ga-rich conditions, the stability of Ga^{q}_{Sb} is further enhanced. Ga^{-2}_{Sb} will attain sub-zero formation energy beyond a Fermi level of 0.53 eV i.e when the material is just slightly under n-type doping.

For Sb-rich conditions, Sb^{q}_{Ga} will be able to form in +1 charge state under p-doping conditions but captures an electron and is converted into the neutral state as the Fermi energy increases. However, even under Sb-rich conditions Ga^{q}_{Sb} is still going to form and will surpass Sb^{q}_{Ga} in concentration beyond $\mu_e = 0.19$ eV.

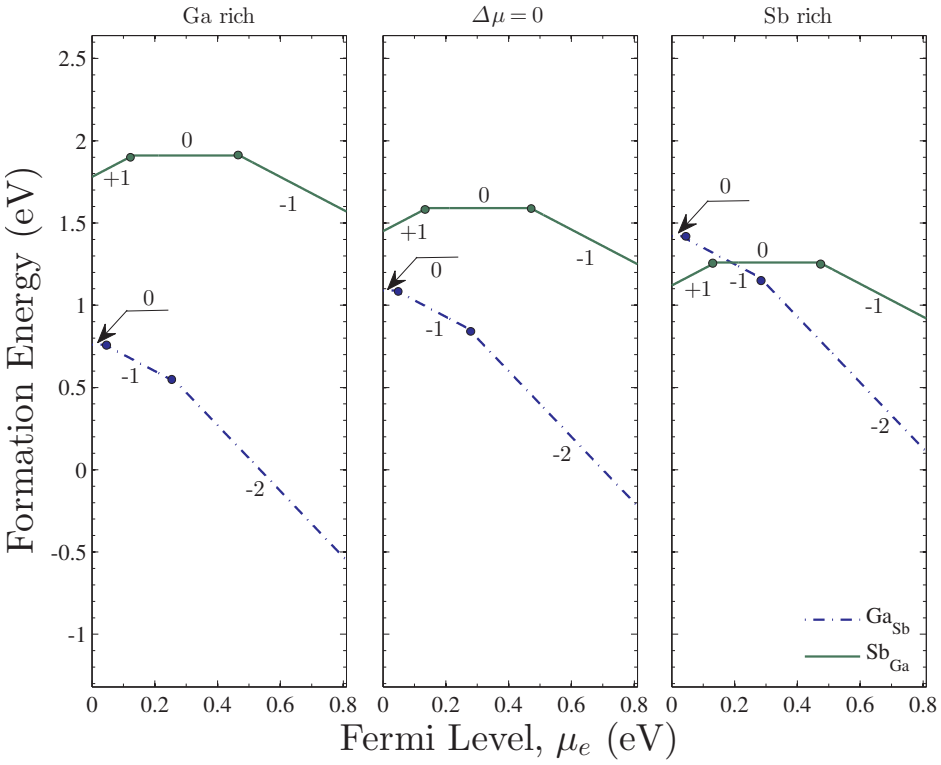

Figure 10.6.: Lowest antisite formation energies for Ga^q_{Sb} and Sb^q_{Ga} in GaSb assuming the most stable charge state (neutral or charged) as a function of the Fermi level.

10.3.3. Indium-$\mathbb{V}$ Compounds

10.3.3.1. Indium Phosphide

For InP under stoichiometric conditions, the two antisites In^q_P and P^q_{In} can form in turn depending on the Fermi level. From the VBM up to $\mu_e = 1.14$ eV P^q_{In} is the low energy defect and can exist in +2, +1 and the neutral charge states. For P^0_{In} the calculated formation energy is 2.20 eV which is in very good agreement with the calculated value of 2.28 eV by Castleton and Mirbt [222] and agrees very well with values obtained by Mishra *et al.* [236]. This agreement extends to In^0_P for which the formation energy of 2.67 eV is within 0.02 eV and 0.01 eV from the result in Ref. [222] and Ref. [236], respectively.

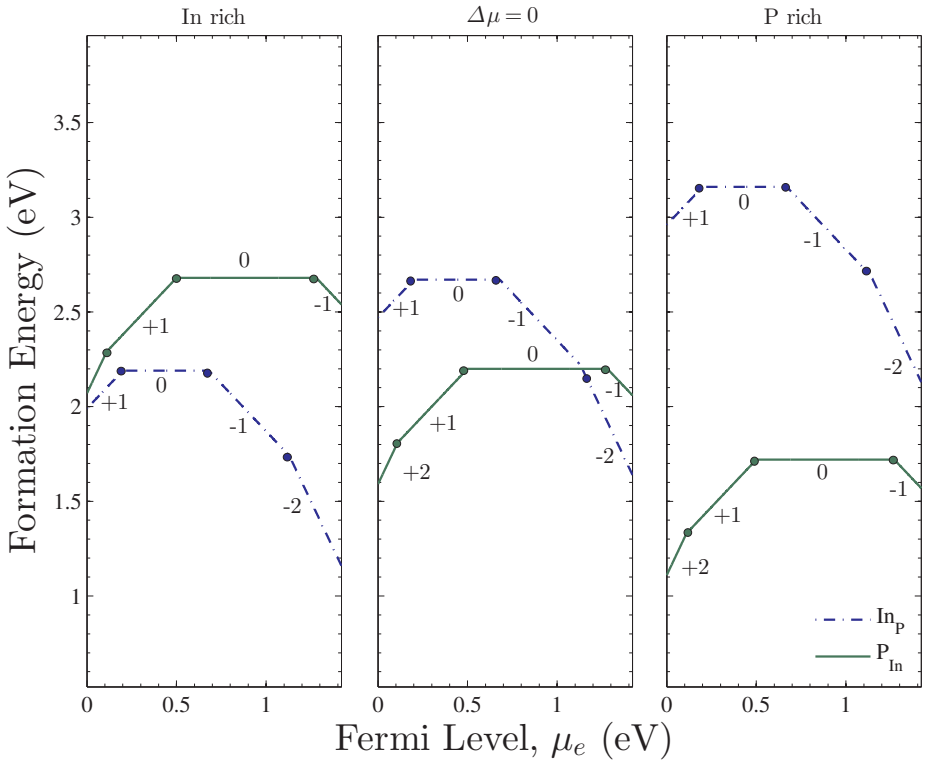

Figure 10.7.: Lowest antisite formation energies for In_P^q and P_{In}^q in InP assuming the most stable charge state (neutral or charged) as a function of the Fermi level.

Under In-rich conditions, a brief competition can occur between In_P^{+1} and P_{In}^{+2} as the difference in their formation energies is only 0.08 eV at the VBM. However, this difference grows rapidly as P_{In}^{+1} keeps rising in energy with the Fermi level whereas In_P^q transits to the neutral state followed by the -1 and -2 charge states. This leads to the difference in formation energies reaching 1.40 eV at the CBM prohibiting the formation of P_{In}^{-1}.

The situation is reversed dramatically under P-rich conditions. Here P_{In}^q will be favoured throughout the band gap starting from the VBM where In_P^{+1} has a high formation energy of 2.96 eV compared to 1.11 eV for P_{In}^{+2}.

10.3.3.2. Indium Arsenide

As can be seen from Fig. 10.8 antisites in InAS are dominantly charge neutral. The low energy defect under stoichiometric conditions is As^{q}_{In}. As^{+1}_{In} exists under p-doping conditions before making a transition to the neutral charge state at $\mu_e = 0.10$ eV. In^{q}_{As} is predicted to be less favourable due to its high formation energy relative to As^{q}_{In} [$E^f(As^0_{In}) - E^f(In^0_{As})$=0.64 eV].

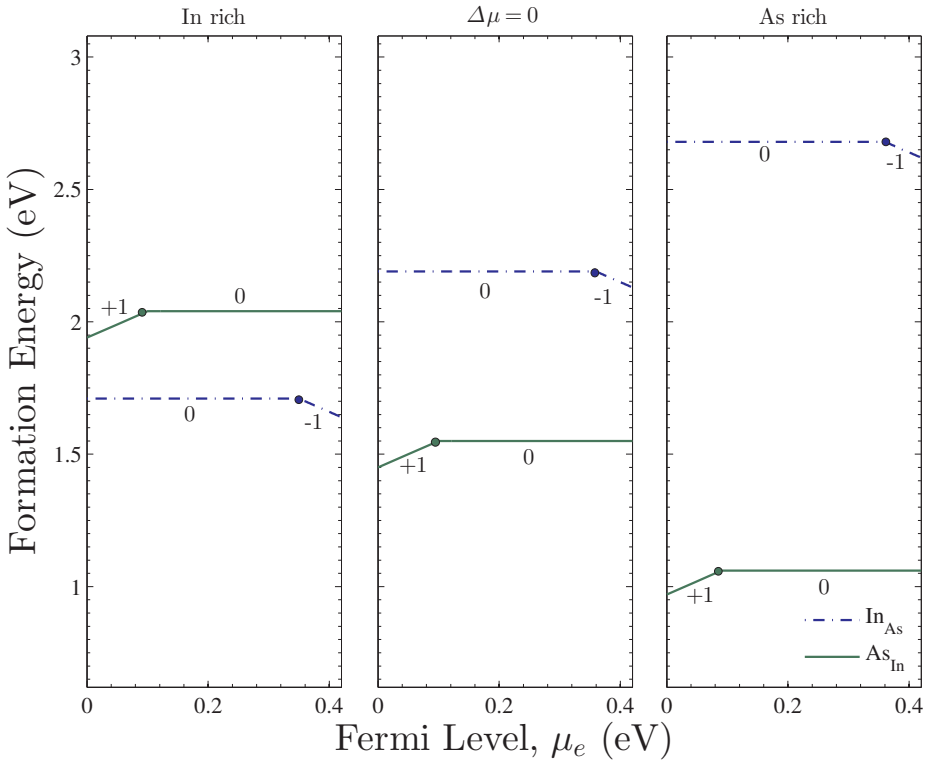

Figure 10.8.: Lowest antisite formation energies for In^{q}_{As} and As^{q}_{In} in InAs assuming the most stable charge state (neutral or charged) as a function of the Fermi level.

Under In-rich conditions, In^{q}_{As} will generally exhibit higher concentration than their As counterparts. The reverse is true under As-rich conditions.

10.3.3.3. Indium Antimonide

Similar to InAs, the small band gap forbids the formation of many charged defects in InSb. Again, we see here only the neutral and -1 charge states for $\mathrm{In}_{\mathrm{Sb}}^{q}$ and the $+1$ and neutral charge states for $\mathrm{Sb}_{\mathrm{In}}^{q}$. The only two transitions that are predicted from these calculations are $\epsilon(0/-) = 0.11$ eV and $\epsilon(+1/0) = 0.09$ eV for $\mathrm{In}_{\mathrm{Sb}}^{q}$ and $\mathrm{Sb}_{\mathrm{In}}^{q}$ respectively.

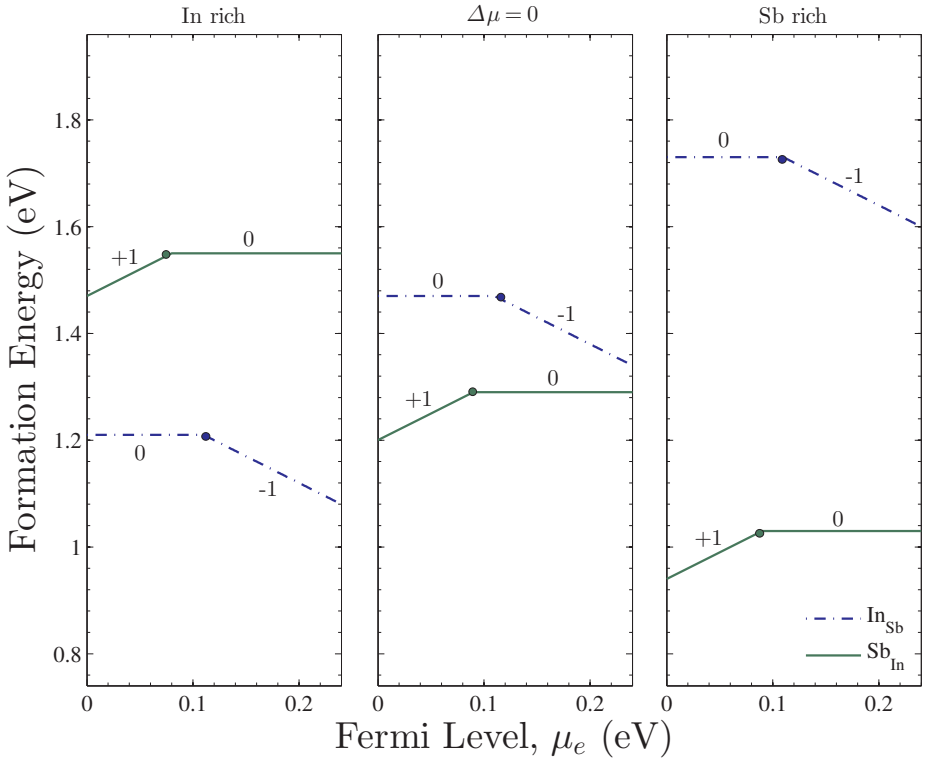

Figure 10.9.: Lowest antisite formation energies for $\mathrm{In}_{\mathrm{Sb}}^{q}$ and $\mathrm{Sb}_{\mathrm{In}}^{q}$ in InSb assuming the most stable charge state (neutral or charged) as a function of the Fermi level.

Stoichiometric conditions are in favour of the formation of $\mathrm{Sb}_{\mathrm{In}}^{q}$ as shown in Fig. 10.9; it is worth noting, however, that regardless of the value of the Fermi level, the difference in formation energies between the two antisite defects is not as large as the differences between other antistes. At the VBM $E^f(\mathrm{In}_{\mathrm{Sb}}^{0}) - E^f(\mathrm{Sb}_{\mathrm{In}}^{+1})$=0.27 eV and at the CBM $E^f(\mathrm{In}_{\mathrm{Sb}}^{-1}) - E^f(\mathrm{Sb}_{\mathrm{In}}^{0})$=0.098 eV indicating a

high competition between these two defects.

Changing the growth conditions towards In-rich will switch the preference to In^q_{Sb}, just as Sb-rich conditions will favour Sb^q_{In}.

10.3.4. Trends

The transition levels of all defects considered above are summarised in Table 10.1. The first noticeable feature is that only the phosphide anitsites (P^q_{Al}, P^q_{Ga} and P^q_{In}) possess a stable $+2$ charge states and that the transition to $+1$ occurs at Fermi levels that decrease down the group. The other feature is that, unlike III-V vacancies which can form in the -3 charge state, none of the antisites with the exception of Ga_{As} favour this charge state.

In general, group III antisites dominate under group III rich conditions while group V are dominant under group V conditions. There are a few exceptions when, under certain growth and doping conditions, the two antisites compete to form. This is the case for AlSb for which under stoichiometric conditions, Sb^q_{Al} dominates in the first half of the band gap and Al^q_{Sb} in the second. Under Al-rich conditions, the formation energy of Sb^q_{Al} is low enough for it to form under p-doping conditions before Al^q_{Sb} becomes lower in energy. Likewise, under Sb-rich conditions towards n-doping conditions Al^q_{Sb} becomes more favourable. This behaviour, in which the group III antisite becomes favourable under group V-rich conditions under n-doping conditions is shared by GaP and GaAs.

Overall, group V antisites are most likely to form under stoichiometric conditions. The only compound to favour group III antisites under stoichiometric conditions is GaSb.

The formation energies of antisites under stoichiometric conditions for Fermi levels in the middle of the band gap ($\mu_e = E_g/2$) (intrinsic doping conditions)

Table 10.1.: The transition levels (in eV above the VBM) of group III and group V antisites.

System	Defect	Transition				
		$\epsilon(+2/+1)$	$\epsilon(+1/0)$	$\epsilon(0/-)$	$\epsilon(-/=)$	$\epsilon(=/\equiv)$
AlP	Al_P	···	0.59	1.11	1.66	···
	P_{Al}	0.61	0.99	1.95	2.12	···
AlAs	Al_{As}	···	0.19	0.70	1.68	
	As_{Al}	···	0.46	1.85	···	
AlSb	Al_{Sb}	···	···	0.25	0.67	···
	Sb_{Al}	···	0.41	1.37	···	···
GaP	Ga_P	···	0.07	0.43	1.00	···
	P_{Ga}	0.48	0.58	1.84	2.25	···
GaAs	Ga_{As}	···	···	0.26	0.61	1.33
	As_{Ga}	···	0.19	1.08	1.39	···
GaSb	Ga_{Sb}	···	···	0.04	0.27	···
	Sb_{Ga}	···	0.13	0.47	···	···
InP	In_P	···	0.20	0.68	1.13	···
	P_{In}	0.11	0.50	1.28	···	···
InAs	In_{As}	···	···	0.35	···	···
	As_{In}	···	0.10	···	···	···
InSb	In_{Sb}	···	···	0.11	···	···
	Sb_{In}	···	0.08	···	···	···

are shown in Table 10.2. This shows a trend similar to the one established in Chapter 9, in which the formation energies of $\mathrm{III}_{\mathrm{V}}^{q}$ defects decrease as the covalent radius of the group V atom increases, while the formation energies of $\mathrm{V}_{\mathrm{V}}^{q}$ defects decrease as either the group III or V covalent radius increases.

Table 10.2.: The formation energies of the group Ⅲ and group Ⅴ antisites (in eV) for $\mu_e = \mathrm{E_g}/2$ under stoichiometric conditions ($\Delta\mu = 0$). The values in parenthesis correspond to the charge of the vacancy under intrinsic conditions.

	$\mathrm{Ⅲ}^q_{\mathrm{Ⅴ}}$		
	P	As	Sb
Al	4.33 (−1)	3.39 (−1)	1.82 (−2)
Ga	1.93 (−2)	1.57 (−2)	0.60 (−2)
In	2.64 (−1)	2.19 (−1)	1.46 (−1)
	$\mathrm{Ⅴ}^q_{\mathrm{Ⅲ}}$		
	P	As	Sb
Al	3.01 (0)	2.24 (0)	1.65 (0)
Ga	2.70 (0)	1.95 (0)	1.59 (0)
In	2.20 (0)	1.55 (0)	1.29 (0)

It can be noted from Table 10.2 that under stoichiometric growth and doping conditions $\mathrm{Ⅲ}^q_{\mathrm{Ⅴ}}$ defects exist in a -1 or -2 charge states. Ga-Ⅴ compounds favour the -2 charge state while In-Ⅴ compounds will favour the -1 charge state. The other remarkable feature is the prevalence of neutral charge for all group Ⅴ antisites. Furthermore, Table 10.2 indicates that under intrinsic conditions:

(a) The lowest energy antisites for Al-Ⅴ are the group Ⅴ antisites ($\mathrm{P}^0_{\mathrm{Al}}$, $\mathrm{As}^0_{\mathrm{Al}}$ and $\mathrm{Sb}^0_{\mathrm{Al}}$).

(b) The lowest energy antisites for Ga-Ⅴ are the group Ⅲ antisites ($\mathrm{Ga}^{-2}_{\mathrm{P}}$, $\mathrm{Ga}^{-2}_{\mathrm{As}}$ and $\mathrm{Ga}^{-2}_{\mathrm{Sb}}$).

(c) The lowest energy antisites for In-Ⅴ are the group Ⅴ antisites ($\mathrm{P}^0_{\mathrm{In}}$, $\mathrm{As}^0_{\mathrm{In}}$ and $\mathrm{Sb}^0_{\mathrm{In}}$).

To appreciate the importance of antisites in Ⅲ-Ⅴ semiconductors, it is useful to compare their formation energies with those of the vacancies obtained in Chapter 9. A comparison between Tables. 9.1 and 10.2 reveals that antisites are

Table 10.3.: The difference in formation energies $E^f(\text{vacancy}) - E^f(\text{antisite}) = \Delta E^f$ (in eV) between the favourable vacancies and antisites for each of the III-V compounds for $\mu_e = \mathrm{E_g}/2$ under stoichiometric conditions ($\Delta\mu = 0$).

	ΔE^f		
	P	As	Sb
Al	0.85	0.76	0.09
Ga	0.77	0.25	0.63
In	0.31	0.66	0.36

lower in energy for all of the compounds considered. The largest difference between antisite and vacancy formation energies occurs in AlP where the difference is $E^f(V_{\mathrm{P}}^{+1}) - E^f(\mathrm{P}_{\mathrm{Al}}^0) = 0.85$ eV and the least difference occurs in AlSb where $E^f(V_{\mathrm{Al}}^{-2}) - E^f(\mathrm{Sb}_{\mathrm{Al}}^0) = 0.09$ eV. The differences are summarised in Table 10.3.

Table 10.3 can be used to deduce the ratio of the antisite concentration to the vacancy concentration by using the relation:

$$c = N \exp(-E^f/k_B T) \tag{10.1}$$

where c is the concentration, N is the number of sites available, k_B is Boltzmann's constant and T the temperature. As mentioned in Sec. 1.3, the dependence of the calculated quantities in this work on temperature effects has been neglected. In general these effects become important at elevated temperatures and their magnitudes are defect dependent. The ratio of antisite concentration c_A to vacancy concentration c_V can then be expressed as:

$$c_A/c_V = \exp(\Delta E^f/kT) \tag{10.2}$$

where ΔE^f is the difference in formation energies between the favourable vacancies and antisites for each compound as given in Table 10.3. This implies

that concentrations of antisites can be orders of magnitudes higher than those of vacancies under strict intrinsic conditions. However, bearing in mind that vacancies in many of the III-V compounds (all except InAs and InSb) are stable in the -3 charge state (and thus strongly affected by the Fermi level) over a wide range of Fermi levels, changing the Fermi energy can readily change the relative concentrations of vacancies and antisites.

10.4. Conclusions

In this chapter, the formation energies of III-V antisites of different charges were investigated under various growth and doping conditions. It was found that under stoichiometric conditions and intrinsic doping conditions, antisite formation energies decrease with the covalent radii of the constituent atoms.

Under strict intrinsic conditions, antisites are always lower in energy compared to III-V vacancies. This is reversed under n-doping conditions as vacancies exist in the -3 charge state which easily attain low formation energies leading to higher concentrations. Understanding the effects of growth and doping on the relative stabilities of different point defects is of paramount importance when experimentally engineering the properties of these materials.

Work in this chapter appears in Tahini *et al.* Appl. Phys. Lett. **103**, 142107 (2013) [237].

11. Antisites and Anisotropic Diffusion in GaAs and GaSb

The significant diffusion of Ga under Ga-rich conditions in GaAs and GaSb is counter intuitive as the concentration of Ga vacancies should be depressed although Ga vacancies are necessary to interpret the experimental evidence for Ga transport. To reconcile the existence of Ga vacancies under Ga-rich conditions, transformation reactions have been proposed. In this chapter the formation energies of vacancies on both sublattices and the migration energy barriers to overcome the formation of the vacancy-antisite defects are calculated.

11.1. Introduction

Bracht *et al.* [219, 238] have determined that self-diffusion in GaSb is asymmetric with Ga diffusing more rapidly than Sb by over three orders of magnitude near the melting temperature. Furthermore, Ga self-diffusion is more significant than Sb even under Ga-rich conditions. Ga-diffusion is mainly vacancy-mediated in GaSb so one needs to understand the large disparity between the diffusion coefficients of Ga and Sb and the role of Ga vacancies (V_{Ga}) even under Ga-rich conditions.

Bracht and Brotzmann [239] explain the diffusion of Zn in GaAs via the kick-out mechanism that involves neutral and single positively charged self-interstitials. In addition, V_{Ga} contributes to Zn diffusion via the dissociative mechanism [239]. Zn diffusion in GaAs is effectively a probe to determine the individual contributions of charged Ga interstitials ($\mathrm{Ga_{int}}$) and V_{Ga} to the total Ga self-diffusion coefficient. Using Zn profiles from experiments on Zn diffusion under As-rich conditions, Bracht and Brotzmann [239] fitted the $\mathrm{Ga_{int}}$ and V_{Ga} contributions to Ga self-diffusion in GaAs, obtaining results consistent with the total self-diffusion coefficient. That is, the individual contributions are lower than the total Ga self-diffusion. However, the situation is very different under Ga-rich conditions. Although the same diffusion mechanisms (see Eqs. 2-4 of Ref. [239]) describe the experimental Zn profiles and even the Ga profiles, the individual contributions of neutral and positively charged V_{Ga} reduced to standard conditions (electronically intrinsic and to an As pressure of 1 atm), exceed the total Ga self-diffusion coefficient [238]. It is striking that the same model that works for As-rich conditions also accurately reproduces Zn profiles obtained under Ga-rich conditions. One counter intuitive idea that may nevertheless explain the situation is that significant concentrations of V_{Ga} exist and can evolve from V_{As} even under Ga-rich conditions. The same idea was used by Sunder *et al.* [240] to explain the abundance of V_{Ga} in GaSb under Ga-rich conditions. Few theoretical works have

also investigated these transformation reactions in GaAs and GaSb. The work of Chroneos and Bracht [167] supports the point of view that V_{Ga} in GaSb is produced under Ga-rich conditions via a transformation reaction involving V_{Sb}. Hakala *et al.* [235] also investigated along this avenue and found that a transformation of V_{Sb} to $\mathrm{Ga_{Sb}}V_{\mathrm{Ga}}$ is exothermic while a transformation of V_{Ga} to $\mathrm{Sb_{Ga}}V_{\mathrm{Sb}}$ is endothermic, and thus argued that these reactions can provide an explanation for the observed highly asymmetric self-diffusion of Ga and Sb in GaSb but without neglecting the role $\mathrm{Ga_{int}}$.

Apart from the investigation of vacancies, the present study will also focus on the associations of antisite defects with vacancies. Using DFT, a detailed investigation of the point defects is presented under different compositional conditions (stoichiometric, Ga-rich and As/Sb-rich) and Fermi levels. To gain a complete understanding of the processes, the kinetics of the transformation reactions are also considered.

11.2. Methodology

The work presented here adopts the methodology used in Chapters 9 and 10 in terms of supercell size, Brillouin zone sampling and cutoff energy along with similar parameters controlling force and energy convergence criteria. Charged defect interactions are similarly accounted for using the technique due to Freysoldt *et al.* [8, 9].

11.3. Results and Discussions

It is important to consider how V_{Ga} are relevant in GaAs and GaSb. The zinc blende structure has two sublattices, with each sublattice being occupied, ideally, by atoms of one kind. The four nearest neighbour sites of every lattice site

lie on the other sublattice, whereas the second neighbour sites lie on the same sublattice. In the plane-passing mechanism proposed by Bockstedte and Scheffler [241] (for Ga diffusion in GaAs) a Ga atom at a second nearest neighbour position with respect to a V_{Ga} moves towards it leaving its own site vacant. Thus, the Ga atom moves towards the interstitial region along the diffusion plane that is perpendicular to the (110) plane (see also Fig. 3 in Ref. [241]). The advantage of the plane-passing mechanism is that it does not necessitate the formation of defect complexes (such as $V_{\mathrm{Sb}}V_{\mathrm{Ga}}$ in the triple-defect mechanism [242]) or the creation of antisite disorder (such as in the ten-jump process [243]). This is because Ga self-diffusion is taking place on the Ga-sublattice and As self-diffusion on the As sublattice. In recent DFT studies El-Mellouhi and Mousseau [244, 245] considered other possible mechanisms for Ga self-diffusion in GaAs but predicted that the plane passing mechanism is the most energetically favourable for V_{Ga}^{0} and V_{Ga}^{-1} (both with diffusion barriers of 1.7 eV) and also for V_{Ga}^{-2} (diffusion barrier 1.85 eV).

Results presented in Fig. 11.1 show that in GaSb, irrespective of the composition conditions (i.e Ga or Sb rich) or Fermi level, the isolated V_{Ga} defect has a lower formation energy than the antimony vacancy (V_{Sb}). Fig. 11.2 shows that for GaAs the V_{As} is more favourable than the V_{Ga} for some p-type conditions in stoichiometric and Ga-rich compositions; it is never more favourable in As-rich compositions.

Bracht *et al.* [219] have proposed the transformation reaction $V_{\mathrm{As}} \rightarrow V_{\mathrm{Ga}} + \mathrm{Ga}_{\mathrm{As}}$ as a way to produce V_{Ga} from V_{As} in GaAs under Ga-rich conditions. Although the transformation does not change the formation energy of V_{Ga}, which relates to the unbound species concentration, it does introduce a population of $\mathrm{Ga}_{\mathrm{As}}V_{\mathrm{Ga}}$. In essence, Bracht *et al.* [219] considered the formation of two isolated species; however, as an intermediate process the vacancy-antisite pair is formed. Formally, the dissociation energy required to break up the pair defect also needs

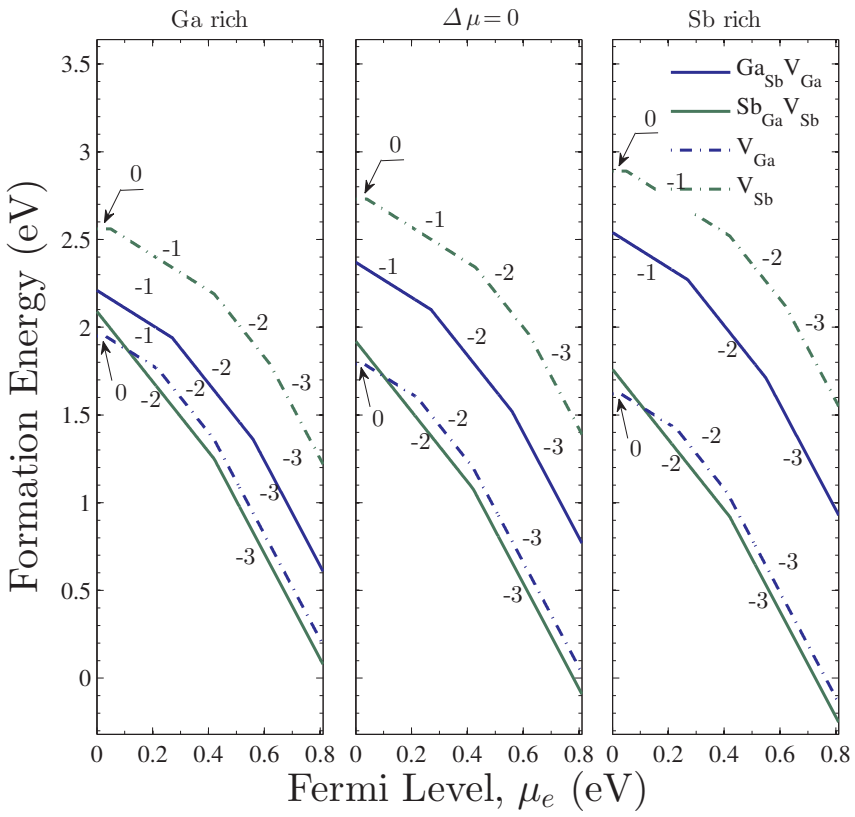

Figure 11.1.: Lowest energy vacancy and antisite-vacancy pair formation energies assuming the most stable charge state as a function of the Fermi level for stoichiometric, Ga-rich and Sb-rich conditions for GaSb.

to be calculated to gain a full understanding of the defect processes. This will involve the V_{Ga} migrating away from the pair via the plane-passing mechanism [241], effectively with a Ga atom at a second nearest neighbour position (with respect to a V_{Ga}) moving towards it, leaving its own site vacant. Here we assume that under experimental conditions all the vacancies will contribute to diffusion at their sublattice. For such conditions the calculations, illustrated in Fig. 11.2, reveal that it is energetically favourable to form isolated vacancies. In addition, a transformation reaction to form antisite-vacancy pairs for both materials is calculated to assess the impact on the V_{Ga} concentration, as was proposed experimentally. Figs. 11.1 and 11.2 report the antisite-vacancy pair formation

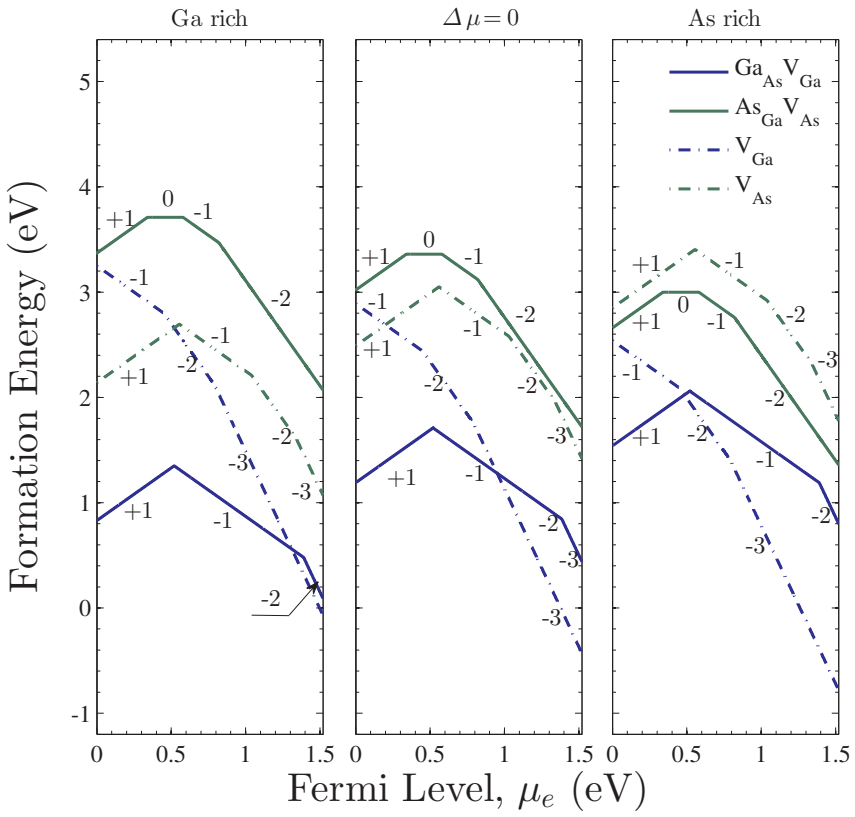

Figure 11.2.: Lowest energy vacancy and antisite-vacancy pair formation energies assuming the most stable charge state as a function of the Fermi level for stoichiometric, Ga-rich and As-rich conditions for GaAs.

energies for the most stable charge states as a function of the Fermi level for stoichiometric, III-rich and V-rich conditions in both GaSb and GaAs. The most stable cluster configuration is predominantly the nearest neighbour $Ga_{As}V_{Ga}$ in GaAs and $Sb_{Ga}V_{Sb}$ in GaSb regardless of composition. Considering first GaSb under Ga-rich conditions, the $Ga_{Sb}V_{Ga}$ cluster has a low formation energy under n-type conditions supporting the transformation reaction $V_{Sb} \rightarrow V_{Ga} + Ga_{Sb}$ that was previously proposed to explain the V_{Ga} mediated diffusion of Ga in GaSb under Ga-rich conditions [219]. Under such conditions one should expect that Ga_{int}, Ga_{Sb} and V_{Sb} are the favoured defects [219]. However, in their experiments under Ga-rich conditions, Bracht *et al.* observed no intermixing of the

Sb isotope structures even when V_{Sb} are supposed to be present. The present study supports the view that isolated V_{Ga} are produced even under Ga-rich conditions and are prevalent over V_{Sb} (Fig. 11.1). Again this is consistent with the experimental evidence of significantly higher Ga self-diffusion compared to Sb self-diffusion in GaSb. At any rate, the transformation reaction can add complementary V_{Ga} to the system.

In GaAs under Ga-rich conditions $\mathrm{Ga_{As}}V_{\mathrm{Ga}}$ have low formation energies especially for low Fermi levels where V_{As} have lower formation energies than V_{Ga} (see Fig. 11.2). Therefore, GaAs and GaSb are similar under Ga-rich conditions. Where the two materials differ is that under all conditions the $\mathrm{Sb_{Ga}}V_{\mathrm{Sb}}$ pair exhibits a lower formation energy than the V_{Ga}; the analogous pair in GaAs (i.e. the $\mathrm{As_{Ga}}V_{\mathrm{As}}$ pair) exhibits significantly higher formation energy under Ga rich conditions.

The lower formation energies of the $\mathrm{Sb_{Ga}}V_{\mathrm{Sb}}$ pair suggests that the transformation reaction $V_{\mathrm{Ga}} \rightarrow V_{\mathrm{Sb}} + \mathrm{Sb_{Ga}}$ would form V_{Sb} even under Sb-rich conditions, something that was not observed experimentally [219]. Hence to understand the absence of these thermodynamically favourable species, the kinetics of the transformation reactions are considered next by calculating the migration energies for these processes.

While the formation of V_{Ga} via transformation reactions can assist in achieving the V_{Ga} equilibrium concentration one has to consider the migration energy barrier that must be overcome to form the defect pair. A schematic representation of the transformation reaction $V_{\mathrm{As}} \rightarrow V_{\mathrm{Ga}} + \mathrm{Ga_{As}}$ in GaAs is provided at the top of Fig. 11.3(a). In essence a nearest neighbour Ga atom moves into the vacant As site. This leads to the formation of the Ga antisite and a vacant Ga site. Analogous mechanisms were also considered for $V_{\mathrm{Ga}} \rightarrow V_{\mathrm{As}} + \mathrm{As_{Ga}}$, $V_{\mathrm{Sb}} \rightarrow V_{\mathrm{Ga}} + \mathrm{Ga_{Sb}}$, and $V_{\mathrm{Ga}} \rightarrow V_{\mathrm{Sb}} + \mathrm{Sb_{Ga}}$ in Figs. 11.3(b), 11.4(a), and 11.4(b).

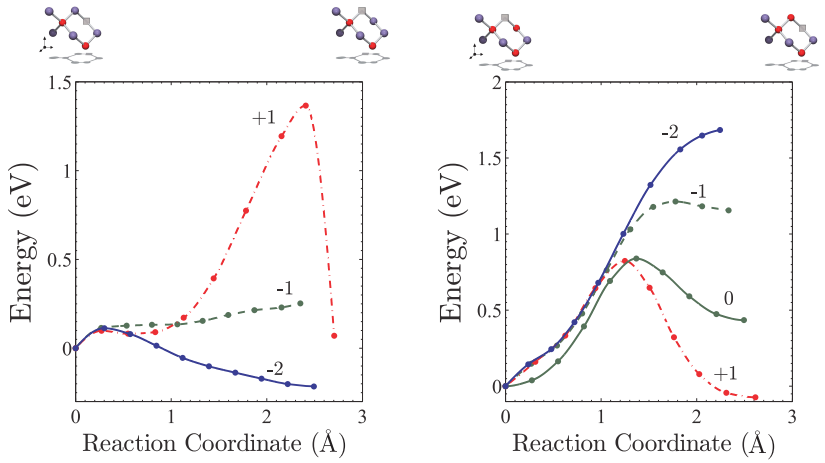

(a) (b)

Figure 11.3.: The migration energy barriers for (a) $V_{\mathrm{As}} \rightarrow V_{\mathrm{Ga}} + \mathrm{Ga}_{\mathrm{As}}$ and (b) $V_{\mathrm{Ga}} \rightarrow V_{\mathrm{As}} + \mathrm{As}_{\mathrm{Ga}}$ transformation reactions in GaAs. On the top of the figure is the initial and final state of the transformation reaction. Cubes represent the vacant site, red spheres the As atoms and purple spheres the Ga atoms. The reaction coordinates represent the distance between the images along the path of the diffusing species. Numbers in the figures represent the charge state of the respective defects.

Figs. 11.3 and 11.4 report the energies along the path defined on the top of the Figs. for GaAs and GaSb respectively. The charge states considered correspond to the dominant values of the vacancy-antisite pair identified in Figs. 11.1 and 11.2. It can be observed by comparing Figs. 11.3(a) and 11.3(b) and Figs. 11.4(a) and 11.4(b) that the lowest energy barriers, irrespective of the charge states, are for the production of V_{Ga} via the respective transformation reactions. For example, considering GaAs (see Fig. 11.3), the barrier to form doubly negatively charged $V_{\mathrm{As}} + \mathrm{As}_{\mathrm{Ga}}$ pairs (via $V_{\mathrm{Ga}} \rightarrow V_{\mathrm{As}} + \mathrm{As}_{\mathrm{Ga}}$, Fig. 11.3(a)) is more than 1.3 eV higher compared to the barrier to form the doubly negatively charged $V_{\mathrm{Ga}} + \mathrm{Ga}_{\mathrm{As}}$ pairs (via $V_{\mathrm{As}} \rightarrow V_{\mathrm{Ga}} + \mathrm{Ga}_{\mathrm{As}}$, Fig. 11.3(b)).

It is evident that the transformation reactions leading to the production of V_{Ga} are energetically favourable over the analogous reactions for all conditions in

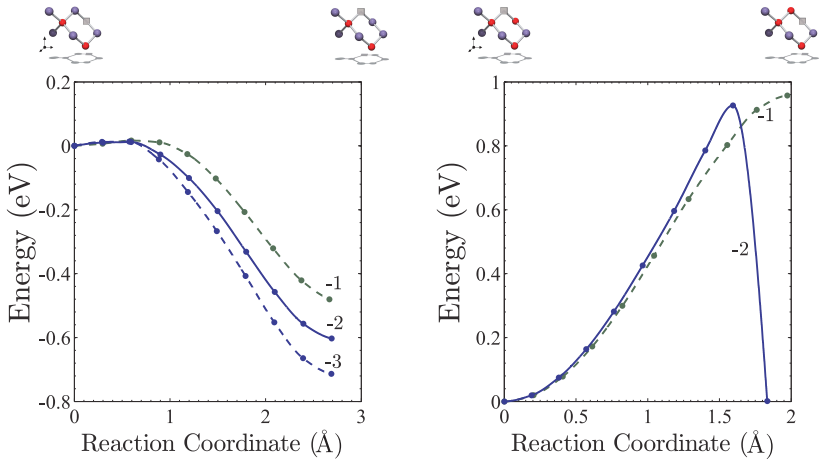

Figure 11.4.: The migration energy barriers for (a) $V_{\mathrm{Sb}} \rightarrow V_{\mathrm{Ga}} + \mathrm{Ga}_{\mathrm{Sb}}$ and (b) $V_{\mathrm{Ga}} \rightarrow V_{\mathrm{Sb}} + \mathrm{Sb}_{\mathrm{Ga}}$ transformation reactions in GaSb. On the top of the figure is the initial and final state of the transformation reaction.

both materials (Figs. 11.3 and 11.4). For GaSb this supports the model proposed by Bracht *et al.* [219], namely that under Ga-rich conditions transformation reactions ($V_{\mathrm{Sb}} \rightarrow V_{\mathrm{Ga}} + \mathrm{Ga}_{\mathrm{Sb}}$) lead to the formation of Ga vacancies (Fig. 11.4). At high Fermi levels the energy of this process is very low leading to the transformation of V_{Sb} to additional V_{Ga}. Conversely the process $V_{\mathrm{Ga}} \rightarrow V_{\mathrm{Sb}} + \mathrm{Sb}_{\mathrm{Ga}}$ in GaSb (which appears favourable at high Fermi energies in terms of formation energies in Fig. 11.1) is hindered by the high migration energy barriers (refer to Fig. 11.4(b)) which renders the equilibration rate to be very slow. The picture in GaAs is very similar, that is, the migration energy barriers for the production of V_{Ga} via the transformation reactions is lower compared to the production of the V_{As}.

11.4. Conclusions

The results of the present study lead to counterintuitive conclusions as it is predicted that the concentration of V_{Ga} or $\mathrm{Ga}_{\mathrm{As/Sb}}V_{\mathrm{Ga}}$ pairs is significant and dominant over group-$\mathbb{V}$ vacancies even under Ga-rich conditions for both GaSb and GaAs. They are consistent though with the experimentally observed diffusion behaviour in both materials. Transformation reactions under Ga-rich conditions can provide complementary V_{Ga} but these reactions are not necessary to explain the existence of V_{Ga} as they exhibit formation energies that are compatible with high Ga diffusion. The kinetics of the processes help explain the suppression of $V_{\mathrm{As/Sb}}$, as the migration energies indicate that the rate at which the equilibrium concentrations of these defects is attained is slow compared to the rates at which V_{Ga} are produced.

12. Conclusions and Outlook

"If I have seen further it is by standing on the shoulders of giants."

— Isaac Newton, physicist

12.1. Conclusions

As the quest for silicon alternatives continues, the aim of this thesis was to investigate some of the defect properties in interesting potential substitutes, namely Ge and III-V compounds. In this work, DFT was used with various functionals to study the formation and diffusion of point defects under different doping and growth conditions.

In Chapter 3 the perfect crystal properties of Ge and III-V materials were presented. For Ge, GGA alone does not predict the correct electronic structure. This was corrected using a $+U$ term, which is as reliable as HSE06 in reproducing the experimental band gap. The lattice, elastic, thermodynamic and electronic properties of III-V semiconductors were compared using GGA, GGA$+U$ and HSE06.

In Chapter 4 the effect of strain on the electronic structure of Ge was inves-

tigated. Here, both tensile and compressive strain were applied biaxially and uniaxially and in total six different planes and directions were considered. It was found that in general the application of strain converts Ge into a direct band gap material. The results were validated against known experimental data regarding the biaxial strain parallel to the (001) plane required to make the band gap of Ge direct. This is calculated to be 1.7% and agrees with the experimental result of 1.75% [110] providing confidence in the methodology used. Of particular interest was strain applied along the [111] direction that converted Ge into a direct band gap material at 1.05%.

Chapter 5 dealt with the interactions of n-dopants and tin with vacancies. The formation energies of PV_{Ge}, AsV_{Ge} and SbV_{Ge} clusters in different charge states were investigated as a function of the Fermi level. This was followed by an investigation of their diffusion in Ge. The activation energies of diffusion were found to be in very good agreement with experiments, exhibiting the same trend in which the activation energy decreased as the size of the n-dopant atom increased. The binding and formation energies of SnV_{Ge} pairs were calculated for various charges and Fermi levels. The migration energies of SnV_{Ge} pairs were also calculated. The analysis was extended further to study the effect of doping on the activation energies. The results were used successfully to explain the experimental observation of retarded diffusion (higher activation energy of migration) under p-doping conditions and enhanced diffusion (lower activation energy of migration) under n-doping conditions.

After establishing (Chapter 5) that n-dopants are fast diffusers in Ge, Chapters 6 and 7 were devoted to investigating strategies to retard the diffusion of P in particular. The key is to co-dope Ge with isovalent atoms such as Sn or Hf. These were shown to greatly increase the migration barriers and to form tightly bound clusters with P.

Chapter 8 focused on the interaction of Pd with Ge. Pd is an important metal

in the process of metal induced lateral crystallisation. Calculations reveal that Pd favours a split-vacancy configuration. Pd atoms occupying interstitial and substitutional sites have low formation energies indicating high stability. DOS calculations identified some low energy defects such as Pd^{0}_{Ge} or Pd^{-1}_{Ge} which are capable of interfering with the electronic structure of Ge. Pd is relatively mobile, with diffusion proceeding via a direct interstitial mechanism. The Frank-Turnbull and the kick-out mechanism are also feasible due to the very low migration and formation energies of Pd_{int} leading to a low activation energy.

A full understanding of intrinsic defects in III-V semiconductors will enable improved approaches to the fabrication of advanced ternary and quaternary materials for electronic and photovoltaic use. For this, vacancies and antisites were studied in Chapters 9 and 10 respectively for various growth conditions. Vacancy formation energies were found to decrease as the size of the group V atom increased. This trend was maintained for Al-V, Ga-V, and In-V compounds. It was also predicted that even under group III rich conditions, group III vacancies dominate in aluminium antimonide and gallium antimonide. For indium antimonide, group V vacancies are favoured even under group V rich conditions. Under stoichiometric and intrinsic doping conditions antisites are lower in energy than vacancies and hence, are expected to be present in higher concentrations. However, this is very sensitive to the doping levels as the formation energies of vacancies with high negative charges decrease as μ_e rises and approaches the CBM. Such vacancies therefore become favoured in the strongly n-doped regime.

Finally, in Chapter 11, self-diffusion in GaAs and GaSb was studied in an attempt to explain the disparity in the diffusion between Ga and As/Sb. It was found that the concentration of V_{Ga} or $\mathrm{Ga_{As}}V_{\mathrm{Ga}}$ pairs is significant and dominant over group V vacancies even under Ga-rich conditions for both GaSb and GaAs. This is consistent though, with the experimentally observed diffusion behaviour in

both materials. Transformation reactions under Ga-rich conditions can provide complementary V_{Ga} but these reactions are not necessary to explain the existence of V_{Ga} as they exhibit formation energies that are compatible with high Ga diffusion. The kinetics of the processes are, however, necessary to explain the suppression of V_{Sb} as the migration energies of the transformation reaction establish the dominance of the V_{Ga} over V_{As} or V_{Sb} for GaAs and GaSb.

12.2. Further Work

12.2.1. Re-evaluation

The reader will notice the use of an array of computational methods ranging from GGA to HSE06 functionals. This reflects the rapid evolution in this computational field over the course of a few years. By using the GGA+U exchange-correlation functional with a 64-atom supercell it was possible to avoid expensive HSE06 calculations. However, the small supercells demanded the use of finite size correction schemes, among which the Makov-Payne [60] approach was the most widely used at the beginning of this work. This was soon replaced by a more powerful and efficient method due to Freysoldt *et al.* [8, 9] which was numerically implemented and made available for users [246]. As the computational resources increased we were able to employ larger supercells with 216 or 512 atoms. Nevertheless, in order to use the more accurate HSE06 functional, a step backward was taken in terms of system sizes as the inclusion of a non-local exact exchange does not scale efficiently with plane wave basis sets making these calculations particularly demanding.

It would therefore be very beneficial to re-evaluate some of the results (for example Chapters 5, 9 and 10) with more advanced functionals and larger supercells in order to minimise the band gap and finite size errors, which will be a step

forward in harmonising and bringing these results to a common standard. However, it will not be long before new improved methods will emerge, demanding continuous assessment of prior results.

12.2.2. New Studies

The work presented here spans a wide range of semiconductors and some of their interactions with defects. The work presented in Chapter 4 thoroughly examined strain induced changes to the electronic structure of Ge along different planes and directions. The extension of this work to include binary III-V compounds will be beneficial to engineer the properties of these semiconductors, especially the indirect band gap compounds, AlP, AlAs, AlSb and GaP. For these, it would be useful to first make their relatively large band gaps direct by the application of strain, and then to tune the magnitude of the applied strain to achieve a wide range of band gaps, suitable to absorb a wider energy spectrum for applications in, for instance, photovoltaic devices.

Chapters 9 and 10 considered the formation of vacancies and antisites in III-V semiconductors and the effect of growth conditions and doping on these point defects. It is important to extend this to include self-interstitials in order to form a comprehensive survey of the interplay of point defects in these compounds, which will provide a road map for a better understanding of competing defects when fabricating real electronic devices.

Another area of great technological importance is semiconductors interface. There are a number of different interfaces and understanding impact of these on the electronic properties is correspondingly complex. It is important to be able to characterize the electronic properties of interfaces in layer semiconductors as dopants act to modify these base structures. GaInP/GaAs/Ge tandem cells could be studied and compared with available experimental work. A key feature would

be to establish the driving force for species segregation to the interface. That is, to test if it is likely that there is a change in concentration in composition towards such an interface. Of course, kinetics might play a critical role in the development of an interface structure, which is an avenue for further study. It would also be important to study the effect of inter-diffusion on the electronic properties of the interfaces.

The emergence of the revolutionary new material graphene [247, 248] has sparked interest in 2D semiconductors. Already research has investigated silicine [249] and germanene [250–252] (2D silicon and germanium sheets analogous to graphene). Work on 2D III-V semiconductors was initiated by Otsuji et al. [253] and Zhuang *et al.* [254]. Nevertheless, point defect studies are still lacking in these systems and hence, research into the doping and diffusion mechanisms and point defect induced changes in their electronic structure is uncharted territory.

In the thesis, most systems have been modelled with respect to single dopants. More generally dopants can be used to modify structural properties as well as electronic structures. Experimentally co-doping or even doping with three species is onerous because of the large parameter space: the dopant concentrations, the temperature, and the multiple charge states of multiple defects all need to be considered. This thesis has shown that using a general computational approach to identify interesting dopant combinations is feasible and could be very useful. Such an approach would be a valuable example of how modelling can lead experiment while still working very much in collaboration.

Bibliography

[1] W. M. Haynes, ed., *CRC Handbook of Chemistry and Physics* (CRC Press, 2012).

[2] S. Brotzmann and H. Bracht, J. Appl. Phys. **103**, 033508 (2008).

[3] J. P. Perdew and K. Schmidt, in *AIP Conference Proceedings* (2001), vol. 577, p. 1.

[4] D. Sheppard, R. Terrell, and G. Henkelman, J. Chem. Phys **128**, 134106 (2008).

[5] M. Aroyo, J. Perez-Mato, D. Orobengoa, E. Tasci, G. de la Flor, and A. Kirov, Bulg. Chem. Commun **43**, 183 (2011).

[6] *Images of elements* (2013), URL http://images-of-elements.com/.

[7] F. Frank and D. Turnbull, Phys. Rev. **104**, 617 (1956).

[8] C. Freysoldt, J. Neugebauer, and C. G. Van de Walle, Phys. Rev. Lett. **102**, 016402 (2009).

[9] C. Freysoldt, J. Neugebauer, and C. G. Van de Walle, Phys. Status Solidi B **248**, 1067 (2011).

[10] H. Iwai, in *Electron Devices Meeting, 2004. IEDM Technical Digest. IEEE International* (IEEE, 2004), pp. 11–16.

[11] T. Shinada, S. Okamoto, T. Kobayashi, and I. Ohdomari, Nature **437**, 1128 (2005).

[12] S. Sze, *Semiconductor Devices: Physics and Technology* (John Wiley & Sons Singapore Pte. Limited, 2013), ISBN 9780470873670.

[13] L. Kang, B. H. Lee, W.-J. Qi, Y. Jeon, R. Nieh, S. Gopalan, K. Onishi, and J. C. Lee, IEEE Electron Device Lett. **21**, 181 (2000).

[14] G. D. Wilk, R. M. Wallace, and J. Anthony, J. Appl. Phys. **89**, 5243 (2001).

[15] A. Chroneos, M. Rushton, and R. Grimes, in *Comprehensive Nuclear Materials*, edited by E. in Chief: Rudy J.M. Konings (Elsevier, Oxford, 2012), pp. 47 – 64, ISBN 978-0-08-056033-5.

[16] R. Tilley, *Defects in Solids*, Special Topics in Inorganic Chemistry (Wiley, 2008), ISBN 9780470380734.

[17] F. Kröger and H. Vink, Solid state physics **3**, 307 (1956).

[18] H. Mehrer, *Diffusion in Solids: Fundamentals, Methods, Materials, Diffusion-Controlled Processes*, Springer series in solid-state sciences (Springer-Verlag Berlin Heidelberg, 2007), ISBN 9783540714880.

[19] A. Walsh, J. Buckeridge, C. R. A. Catlow, A. J. Jackson, T. W. Keal, M. Miskufova, P. Sherwood, S. A. Shevlin, M. B. Watkins, S. M. Woodley, et al., Chem. Mat. (2013).

[20] J. Frenkel, Zeits. f. Physik **35**, 652 (1926).

[21] K. Sasaki and J. Maier, J. Appl. Phys. **86**, 5422 (1999).

[22] J. Orton, *The Story of Semiconductors* (OUP Oxford, 2004), ISBN 9780198530831.

[23] E. Conwell and V. F. Weisskopf, Phys. Rev. **77**, 388 (1950).

[24] O. D. Jurchescu, J. Baas, and T. T. M. Palstra, Appl. Phys. Lett. **84**, 3061 (2004).

[25] M. Youssef and B. Yildiz, Phys. Rev. B **86**, 144109 (2012).

[26] M. K. Aydinol, A. F. Kohan, G. Ceder, K. Cho, and J. Joannopoulos, Phys. Rev. B **56**, 1354 (1997).

[27] A. Kuwabara, Sci. Tech. Adv. Mater. **8**, 519 (2007).

[28] R. Martin, *Electronic Structure: Basic Theory and Practical Methods* (Cambridge University Press, 2004), ISBN 9780521782852.

[29] H. Hellmann, *Einführung in die Quantenchemie* (Franz Deuticke, 1937).

[30] R. P. Feynman, Phys. Rev. **56**, 340 (1939).

[31] P. Pulay, Molecular Physics **17**, 197 (1969).

[32] P. Hohenberg and W. Kohn, Phys. Rev. **136**, B864 (1964).

[33] W. Kohn and L. J. Sham, Phys. Rev. **140**, A1133 (1965).

[34] E. Kaxiras, *Atomic and Electronic Structure of Solids* (Cambridge University Press, 2003), ISBN 9780521523394.

[35] J. P. Perdew and W. Yue, Phys. Rev. B **33**, 8800 (1986).

[36] J. P. Perdew, J. A. Chevary, S. H. Vosko, K. A. Jackson, M. R. Pederson, D. J. Singh, and C. Fiolhais, Phys. Rev. B **46**, 6671 (1992).

[37] J. P. Perdew, K. Burke, and M. Ernzerhof, Phys. Rev. Lett. **77**, 3865 (1996).

[38] H. J. Monkhorst and J. D. Pack, Phys. Rev. B **13**, 5188 (1976).

[39] R. Pierret, *Advanced Semiconductor Fundamentals*, Modular Series on Solid State Devices, V. 6 (Prentice Hall./Pearson Education, 2003), ISBN 9780130617927.

[40] R. M. Nieminen, Modelling Simul. Mater. Sci. Eng. **17** (2009).

[41] V. E. Borisenko and S. Ossicini, *What is What in the Nanoworld* (Wiley, 2008).

[42] J. P. Perdew, M. Ernzerhof, and K. Burke, J. Chem. Phys **105**, 9982 (1996).

[43] J. Heyd, G. E. Scuseria, and M. Ernzerhof, J. Chem. Phys. **118**, 8207 (2003).

[44] J. Heyd, G. E. Scuseria, and M. Ernzerhof, J. Chem. Phys. **124**, 219906 (2006).

[45] T. Leininger, H. Stoll, H.-J. Werner, and A. Savin, Chem. Phys. Lett. **275**, 151 (1997).

[46] A. V. Krukau, O. A. Vydrov, A. F. Izmaylov, and G. E. Scuseria, J. Chem. Phys **125**, 224106 (2006).

[47] M. Fuchs, M. Bockstedte, E. Pehlke, and M. Scheffler, Phys. Rev. B **57**, 2134 (1998).

[48] P. Schwerdtfeger, ChemPhysChem **12**, 3143 (2011), ISSN 1439-7641.

[49] D. R. Hamann, M. Schlüter, and C. Chiang, Phys. Rev. Lett. **43**, 1494 (1979).

[50] N. Troullier and J. L. Martins, Phys. Rev. B **43**, 1993 (1991).

[51] C. L. Reis, J. M. Pacheco, and J. L. Martins, Phys. Rev. B **68**, 155111 (2003).

[52] D. Vanderbilt, Phys. Rev. B **41**, 7892 (1990).

[53] D. Singh and L. Nordstrom, *Planewaves, Pseudopotentials, and the LAPW Method* (Springer, 2006), ISBN 9780387287805.

[54] P. E. Blöchl, Phys. Rev. B **50**, 17953 (1994).

[55] G. Kresse and D. Joubert, Phys. Rev. B **59**, 1758 (1999).

[56] V. Brazdova and D. Bowler, *Atomistic Computer Simulations: A Practical Guide* (Wiley, 2013), ISBN 9783527671830.

[57] C. G. Van de Walle and J. Neugebauer, J. Appl. Phys. **95**, 3851 (2004).

[58] H.-P. Komsa, T. T. Rantala, and A. Pasquarello, Phys. Rev. B **86**, 45112 (2012).

[59] M. Leslie and J. Gillian, J. Phys. C: Solid State Phys. **18** (1985).

[60] G. Makov and M. C. Payne, Phys. Rev. B **51**, 4014 (1995).

[61] S. Lany and A. Zunger, Modell. Simul. Mater. Sci. Eng. **17**, 84002 (2009).

[62] N. D. M. Hine, K. Frensch, W. M. C. Foulkes, and M. W. Finnis, Phys. Rev. B **79**, 24112 (2009).

[63] G. Henkelman, G. Jóhannesson, and H. Jónsson, Theoretical Methods in Condensed Phase Chemistry pp. 269–302 (2002).

[64] H. Jónsson, G. Mills, and K. W. Jacobsen, *Nudged elastic band method for finding minimum energy paths of transitions* (385).

[65] G. Henkelman, B. P. Uberuaga, and H. Jónsson, J. Chem. Phys **113**, 9901 (2000).

[66] S. L. Dudarev, G. A. Botton, S. Y. Savrasov, C. J. Humphreys, and A. P. Sutton, Phys. Rev. B **57**, 1505 (1998).

[67] J. Paier, M. Marsman, K. Hummer, G. Kresse, I. C. Gerber, and J. G. Angyan, J. Chem. Phys. **124**, 154709 (2006).

[68] B. G. Janesko, T. M. Henderson, and G. E. Scuseria, Phys. Chem. Chem. Phys. **11**, 443 (2009).

[69] L. Schimka, J. Harl, and G. Kresse, J. Chem. Phys. **134**, 024116 (2011).

[70] S. Sze and K. Ng, *Physics of Semiconductor Devices* (Wiley, 2006), ISBN 9780470068304.

[71] H. P. Singh, Acta Crystallogr. A **24**, 469 (1968).

[72] A. Zaouk, E. Salvetat, J. Sakaya, F. Maury, and G. Constant, J. Cryst. Growth **55**, 135 (1981).

[73] M. Ludowise, J. Appl. Phys. **58**, R31 (1985).

[74] P. Petroff and S. DenBaars, Superlattices and Microstructures **15**, 15 (1994).

[75] A. Cho, Thin Solid Films **100**, 291 (1983).

[76] K. Cheng, Journal of Vacuum Science & Technology A: Vacuum, Surfaces, and Films **31**, 050814 (2013).

[77] S. Bedair, M. Tischler, T. Katsuyama, and N. El-Masry, Appl. Phys. Lett. **47**, 51 (1985).

[78] K. Burke, J. Chem. Phys **136**, 150901 (2012).

[79] S. Baroni, S. de Gironcoli, A. Dal Corso, and P. Giannozzi, Rev. Mod. Phys. **73**, 515 (2001).

[80] X. Wu, D. Vanderbilt, and D. Hamann, Phys. Rev. B **72**, 035105 (2005).

[81] Y. Le Page and P. Saxe, Phys. Rev. B **65**, 104104 (2002).

[82] J. Korvink and A. Greiner, *Semiconductors for Micro- and Nanotechnology: An Introduction for Engineers* (Wiley, 2002), ISBN 9783527302574.

[83] R. Tinder, *Tensor Properties of Solids: Phenomenological Development of the Tensor Properties of Crystals*, Synthesis lectures on engineering (Morgan & Claypool Publishers, 2008), ISBN 9781598293487.

[84] B. Delley, J. Phys. Chem. A **110**, 13632 (2006).

[85] A. Jain, G. Hautier, S. P. Ong, C. J. Moore, C. C. Fischer, K. A. Persson, and G. Ceder, Phys. Rev. B **84**, 045115 (2011).

[86] H. Tahini, A. Chroneos, R. W. Grimes, U. Schwingenschlögl, and A. Dimoulas, J. Phys.: Condens. Matter **24**, 195802 (2012).

[87] M. R. Bauer, J. Tolle, C. Bungay, A. V. Chizmeshya, D. J. Smith, J. Menéndez, and J. Kouvetakis, Solid State Communications **127**, 355 (2003), ISSN 0038-1098.

[88] M. Ieong, B. Doris, J. Kedzierski, K. Rim, and M. Yang, Science **306**, 2057 (2004).

[89] F. Ma, T.-W. Zhang, K.-W. Xu, and P. K. Chu, Appl. Phys. Lett. **98**, 191907 (2011).

[90] H. Yin, R. L. Peterson, K. D. Hobart, S. R. Shieh, T. S. Duffy, and J. C. Sturm, Appl. Phys. Lett. **87**, 061922 (2005).

[91] M. M. Rieger and P. Vogl, Phys. Rev. B **48**, 14276 (1993).

[92] D. D. Nolte, W. Walukiewicz, and E. E. Haller, Phys. Rev. Lett. **59**, 501 (1987).

[93] C. Tserbak and G. Theodorou, Phys. Rev. B **52**, 12232 (1995).

[94] Y. M. Niquet, D. Rideau, C. Tavernier, H. Jaouen, and X. Blase, Phys. Rev. B **79**, 245201 (2009).

[95] P. H. Lim, S. Park, Y. Ishikawa, and K. Wada, Opt. Express **17**, 16358 (2009).

[96] R. Camacho-Aguilera, Z. Han, Y. Cai, L. C. Kimerling, and J. Michel, Appl. Phys. Lett. **102**, 152106 (2013).

[97] L. Carroll, P. Friedli, S. Neuenschwander, H. Sigg, S. Cecchi, F. Isa, D. Chrastina, G. Isella, Y. Fedoryshyn, and J. Faist, Phys. Rev. Lett. **109**, 057402 (2012).

[98] M. Schmid, M. Oehme, M. Gollhofer, R. Körner, M. Kaschel, E. Kasper, and J. Schulze, Thin Solid Films (2013), ISSN 0040-6090, accepted Manuscript.

[99] M. E. Kurdi, H. Bertin, E. Martincic, M. de Kersauson, G. Fishman, S. Sauvage, A. Bosseboeuf, and P. Boucaud, Appl. Phys. Lett. **96**, 041909 (2010).

[100] F. Murphy-Armando and S. Fahy, J. Appl. Phys. **109**, 113703 (2011).

[101] G. Kresse and J. Furthmüller, Phys. Rev. B **54**, 11169 (1996).

[102] O. Madelung, *Semiconductors : data handbook* (Springer, Berlin ; New York, 2004).

[103] D. E. Aspnes, Phys. Rev. B **12**, 2297 (1975).

[104] Y. Maeda, Phys. Rev. B **51**, 1658 (1995).

[105] O. Madelung, W. von der Osten, and U. Rössler, *Intrinsic Properties of Group IV Elements and III-V, II-VI and I-VII Compounds / Intrinsische Eigenschaften Von Elementen Der IV. Gruppe und Von III-V-, II-VI- und I-VII-Verbindungen*, Landolt-Bornstein: New series (Springer, 1986), ISBN 9783540166092.

[106] C. G. Van de Walle and R. M. Martin, Phys. Rev. B **34**, 5621 (1986).

[107] J. Kim, Ph.D. thesis, University of Massachusetts Amherst (2011).

[108] U. Mishra and J. Singh, *Semiconductor Device Physics and Design* (Springer, 2007), ISBN 9781402064814.

[109] D. Ahn and S. Park, *Engineering Quantum Mechanics* (Wiley, 2011), ISBN 9781118017814.

[110] Y. Huo, Ph.D. thesis, Stanford University (2010).

[111] F. Zhang, V. H. Crespi, and P. Zhang, Phys. Rev. Lett. **102**, 156401 (2009).

[112] J. R. Sánchez-Pérez, C. Boztug, F. Chen, F. F. Sudradjat, D. M. Paskiewicz, R. Jacobson, M. G. Lagally, and R. Paiella, Proceedings of the National Academy of Sciences **108**, 18893 (2011).

[113] Y. Sun, S. E. Thompson, and T. Nishida, J. Appl. Phys. **101**, 104503 (2007).

[114] J. Halpern and B. Lax, J. Phys. Chem. Solids **26**, 911 (1965).

[115] R. L. Aggarwal, Phys. Rev. B **2**, 446 (1970).

[116] E. Paige, *The electrical Conductivity of germanium*, [Progress in Semiconductors. vol. 8.] (Heywood, 1964).

[117] H. Tahini, A. Chroneos, R. W. Grimes, U. Schwingenschlögl, and H. Bracht, Appl. Phys. Lett. **99**, 072112 (2011).

[118] H. Tahini, A. Chroneos, R. W. Grimes, and U. Schwingenschlögl, Appl. Phys. Lett. **99**, 162103 (2011).

[119] M. Naganawa, Y. Shimizu, M. Uematsu, K. M. Itoh, K. Sawano, Y. Shiraki, and E. E. Haller, Appl. Phys. Lett. **93**, 191905 (2008).

[120] A. Chroneos, R. W. Grimes, B. P. Uberuaga, and H. Bracht, Phys. Rev. B **77**, 235208 (2008).

[121] C. Janke, R. Jones, S. Öberg, and P. R. Briddon, Phys. Rev. B **77**, 195210 (2008).

[122] A. Chroneos, H. Bracht, R. W. Grimes, and B. P. Uberuaga, Appl. Phys. Lett. **92**, 172103 (2008).

[123] B. Uberuaga, G. Henkelman, H. JÃşnsson, S. Dunham, W. Windl, and R. Stumpf, physica status solidi (b) **233**, 24 (2002), ISSN 1521-3951.

[124] M. I. J. Probert and M. C. Payne, Phys. Rev. B **67**, 075204 (2003).

[125] A. Chroneos, J. Appl. Phys. **107**, 076102 (2010).

[126] S. Lany and A. Zunger, Phys. Rev. B **78**, 235104 (2008).

[127] J. Coutinho, R. Jones, V. J. B. Torres, M. Barroso, S. Oberg, and P. R. Briddon, J. Phys. Cond. Mat. **17** (2005).

[128] A. Janotti, R. Baierle, A. J. R. D. Silva, R. Mota, and A. Fazzio, Physica B **273** (1999).

[129] H. Haesslein, R. Sielemann, and C. Zistl, Phys. Rev. Lett. **80** (1998).

[130] A. Mesli, L. Dobaczewski, K. B. Nielsen, V. Kolkovsky, M. C. Petersen, and A. N. Larsen, Phys. Rev. B. **78** (2008).

[131] T. Südkamp, H. Bracht, G. Impellizzeri, J. L. Hansen, A. N. Larsen, and E. Haller, Appl. Phys. Lett. **102**, 242103 (2013).

[132] P. Spiewak, J. Vanhellemont, K. Sueoka, K. Kurzydłowski, and I. Romandic, J. Appl. Phys. **103**, 086103 (2008).

[133] J. R. Weber, A. Janotti, and C. G. Van de Walle, Phys. Rev. B **87**, 035203 (2013).

[134] R. Jones, A. Carvalho, J. Goss, and P. Briddon, Materials Science and Engineering: B **159**, 112 (2009).

[135] H. Höhler, N. Atodiresei, K. Schroeder, R. Zeller, and P. H. Dederichs, Phys. Rev. B **71**, 035212 (2005).

[136] S. Hu, physica status solidi (b) **60**, 595 (1973).

[137] M. Ono and T. Tezuka, Jpn. J. Appl. Phys. **49** (2010).

[138] S. Takeuchi, Y. Shimura, O. Nakatsuka, S. Zaima, M. Ogawa, and A. Sakai, Appl. Phys. Lett. **92**, 231916 (2008).

[139] Y. Shimura, N. Tsutsui, O. Nakatsuka, A. Sakai, and S. Zaima, Thin Solid Films **518**, S2 (2010).

[140] J. J. Pulikkotil, A. Chroneos, and U. Schwingenschlögl, J. Appl. Phys. **110**, 036105 (2011).

[141] R. Kube, H. Bracht, A. Chroneos, M. Posselt, and B. Schmidt, J. Appl. Phys. **106**, 063534 (2009).

[142] G. Impellizzeri, S. Boninelli, F. Priolo, E. Napolitani, C. Spinella, A. Chroneos, and H. Bracht, J. Appl. Phys. **109**, 113527 (2011).

[143] G. Weyer, A. Nylandsted-Larsen, B. Deutch, J. Andersen, and E. Antoncik, Hyperfine Interactions **1**, 93 (1975).

[144] A. Chroneos, physica status solidi (b) **244**, 3206 (2007).

[145] V. Markevich, A. Peaker, B. Hamilton, V. Litvinov, Y. M. Pokotilo, S. Lastovskii, J. Coutinho, A. Carvalho, M. Rayson, and P. Briddon, J. Appl. Phys. **109**, 083705 (2011).

[146] J. Bernholc, A. Antonelli, T. M. Del Sole, Y. Bar-Yam, and S. T. Pantelides, Phys. Rev. Lett. **61**, 2689 (1988).

[147] H. M. Branz, R. Reedy, R. S. Crandall, H. Mahan, Y. Xu, and B. P. Nelson, Journal of non-crystalline solids **299**, 191 (2002).

[148] N. Nickel, Microelectronic. Reliab. **47**, 899 (2007).

[149] G. Vogel, G. Hettich, and H. Mehrer, J. Phys. C **16**, 6197 (1983).

[150] M. Werner, H. Mehrer, and H. Hochheimer, Phys. Rev. B **32**, 3930 (1985).

[151] P. Kringhoj and R. G. Elliman, Appl. Phys. Lett. **65**, 324 (1994).

[152] M. Friesel, U. Sodervall, and W. Gust, J. Appl. Phys. **78**, 5351 (1995).

[153] I. Riihimaki, A. Virtanen, S. Rinta-Anttila, P. Pusa, J. Raisanen, et al., Appl. Phys. Lett. **91**, 091922 (2007).

[154] D. Shaw, physica status solidi (b) **72**, 11 (1975).

[155] H. A. Tahini, A. Chroneos, R. W. Grimes, U. Schwingenschlögl, and H. Bracht, Phys. Chem. Chem. Phys. **15**, 367 (2013).

[156] C. Claeys and E. Simoen, *Germanium-Based Technologies: From Materials to Devices* (Elsevier Science, 2011), ISBN 9780080474908.

[157] E. Napolitani, G. Bisognin, E. Bruno, M. Mastromatteo, G. Scapellato, S. Boninelli, D. De Salvador, S. Mirabella, C. Spinella, A. Carnera, et al., Appl. Phys. Lett. **96**, 201906 (2010).

[158] J. Kim, S. W. Bedell, and D. K. Sadana, Appl. Phys. Lett. **98**, 082112 (2011).

[159] A. Chroneos, R. Grimes, and H. Bracht, J. Appl. Phys. **106**, 063707 (2009).

[160] A. Chroneos, C. Jiang, R. W. Grimes, U. Schwingenschlögl, and H. Bracht, Appl. Phys. Lett. **94**, 252104 (2009).

[161] A. Chroneos, C. Londos, E. Sgourou, and P. Pochet, Appl. Phys. Lett. **99**, 241901 (2011).

[162] A. Chroneos and A. Dimoulas, J. Appl. Phys. **111**, 023714 (2012).

[163] M. Marsman, J. Paier, A. Stroppa, and G. Kresse, J. Phys.: Condens. Matter **20**, 064201 (2008).

[164] H. A. Tahini, A. Chroneos, R. W. Grimes, and U. Schwingenschlögl, J. Appl. Phys. **113**, 073704 (2013).

[165] E. Bruno, G. Scapellato, A. La Magna, M. Cuscuna, E. Napolitani, S. Boninelli, F. Priolo, G. Fortunato, and V. Privitera, Appl. Phys. Lett. **101**, 172110 (2012).

[166] P. Tsouroutas, D. Tsoukalas, and H. Bracht, J. Appl. Phys. **108**, 024903 (2010).

[167] A. Chroneos and H. Bracht, J. Appl. Phys. **104**, 093714 (2008).

[168] S. Brotzmann, H. Bracht, J. L. Hansen, A. N. Larsen, E. Simoen, E. E. Haller, J. S. Christensen, and P. Werner, Phys. Rev. B **77**, 235207 (2008).

[169] S. Solmi and D. Nobili, J. Appl. Phys. **83**, 2484 (1998).

[170] J. Xie and S. Chen, J. Phys.: Condens. Matter **11**, 7219 (1999).

[171] V. Ranki and K. Saarinen, Physica B: Condensed Matter **340**, 765 (2003).

[172] S. Schneider, H. Bracht, J. N. Klug, J. L. Hansen, A. N. Larsen, D. Bougeard, and E. E. Haller, Phys. Rev. B **87**, 115202 (2013).

[173] J.-H. Park, M. Tada, P. Kapur, H. Peng, and K. C. Saraswat, J. Appl. Phys. **104**, 064501 (2008).

[174] S. Herd, P. Chaudhari, and M. Brodsky, J. Non-Cryst. Solids **7**, 309 (1972), ISSN 0022-3093.

[175] Z. Jin, G. A. Bhat, M. Yeung, H. S. Kwok, and M. Wong, J. Appl. Phys. **84**, 194 (1998).

[176] M. Miyasaka, K. Makihira, T. Asano, E. Polychroniadis, and J. Stoemenos, Appl. Phys. Lett. **80**, 944 (2002).

[177] R. Xie, T. H. Phung, M. Yu, S. A. Oh, S. Tripathy, and C. Zhu, Electrochem. Solid-State Lett. **12**, H266 (2009).

[178] T. H. Phung and C. Zhu, J. Electrochem. Soc. **157**, H755 (2010).

[179] Z. Chen, S. Zhang, S. Tan, and Z. Wu, Mater. Sci. Eng. A **373**, 21 (2004), ISSN 0921-5093.

[180] H. Timmers, W. Kemp, A. Byrne, M. Ridgway, R. Vianden, P. Kessler, and M. Steffens, Hyperfine Interact. **197**, 159 (2010).

[181] A. Abiona, W. Kemp, and H. Timmers, Hyperfine Interact. pp. 1–8 (2012).

[182] M. Beck, M. Ellner, and E. J. Mittemeijer, in *Materials Science Forum* (Trans Tech Publ, 2000), vol. 321, pp. 604–609.

[183] W. Chen, C. Tegenkamp, H. PfnÃijr, and T. Bredow, Phys. Rev. B **82**, 104106 (2010).

[184] H. A. Tahini, A. Chroneos, S. T. Murphy, U. Schwingenschlögl, and R. W. Grimes, J. Appl. Phys. **114**, 063517 (2013).

[185] B. Cordero, V. Gomez, A. E. Platero-Prats, M. Reves, J. Echeverria, E. Cremades, F. Barragan, and S. Alvarez, Dalton Trans. pp. 2832–2838 (2008).

[186] S. Kasamatsu, T. Tada, and S. Watanabe, Solid State Ionics **183**, 20 (2011).

[187] H. Bracht, Materials science in semiconductor processing **7**, 113 (2004).

[188] H. Bracht, N. Stolwijk, and H. Mehrer, Phys. Rev. B **43**, 14465 (1991).

[189] R. Szweda, *Gallium Arsenide, Electronics Materials and Devices. A Strategic Study of Markets, Technologies and Companies Worldwide 1999-2004* (Elsevier Science, 2000).

[190] J. S. Blakemore, J. Appl. Phys. **53**, R123 (1982).

[191] P. S. Dutta, H. L. Bhat, and V. Kumar, J. Appl. Phys. **81**, 5821 (1997).

[192] *The international technology roadmap for semiconductors*, http://www.itrs.net/ (accessed 2013).

[193] J. A. del Alamo, Nature **479**, 317 (2011).

[194] S. Adachi, *Physical Properties of III-V Semiconductor Compounds*, Wiley-Interscience publication (Wiley, 1992).

[195] D. N. Talwar and C. S. Ting, Phys. Rev. B **25**, 2660 (1982).

[196] J. Hafner, J. Comput. Chem. **29**, 2044 (2008).

[197] R. Ramprasad, H. Zhu, P. Rinke, and M. Scheffler, Phys. Rev. Lett. **108**, 066404 (2012).

[198] S. B. Zhang and J. E. Northrup, Phys. Rev. Lett. **67**, 2339 (1991).

[199] F. El-Mellouhi and N. Mousseau, Phys. Rev. B **71**, 125207 (2005).

[200] H.-P. Komsa and A. Pasquarello, Microelectron. Eng. **88**, 1436 (2011).

[201] T. Shimazaki and Y. Asai, J. Chem. Phys. **132**, 224105 (2010).

[202] Z. Y. Jiao, S. H. Ma, and Y. L. Guo, Comp. Theor. Chem. **970**, 79 (2011).

[203] L. Torpo, M. Marlo, T. E. M. Staab, and R. M. Nieminen, J. Phys.: Condens. Matter **13**, 6203 (2001).

[204] K. Seeger and E. Schonherr, Semicond. Sci. Technol. **6**, 301 (1991).

[205] D. Åberg, P. Erhart, A. J. Williamson, and V. Lordi, Phys. Rev. B **77**, 165206 (2008).

[206] M.-H. Du, Phys. Rev. B **79**, 45207 (2009).

[207] A. S. Jordan, A. R. Von Neida, R. Caruso, and C. K. Kim, J. Electrochem. Soc. **121**, 153 (1974).

[208] A. Fazzio, L. M. Brescansin, and J. R. Leite, J. Phys. C: Solid State Phys **15**, L1 (1982).

[209] L. Wang, J. A. Wolk, L. Hsu, E. E. Haller, J. W. Erickson, M. Cardona, T. Ruf, J. P. Silveira, and F. Briones, Appl. Phys. Lett. **70**, 1831 (1997).

[210] A. Höglund, C. W. M. Castleton, and S. Mirbt, Phys. Rev. B **72**, 195213 (2005).

[211] S. Y. Chiang and G. L. Pearson, J. Appl. Phys. **46**, 2986 (1975).

[212] D. M. Taylor, D. O. Wilson, and D. H. Phillips, Solid-State and Electron Devices, IEE Proceedings I **127**, 266 (1980).

[213] K. Hjort, J. Soderkvist, and J. A. Schweitz, J. Micromech. Microeng **4**, 1 (1994).

[214] J. T. Schick, C. G. Morgan, and P. Papoulias, Phys. Rev. B **66**, 195302 (2002).

[215] P. A. Schultz and O. A. von Lilienfeld, Modell. Simul. Mater. Sci. Eng. **17**, 84007 (2009).

[216] B.-H. Cheong and K. J. Chang, Phys. Rev. B **49**, 17436 (1994).

[217] S. Pöykkö, M. J. Puska, and R. M. Nieminen, Phys. Rev. B **53**, 3813 (1996).

[218] S. T. Murphy, A. Chroneos, R. W. Grimes, C. Jiang, and U. Schwingenschlögl, Phys. Rev. B **84**, 184108 (2011).

[219] H. Bracht, S. P. Nicols, W. Walukiewicz, J. P. Silveira, F. Briones, and E. E. Haller, Nature **408**, 69 (2000).

[220] A. Katz, *Indium phosphide and related materials: processing, technology, and devices*, Artech House Materials Library (Artech House, 1992).

[221] C. W. M. Castleton and S. Mirbt, Physica B: Condensed Matter **340**, 407 (2003).

[222] C. W. M. Castleton and S. Mirbt, Phys. Rev. B **70**, 195202 (2004).

[223] W. LiMing, S. Fung, C. D. Beling, M. Fuchs, and A. P. Seitsonen, J. Phys.: Condens. Matter **10**, 9263 (1998).

[224] D. G. Avery, D. W. Goodwin, and M. A. E. Rennie, J. Sci. Instrum. **34**, 394 (1957).

[225] J. E. Northrup and S. B. Zhang, Phys. Rev. B **50**, 4962 (1994).

[226] V. Virkkala, V. Havu, F. Tuomisto, and M. J. Puska, Phys. Rev. B **86**, 144101 (2012).

[227] A. Höglund, C. W. M. Castleton, M. Göthelid, B. Johansson, and S. Mirbt, Phys. Rev. B **74**, 75332 (2006).

[228] W. Pötz and D. K. Ferry, Phys. Rev. B **29**, 5687 (1984).

[229] W. Pötz and D. K. Ferry, Phys. Rev. B **31**, 968 (1985).

[230] M. Levinson, Phys. Rev. B **28**, 3660 (1983).

[231] D. J. Chadi and K. J. Chang, Phys. Rev. Lett. **60**, 2187 (1988).

[232] J. Dabrowski and M. Scheffler, Phys. Rev. B **40**, 10391 (1989).

[233] J. Lagowski, D. Lin, T.-P. Chen, M. Skowronski, and H. Gatos, Appl. Phys. Lett. **47**, 929 (1985).

[234] H.-P. Komsa and A. Pasquarello, Physical Review B **84**, 075207 (2011).

[235] M. Hakala, M. Puska, and R. Nieminen, J. Appl. Phys. **91**, 4988 (2002).

[236] R. Mishra, O. Restrepo, A. Kumar, and W. Windl, J. Mater. Sci. **47**, 7482 (2012).

[237] H. A. Tahini, A. Chroneos, H. Bracht, S. T. Murphy, R. W. Grimes, and U. Schwingenschlogl, Appl. Phys. Lett. **103**, 142107 (2013).

[238] H. Bracht, S. P. Nicols, E. E. Haller, J. P. Silveira, and F. Briones, J. Appl. Phys. **89**, 5393 (2001).

[239] H. Bracht and S. Brotzmann, Phys. Rev. B **71**, 115216 (2005).

[240] K. Sunder, H. Bracht, S. P. Nicols, and E. E. Haller, Phys. Rev. B **75**, 245210 (2007).

[241] M. Bockstedte and M. Scheffler, arXiv preprint cond-mat/9612026 (1996).

[242] D. Wbiler and H. Mehrer, Philos. Mag. A **49**, 309 (1984).

[243] J. Van Vechten, J. Phys. C **17**, L933 (1984).

[244] F. El-Mellouhi and N. Mousseau, Phys. Rev. B **74**, 205207 (2006).

[245] F. El-Mellouhi and N. Mousseau, Physica B: Condensed Matter **401**, 658 (2007).

[246] C. Freysoldt, *Manual for sxdefectalign* (2011).

[247] K. S. Novoselov, A. K. Geim, S. Morozov, D. Jiang, Y. Zhang, S. Dubonos, I. Grigorieva, and A. Firsov, Science **306**, 666 (2004).

[248] A. K. Geim and K. S. Novoselov, Nature Mater. **6**, 183 (2007).

[249] P. Vogt, P. De Padova, C. Quaresima, J. Avila, E. Frantzeskakis, M. C. Asensio, A. Resta, B. Ealet, and G. Le Lay, Phys. Rev. Lett. **108**, 155501 (2012).

[250] H. Behera and G. Mukhopadhyay, AIP Conference Proceedings **1349**, 823 (2011).

[251] M. Houssa, E. Scalise, K. Sankaran, G. Pourtois, V. Afanasev, and A. Stesmans, Appl. Phys. Lett. **98**, 223107 (2011).

[252] Z. Ni, Q. Liu, K. Tang, J. Zheng, J. Zhou, R. Qin, Z. Gao, D. Yu, and J. Lu, Nano lett. **12**, 113 (2011).

[253] T. Otsuji, T. Watanabe, S. Boubanga Tombet, A. Satou, W. M. Knap, V. V. Popov, M. Ryzhii, and V. Ryzhii (2013).

[254] H. L. Zhuang, A. K. Singh, and R. G. Hennig, Phys. Rev. B **87**, 165415 (2013).